ABSTRACT

KARBALAEISADEGH, YASAMIN. Quantitative Ultrasound Tissue Characterization. (Under the direction of Dr. Marie Muller).

Ultrasound imaging is very challenging if not practically impossible in several biological tissues like bone and lung due to a phenomenon called multiple scattering. The heterogeneities, and significant acoustical impedance difference between the components of those media, are responsible for the deleterious effects of scattering. While multiply scattered signals complicate the conventional echolocation-based ultrasound imaging, they convey information with respect to the micro-structure of the medium. In the present study, we take advantage of multiple scattering of the ultrasound signals to characterize complex structures including cortical bone, lung and vessel phantoms by exploiting three different quantitative ultrasound (QUS) techniques.

We first give a brief introduction on radiative transfer theory and the diffusion of the wave in heterogeneous structures. The diffusion constant (D) is then measured for cortical bone samples with varying micro-structural parameters like pore diameter (Ct.Po.Dm.) and pore density (Ct.Po.Dn.) using finite-difference time-domain (FDTD) simulations. The increase in either Ct.Po.Dm. or Ct.Po.Dn. results in a decrease in D. This suggests that D can potentially be used to evaluate and monitor osteoporosis. In addition to assessment of cortical bone, we use the diffusion constant to evaluate chronic kidney disease in cats.

The other QUS parameters that we discuss in the thesis are the attenuation coefficient, and its constituents scattering coefficient and apparent absorption coefficient. We obtain these

parameters in porous structures mimicking cortical bone and evaluate them in different scattering regimes and with respect to micro-structural parameters (Ct.Po.Dm. and Ct.Po.Dn.). Based on our findings, increase in either pore size or density results in an increase in attenuation. In low/intermediate scattering regimes, this increase is a result of increase in scattering while in higher scattering regimes, this increase in attenuation is a result of increase in absorption suggesting that the wave has taken longer paths in the absorbing matrix (bone tissue) due to multiple scattering.

The third QUS technique that we use is based on backscatter statistics of the signals. We measure Shannon entropy which is a measure to quantify randomness in the multiply scattered signals. We use this parameter to evaluate cortical bone and lung mimicking phantoms. The simulations in bone indicate high correlations between entropy and micro-structural parameters. The study on porous phantoms mimicking lung demonstrates positive correlation between air volume fraction and entropy, suggesting the effectiveness of this method in assessment of diseases like pulmonary edema which is associated with increased levels of fluid in the lungs.

Quantitative Ultrasound Tissue Characterization

by
Yasamin Karbalaeisadegh

A dissertation submitted to the graduate faculty of
North Carolina State University
in partial fulfillment of the
requirements for the Degree of
Doctor of Philosophy

Mechanical Engineering

Raleigh, North Carolina
2020

APPROVED BY:

_____	_____
Dr. Marie Muller Committee Chair	Dr. David Lalush
_____	_____
Dr. Yun Jing	Dr. Fuh-Gwo Yuan

DEDICATION

To my family, the light of my life.

BIOGRAPHY

I was born on July 17, 1992, in Tehran, Iran. I received my B.Sc. in Mechanical Engineering from K.N. Toosi University of Technology in Tehran, Iran in 2014. I attended NC State University in 2016 to pursue my PhD where I discovered my passion for biomedical ultrasound and tissue characterization techniques. I hope that this dissertation would be my stepping stone toward future accomplishments.

ACKNOWLEDGMENTS

I would like to express my sincere gratitude to my adviser Dr. Marie Muller without whom none of this work could have been done. I have the utmost respect for her, not only as my adviser, but as an intelligent scholar and considerate and kind person. I would also like to thank my dear friend Omid Yousefian for his insightful collaboration, his wit and humour that made these past 5 years delightful. I would like to thank Kaustav Mohanty as he has taught me a lot and has always been a great help whenever I needed a second opinion on my work. I also wish to thank Dr. Kay Raum's group for their collaboration throughout these years. And at last, I would like to express my wholehearted gratitude to all my friends and family for their support.

TABLE OF CONTENTS

LIST OF TABLES

LIST OF FIGURES

Chapter 1: Introduction

1.1 Bone Biology

Bone is a dynamic organ that is developed through solidification of cartilage and connective tissue after birth. Its growth rate slows down with puberty such that 90% of adult bone is formed by the end of adolescence[1]. Bone modeling is an energetically costly physiological process that is responsible for growth of the skeleton during childhood and makes activities like walking and running possible. Malnutrition and limiting the source of energy halts the skeletal growth in children and decreases bone mass in adults[2]. Bone remodeling continuously takes place throughout adulthood with the aim of either adaptation to external circumstances causing bone damage, or simply to maintain the skeleton through the continuous process of renewing the adult skeleton every 10 years[1,3]. The most vital role of the bone in the body is providing it with substantial support. Bones have relatively high stiffness and strength resulting in great mechanical support for load-bearing purposes as well as protecting organs like lungs, heart, brain, etc, that are susceptible to fatal injuries. Organization of protective bone tissue for such organs is such that the maximum amount of energy is absorbed and minimum harm is caused. For instance, ribs are constructed with inherent curvature which provides significant protection and substantial impact energy absorption. Another major role of bones in the body is the production of red blood cells which takes place mostly in regions composed of spongy bone such as the iliac crest, vertebrae, and proximal femur[4]. Bone also is the site for mineral storage in the body: The skeleton stores 99% of calcium, 85% of phosphate and 50% of magnesium in the body[1]. Several factors, including aging can adversely influence bone functionality through hindering the bone turnover process.

1.2 Bone macrostructure

Cortical/compact and trabecular/cancellous bone are the two types of bone that are observed at macrostructural level. Cortical bone is very dense and surrounds the trabecular bone performing a protective function. It also comprises the main part of long bones (diaphyses). Trabecular bone has an interconnected structure of lamellae and is filled with marrow, providing structural support for the cortical shell while maintaining a relatively lower mass per unit volume. Structural differences in the arrangement of components are responsible for the differences in the mechanical properties of cortical and trabecular bones.

1.2.1 Cortical bone

Cortical bone forms about 80 percent of the skeleton [23] and surrounds the marrow and trabecular bone plates. It is the main component of long bone shafts (diaphyses) where there is only a little to no trabecular bone. The thick cortical wall in diaphysis, becomes thinner at the two ends of long bones (metaphyses). Short bones like tarsals and flat bones like skull have thinner cortices and more trabecular bone than diaphysis [21]. The majority of cortical bone is composed of osteons which have two types: primary and secondary. Primary osteons are formed through mineralization of cartilage in areas where bone is not present. They have relatively small vascular channels and do not contain as many lamellae as secondary osteons. The outer boundary of an osteon is called the cement line [5,6]. Secondary osteons are more complex, replace existing bone and are constantly formed through the remodeling process. These composite osteons are comprised of several intersected lamellae [7]. Osteons are usually oriented parallel to the diaphysis of long bones. A single osteon has a cylindrical shape and is composed of concentric lamellae which surround a central canal that is known as Haversian

canal and contains the blood supplies of the bone. While cortical bone is quite dense, the organization of different structures is such that blood supply would be accessible to all cells in a way that no cell lies more than 300 μm from a blood vessel [8,9].

The porosity of cortical bone generally ranges from 3 to 28 % [24], [25]. It is dense and provides maximum resistance to torsion and bending in long bones [21]. Due to its lower metabolic activity, its remodeling rate is much lower than trabecular bone [1]. This lower metabolic activity can specifically be observed in data from an immobilized limb where the increase in porosity in cortical bone occurs at a much lower rate than in trabecular bone [21].

1.2.2 Trabecular bone

Epiphyses and metaphyses of long bones as well as the vertebral bodies are comprised of trabecular bone which is a highly porous, heterogeneous and anisotropic tissue. Its honeycomb structure is comprised of numerous lamellar struts in a marrow matrix [10]. Parallel lamellae are bounded by cement lines to form single units of trabeculae. The lamellae consist of collagen fibrils and ellipsoidal lacunae. The higher stress concentration at the longitudinal direction of lacunae makes trabecular bone packet more susceptible to micro-damage [11]. While in the vertebral bodies, trabecular bone performs the main load-bearing role, in the appendicular skeleton, it transfers the loads from the joint surface to cortical bone [12]. The mechanical properties of trabecular bone depends not only on the bone tissue composition, but also on the orientation and structural position of the struts and collagen fibers within the marrow filling [13]. The more closely the trabecular nodes and plate-trabeculae are located, the higher the overall stability and strength of the bone would be [14].

1.3 Osteoporosis

Bone is a dynamic connective tissue that is constantly changing throughout one's life. There are different types of cells in bone, each responsible for a certain task. Osteoblasts function as bone forming cells to synthesize bone matrix while osteoclasts resorb bone (and cartilage) during both skeletal modeling and remodeling processes. Their activity has a deep impact on skeletal vitality. Accordingly, any malfunction in the process of bone formation and resorption can cause unbalanced bone turnover and lead to osteoporosis [15]. Osteoporosis which literally means "porous bones" is a very common bone disease which is characterized by loss in bone mass that leads to structural deterioration of the skeleton, reduced bone strength and elevated risk of bone fracture. Osteopenia is the initial stage of bone loss and the precursor to osteoporosis[16]. It is estimated that the number of people with osteopenia/osteoporosis in the US will increase to 61 million by the year 2020 [17]. According to the national osteoporosis foundation reports, the number of people in the US with low bone density is estimated to be 44 million as of the year 2017. Despite the high prevalence of this disease, a lot of the cases are undiagnosed since the patients are usually unaware of the disease until the occurrence of fractures. This is why osteoporosis is known as the "silent disease".

There are different hormonal, environmental, genetic, biomechanical and nutritional factors that influence bone turnover. For instance low levels of calcium and vitamin D, estrogen deficiency and exogenous glucocorticoids can affect the bone mass adversely [18]. It is shown that in postmenopausal women the decrease in oestrogen levels is associated with the loss of bone of up to 4% annually implying that women may lose 40% of their total bone mass from 40 to 70 years. The approximate bone loss for men for the same period is 12% [15]. Another

study on Canadian population indicates that 46% of posmenopausal women and 40% of men over 50 are estimated to have osteopenia presenting low levels of bone density [19].

Age-related fractures are the most common manifestations of osteoporosis and are associated with the largest proportion of mortality from osteoporosis [20]. Approximately 75% of all osteoporotic fractures occur in individuals older than 65 years old [21]. Osteoporotic fractures may occur not only from a fall but from simple routine activities such as bending or lifting objects. Approximately one in three women and one in five men experience an osteoporotic fracture in their lifetime [22]. It is estimated that only 44% of the people with hip fracture return home after being dismissed from hospital while 10% go to another hospital, 17% go to long-term care facilities and 27% go to rehabilitation centers. Less than half of them return to pre-fracture conditions and recover to resume daily activities [23]. After the age 75, hip fractures become the most common fractures and up to half of the old individuals with hip fracture will face permanent disabilities [24]. While men are less prone to osteoporosis, it is estimated that one third of all hip fractures occur in men. The percentages of men and women over 50 that are affected by vertebral deformities which represent vertebral fractures are 21.5% and 23.5% respectively [25]. These vertebral fractures usually remain undiagnosed (70% of the cases), since individuals do not seek medical attention with regard to back pain, or physicians do not suspect a fracture to order radiographs for better clarification [26]. Aside from hip fractures, the most common sites of non-vertebral fractures are distal forearm and proximal humerus [27]. Unlike hip fractures which usually happen due to falling indoors, fractures in forearm and humerus occur among more active seniors who spend more time outdoors [28].

1.4 Imaging methods to evaluate bone quality

To evaluate bone quality, several methods such as radiography, absorptiometry, magnetic resonance imaging (MRI), computed tomography (CT) and quantitative ultrasound (QUS) can be used. Currently, the most commonly used technique to diagnose osteoporosis is based on bone mineral density (BMD) measured by dual energy X-ray absorptiometry (DXA). DXA functions through alteration of 2 different energies. As the X-ray emitted beam travels in the body, the interaction with chemical compounds within the body differentially attenuates the 2 energies. Differential attenuation allows for discrimination between bone and soft tissue since attenuation is much higher in bone. The attenuation values are then converted to areal BMD obtained from a reference standard. The common regions for bone mass assessment using DXA are the whole body, lumbar spine, proximal femur, forearm, or hand [29]. The fact that DXA is associated with ionizing radiation makes it difficult to use this technique for regular monitoring of osteoporosis. Computed tomography (CT) is another modality which like DXA uses radiation to obtain images of bone. The advantage of CT over DXA is improved resolution and volumetric information which provides details on the bone geometry, cortical bone density, trabecular bone density and bone volume [30]. Like DXA, exposure to ionizing radiation is a huge disadvantage of CT imaging. The radiation exposure increases with increase in resolution and number of slices [31]. Magnetic resonance imaging is a method based on resonance and relaxation of protons which generates signals from lipids and water in the body. The scanned slices are used to construct a 3D volume. Unlike CT, MRI does not cause ionizing radiation and is relatively safe. MRI can differentiate between trabecular and cortical bone but the clinical scanners do not have high resolution and micro-architectural details are

inaccessible. Aside from the costs, the major drawbacks to MRI are long scanning time (20-30 minutes), low resolution, high cost and loud noise.

1.5 Importance of quantitative ultrasound (QUS) for bone assessment

DXA is the gold standard for bone assessment, however, this method merely focuses on bone mass and does not provide information on micro-structure of the bone while according to National Institute of Health (NIH) bone quality refers to mineralization, turnover, architecture and damage accumulation. This calls for developing alternative techniques to evaluate bone. Compared to other imaging techniques, ultrasound is radiation-free, inexpensive and easy to operate. While ultrasound imaging is highly effective in media where scattering is not dominant and simple scattering approximation is valid, in heterogeneous cases with strong scatterers _ such as pores in cortical bone and struts in trabecular bone _, an ultrasonic image may not be a desirable representation of the medium, since the received signals are the result of multiple and complex interactions with the medium. The energy of the coherent part of the wave diminishes as it propagates in a multiple scattering medium, complicates the Green's function and makes ultrasound imaging difficult [32]. Alternatively, quantitative ultrasound techniques are widely researched to access the micro-architectural properties of scattering structures and characterize them. Ultrasound waves are attenuated, refracted and scattered at tissue interfaces and heterogeneities as well as changes in the heterogeneities are expected to affect the propagation of the ultrasound waves in the medium, resulting in changes in ultrasonic parameters. Several quantitative ultrasound studies have exploited ultrasonic parameters like speed of sound (SOS), broad-band ultrasound attenuation (BUA), and backscatter coefficient to characterize different structures like biological tissues [33–38], concrete [39,40], or oil-water/gelatin mixtures [41,42].

While hip and spine are more susceptible to fracture risks, it can be assumed that osteoporosis is a systemic disease reflected in peripheral sites as well. QUS evaluation of trabecular bone at accessible sites such as calcaneus was first implemented by Langton in 1984 through measurements of frequency-dependent ultrasound attenuation for 60 female volunteers, finding age and fracture related changes in frequency dependence of attenuation [37]. Several other studies have implemented a similar approach to investigate the changes in trabecular bone [33,34,43] and cortical bone [44,45]. Strong relationship between SOS in tibia bone, elastic modulus and BMD have been reported [46–48]. Structural properties of bone such as cortical thickness, anisotropy and porosity also influence SOS [29,49,50]. Bone strength can also be assessed by QUS techniques [51–53]. In a study by Lee et al. strong correlations between ultimate and yield strength of cortical specimens and tibial SOS are reported [54]. While the calcaneus has been prevalently used for QUS measurements, other sites such as radius are also proven to be useful in investigating the age-related changes in bone [55]. The fact that ultrasonic parameters such as SOS are influenced by both bone mass and structure, makes them better determinants of osteoporosis compared to BMD measured by DXA[56]. In a study by Pande et al. SOS is reported to effectively differentiate between normal and pagetic bone with structural abnormalities[57] while BMD is not affected [58]. This indicates that QUS provides complementary information on bone micro-structure which is not captured by BMD.

1.6 Outline of the dissertation

The objective of the present study is to introduce three different quantitative ultrasound approaches to characterize heterogeneous biological tissues. While different tissues such as kidney are evaluated, the main focus of the present work is on characterization of cortical bone. The density and size of the pores, affect the wave propagation in the bone structure. The pores

act as scatterers and it is expected that the changes in the micro-structure will be reflected in the multiply scattered signals. The diffusion constant, attenuation and backscatter statistics are related to multiple scattering and are subsequently exploited in the present study to characterize cortical bone as well as other heterogeneous structures.

In chapter 2, we introduce the radiative transfer theory and mathematical derivation of the diffusion constant. The diffusion constant is then used as a quantitative parameter to evaluate cortical bone structures in a simulation study and in-vivo experiments on distal tibia of 49 patients.

In addition, backscattered signals from contrast enhanced cat kidneys are used to measure the diffusion constant in kidney and characterize different stages of the chronic kidney disease.

In chapter 3, apparent absorption coefficient is introduced which represents the difference between the total attenuation and attenuation exclusively due to scattering. We investigate the micro-structural changes in cortical bone samples using finite-different time-domain (FDTD) simulations and assess their effect on attenuation, scattering coefficient and apparent absorption coefficient. In addition, we evaluate porous scattering media at different scattering regimes through a spectroscopy study to investigate the frequency-dependence of those parameters.

Chapter 4 focuses on backscatter statistics of the signals and exploits Shannon entropy to characterize cortical bone and lung-mimicking phantoms. We use FDTD simulations to model ultrasound scattering in cortical bone samples. The entropy maps are then evaluated as a function of structural parameters like pore diameter, pore density and porosity. In addition,

the in-vivo data from cortical bone obtained from the tibiae of several patients is used for entropy assessment. The results are compared with structural parameters obtained from high-resolution peripheral quantitative computed tomography (HRpQCT) imaging.

In addition, lung mimicking phantoms with different air volume fractions are evaluated to investigate the effectiveness of entropy as a measure to diagnose and monitor pulmonary edema.

In chapter 5 we introduce a novel technique to use the diffusion constant in phantoms mimicking the vasculature. These hollow tubes are filled with contrast agents and a dual frequency transducer is used to excite the micro-bubbles at their resonance frequency. The goal is to acquire the backscattered signals at higher harmonics to suppress the response from the tissue and get the information merely from the vascular network. The diffusion constant is then calculated and exploited to evaluate the structural changes in the vasculature.

Chapter 2: Characterization of biological tissues using the diffusion constant

A brief background on single and multiple scattering of ultrasound is provided here before elaborating the mathematical representation of the diffusion constant (D). Effects of change in the cortical bone structure on D are reported subsequently.

2.1 Single scattering regime

When the wavelength is considerably larger than the size of heterogeneities, the interaction of the wave with the heterogeneities is weak. These conditions are known as Born approximation or single scattering approximation [59]. In this case, the scattered wave is assumed to result from single scattering of the wave by heterogeneities, and multiple scattering encounters are ignored. The Born approximation is widely used in weakly scattering problems in different fields including seismology [60,61], biomedical ultrasound [62] and NDE [63]. When dealing with weakly scattering media, the Born Iterative (BI) method and the Distorted Born Iterative (DBI) methods can be implemented to solve forward and inverse problems to characterize scattering structures through iterative updating of the Green's function [64].

2.2 Multiple scattering regime

When the size of the particles is the same order or larger than the wavelength, ultrasound waves lose some energy as a result of multiple scattering and get diffused through random trajectories as they interact with heterogeneities. The traditional ultrasound techniques which emphasize on coherent pulse-echo reflections and deal with weakly scattering media, would fail in structures with strongly scattering features in which wave trajectories

demonstrate random characteristics. However, these coda waves that reflect multiple scattering in the medium, are deterministic and can convey structural information from the random-like waveforms [59]. The term "coda" was initially adopted in geophysics and was used to describe the lasting wave trains after seismic waves [65]. The coda waves have been studied in different fields (optics, acoustics, geophysics) and have indicated a temporal relevance to perturbations in the medium [66–68]. Diffuse wave spectroscopy in optics [67] and coda wave interferometry to study volcanos [69,70] and Earth's crust [71] are among the notorious applications of multiple scattering. Ultrasound has been exploited in non-destructive testing and evaluation (NDT&E) techniques as a tool to detect cracks which are induced as a result of stress overload, temperature and pressure changes, etc. Combination of enforcing steel bars, grains of sand, porosities, etc., results in heterogeneities which have a wide size range leading to multiple scattering of ultrasonic waves [72–74]. Ultrasound waves can be used to characterize mechanical properties of materials and detect early signs of damage through regular monitoring procedures. Ultrasound NDE techniques are specifically helpful for crack detection in concrete which is very brittle and susceptible to structural failure initiated by micro-cracks. Several studies have applied quantitative techniques to exploit coda waves and evaluate damage in concrete structures [59,75–78].

Historically, there have been two distinct approaches towards complexities of wave propagation in scattering media. One is "radiative transfer theory" or "transport theory" and the other is "multiple scattering theory". The multiple scattering theory obtains solutions to wave equation for a single particle, discusses the interaction between the particles and implements statistical averaging [79]. The light scattering in the presence of powders, pigments, polymers, hydro- and aerosols, emulsions etc., scattering of electrons in crystal structures,

neutron transport in objects with various shapes, are all examples of the multiple scattering phenomenon [80–83].

The radiative transfer theory which was initially proposed by Schuster in 1905 is based on phenomenological observations of the transport characteristics of intensities. For dense distributions of scatterers, the diffusion approximation can be applied [79]. However, the discovery of weak localization as a manifestation of new features in electronic magnetoresistance of metals at low temperatures [84,85], challenged the radiative transfer theory where multiple scattering of waves would destroy the wave phenomenon and they could be simplistically considered as hard spheres colliding with the heterogeneities. In fact, weak localization which originates from constructive interference between reciprocal paths during the wave scattering process, increases the probability for the wave to return to the source by a factor of 2 [32]. In optics, this effect was first observed in light scattering in 1985 and is known as "coherent backscattering effect" (CBE) [86]. It suggests that even in highly scattering media, coherent interferences can survive, the energy of the wave would not completely be diffused, and enhancement in the energy would be observed at exact backscattering direction. In optics [86,87] and acoustics [88,89] CBE has been exploited to extract information from the scattering media and it has accurately predicted parameters like transport mean-free path l^* and diffusion constant (D). In a study on glass beads in water, J. H. Page et al. investigated the frequency dependence of the diffusion constant. They demonstrated that D vary strongly with frequency when size of the beads is comparable to the wavelength [90]. Aubry and Derode measured the diffusion constant from the growth of the incoherent intensity for a structure with metal parallel rods (acting as scatterers) immersed in water. They were able to extract a 1D map of the structure through local measurements of D which depicted the change in the concentration of

the rods [91]. Diffusion constant has also proven to be sensitive to micro-structural changes in trabecular bone. In a study by Aubry et al. D was locally measured for a sample of human trabecular bone where improved contrast compared to densitometry image was obtained indicating the potentials of QUS techniques compared to conventional X-ray [92].

2.3 Mathematical derivation of the diffusion constant in a multiple scattering medium

2.3.1 The radiative transfer equation (RTE)

The empirical derivation of RTE was first done by Chandrasekhar [93]. Considering that x is the location of a particle and k the direction of propagation, it is possible that the particle is scattered in the direction k'. The mean specific intensity after ensemble averaging is described by RTE as follows:

$$k.\nabla \mathrm{I}(\mathrm{x},\mathrm{k}) = -\frac{I(x,k)}{l} + \frac{1}{4\pi l}\int_{4\pi} I(x,k')p(k',k)dk' + e(x,k) \qquad \text{Equation 2-1}$$

where k is a unit vector and $I(x,k)$ is the specific intensity of the wave at position x (propagating in direction k). Equation 2-1 historically was derived empirically from the conservation of energy:

- The left hand side represents the particle advection;

- $I(x,k)/l$ shows the loss as a result of scattering in another direction where l is the elastic mean free path. It is linked to the probability of being scattered to direction k' while traveling in direction k.
- $\frac{1}{4\pi l}\int_{4\pi} I(x,k')p(k',k)dk'$ stands for gain and $p(k',k)$ is the density of probability of getting scattered in direction k' while initially travelling in direction k.
- $e(x,k)$ is the source term showing the probability to create a particle at position x which propagates in direction k.

The relation between the specific intensity and the stationary wave equation has been studied in[94], but the derivation is challenging and tedious. In the RTE approach, the wave packets travel as energy quanta with a velocity. There is no information on the phase of the wave but the memory of the trajectory of the packets is retained[32].

2.3.2 Diffusion equation and calculation of the diffusion constant

Diffusion equation derives from the RTE but instead of dealing with intensity in a certain direction it deals with the energy density ρ:

$$\rho(x,t) = \frac{1}{c}\int_{4\pi} I(x,k,t)dk \qquad \text{Equation 2-2}$$

$$\xRightarrow{RTE\ and\ \text{Equation 2-2}} \partial_t\rho - D\nabla^2\rho = \delta(x)\delta(t) \qquad \text{Equation 2-3}$$

where t is the lapse time and D is the diffusion constant. In other words, in this approach the intensity diffuses isotropically as a Brownian motion. The reason is that since multiple scattering events result in a more uniform distribution of energy over a large angle of propagation, the Green function of the radiative transfer equation P, can be estimated by the solution of the diffusion equation for relatively large time lengths[32,95]. P is the probability density for the wave to get from the first scattering event R_1 to scattering event R_n after time T and can be written as follows[96]:

$$P(R_1, R_n, T) = \frac{\exp\left[-\frac{(x_1 - x_n)^2}{4DT}\right]}{\sqrt{4\pi DT}} \times \sum_{m=1}^{\infty} \sin\left(\frac{m\pi\left(z_1 + \frac{z_r}{2} + z_0\right)}{B}\right) \times \sin\left(\frac{m\pi\left(z_n + \frac{z_r}{2} + z_0\right)}{B}\right) \exp\left(-\frac{m\pi^2 DT}{B}\right), \quad \text{Equation 2-4}$$

x and z indicate the transverse and axial (the direction of wave propagation) coordinates respectively. z_r is the longitudinal dimension of the focus of the beam. z_0 is derived from the exact solution of the Milne problem which indicates that P is zero on the plane $z = -\frac{z_r}{2} - z_0$ where $z_0 = \frac{\pi l^*}{4}$ (l^*: transport mean free path). $B = L + 2z_0$ is the effective thickness of the scattering medium.

Incoherent and coherent contributions of the intensity I_{inc} and I_{coh} can be written respectively as follows[91]:

$$I_{inc}(0, X, T) \simeq \iint d^2R_1 d^2R_n |\psi_{in}(0, R_1)|^2 P(R_1, R_n, T) \times |\psi_{out}(R_n, X)|^2 \quad \text{Equation 2-5}$$

$$I_{coh}(0,X,T) \simeq \iint d^2R_1 d^2R_n \psi_{in}(0,R_1)\psi_{in}^*(0,R_n) \times P(R_1,R_n,T)\psi_{out}(R_1,X)\psi_{out}^*(R_1,X) \quad \text{Equation 2-6}$$

where ψ_{in} and ψ_{out} are emitted and backscattered beams respectively. X is the distance between the emitter and receiver. Equation 2-5 results in[91]:

$$I_{inc}(0,X,T) \simeq (4\pi DT)^{-\frac{1}{2}} \exp\left(-\frac{X^2}{4DT}\right) I_z(T) \quad \text{Equation 2-7}$$

$I_z(T)$ is derived as follows:

$$I_z(T) = \sum_{m=1}^{\infty} \exp\left(-\frac{m\pi^2 DT}{B}\right)\left\{\left[\frac{1}{l_e^2} + \left(\frac{m\pi}{B}\right)^2\right]^{-1} \times \left[\frac{m\pi}{B}\cos\left(\frac{m\pi z_0}{B}\right) + \frac{1}{l_e}\sin\left(\frac{m\pi z_0}{B}\right)\right]\right\}^2, \quad \text{Equation 2-8}$$

where l_e is the elastic mean free path. Equation 2-7 illustrates that the growth of the diffusive halo is a result of the term $\exp\left(-\frac{X^2}{4DT}\right)$. This indicates that by obtaining the incoherent contribution of the intensity and using this estimation, the diffusion constant can be obtained[91]. The procedure of calculating D for cortical bone samples is summarized in section 2.4.2.3.

2.4 Diffusion constant measurement in cortical bone

While osteoporosis assessment has long focused on the characterization of trabecular bone, the cortical bone micro-structure also provides relevant information on bone strength. This numerical study takes advantage of ultrasound multiple scattering in cortical bone to investigate the effect of pore size and pore density on the acoustic diffusion constant. Finite-difference time-domain simulations were conducted in cortical microstructures that were derived from acoustic microscopy images of human proximal femur cross sections and modified by controlling the density (Ct.Po.Dn) $\in [5-25]\frac{pore}{mm^2}$ and size (Ct.Po.Dm) $\in [30-100]\mu m$ of the pores. Gaussian pulses were transmitted through the medium and the backscattered signals were recorded to obtain the backscattered intensity. The incoherent contribution of the backscattered intensity was extracted to give access to the diffusion constant D. At 8 MHz, significant differences in the diffusion constant were observed in media with different porous micro-architectures. The diffusion constant was monotonously influenced by either pore diameter or pore density. An increase in pore size and pore density resulted in a decrease in the diffusion constant (D= $285.9Ct.Po.Dm^{-1.49}, R^2 = 0.989, p = 4.96 \times 10^{-5}, RMSE = 0.06$; $D = 6.91Ct.Po.Dn^{-1.01}, R^2 = 0.94, p = 2.8 \times 10^{-3}, RMSE = 0.09$), suggesting the potential of the proposed technique for the characterization of the cortical microarchitecture. In addition to the numerical study, an experimental study on 49 patients is done. The data from tibia bone is obtained and processed for D. While this clinical study has not led to a robust validation of the simulation results, it is a vital first step towards quantitative assessment of cortical bone using ultrasound as a safe, portable and relatively inexpensive modality.

2.4.1 Introduction

Long bones consist of a trabecular core and an outer compact cortical bone shell. The latter is highly dense, but is pervaded by elongated pores, which results in a porosity (Ct.Po) ranging between 3% and 28% [97,98]. For decades, studies of bone pathologies have focused on the characterization and evaluation of trabecular bone, as it is viewed as metabolically more active and is a common fracture site [99]. However, the assessment of cortical bone is also of high interest since it bears considerable loads and is closely linked to bone strength [99–104]. The load-carrying capacity of cortical bone is considerable at relevant sites such as vertebrae and femoral neck[99,105–109]. It has been shown that bone elastic modulus, toughness and impact energy absorption capacity decrease as cortical porosity increases [106].

Bone mineral density (BMD) is extensively used to diagnose and monitor osteoporosis as it is inversely related to fracture risk [110,111]. The most common technique to measure BMD is dual energy x-ray absorptiometry (DXA). Due to its limited resolution and use of ionizing radiation, it is important to find reliable alternatives to DXA. Quantitative ultrasound (QUS) is a potential alternative, as it permits measurements of fracture-associated bone properties at relevant anatomical regions (e.g., the distal radius and the proximal femur).

Despite significant improvements in ultrasound imaging techniques for soft tissues, ultrasound still presents limitations for imaging solid and porous media such as bone, in which the difference in acoustic impedance between bone tissue and marrow-filled pores is large, leading to large amounts of scattering and attenuation. The potential of multiple scattering to reflect microstructural features of heterogeneous media has been applied in fields such as geophysics, optics, and acoustics [87,91,92,112–116]. Aubry et al. have observed the signature of

multiple scattering in trabecular bone[117]. Tourin et al. took advantage of constructive interferences of backscattered signals in multiple scattering media to extract parameters such as the diffusion constant (D) and transport mean free path [113]. Aubry and Derode have exploited the same principles to measure the diffusion constant in phantoms of steel rods submerged in water[91] and concluded that the diffusion constant could discriminate samples with different scatterer densities. We hypothesize that a similar approach can be applied to bone, in which the typical pore size and the impedance difference between pores and bone tissue is appropriate to lead to multiple scattering and give rise to a diffusive regime of ultrasound waves.

In the present numerical study, we calculate the diffusion constant D for bone geometries with artificially modified porosities when cortical pore density (Ct.Po.Dn) and pore diameter (Ct.Po.Dm) are varied independently. The aim is to determine the dependence of D to structural features such as pore size and pore density. Compared with experimental data acquisition, the numerical approach proposed here allows the necessary, full control over Ct.Po.Dm and Ct.Po.Dn. In addition, data from the tibia bone of 49 patients is acquired. The experimental data is processed to obtain D. The diffusion constant values are evaluated as a function of micro-structural parameters obtained from high-resolution peripheral quantitative computed tomography (HR-pQCT).

2.4.2 Methodology

2.4.2.1 Generation of bone geometries

To study the effect of Ct.Po.Dn and Ct.Po.Dm on wave propagation in bone, these two parameters needed to be accurately controlled in the simulated cortical bone geometries. First, a 2D image of a human femoral shaft cross-section was obtained by Scanning Acoustic

Microscopy (SAM) through the following processes: The left femur was obtained from a 71-year old male donor in accordance with the German Law "Gesetz über das Leichen-, Bestattungs- und Friedhofswesen des Landes Schleswig-Holstein - Abschnitt II, §9 (Leichenöffnung, anatomisch)" from 04.02.2005. A 21-mm thick cross section was extracted from the proximal femur shaft and prepared for SAM as described elsewhere [118]. Briefly, after removal of soft tissues and washing in Phosphate buffered saline (PBS), one surface of the sample was polished on a planar grinder (Phoenix 4000, Buehler Ltd. Illinois). After the polishing, samples were washed again and degassed while submerged in 1 % buffer solution. The SAM measurement was performed using a custom built quantitative scanning acoustic microscope [119] and a 100-MHz spherically focused transducer (KSI 100/60°, KSI, Herborn, Germany), providing a beam diameter of 19.8 μm at a focal depth of 139 μm [120]. Device and scanning procedure have been described in detail elsewhere [121]. The image was acquired with a pixel size of 12 μm in the x-y-plane. Recorded signals were then bandpass-filtered (Chebyshev filter) and the reflected amplitude determined as the maximum of the (Hilbert-transformed) envelope signal. Established procedures were applied for defocus correction, calculation of acoustic impedance (Z) values [30] [31] and thresholding of the bone tissue [121]. The obtained image was then resampled to reach the desired pixel size of 10 μm for simulations. To resample the image, bicubic interpolation method was used such that the output pixel value would be the weighted average of pixels in the nearest 4 by 4 neighborhood.

To measure the average pore diameter and pore density, every single closed surface within the segmented bone cross-section was labelled. The number of labels indicated the total number of pores, while the ratio between pore number and the entire bone area provided the pore density Ct.Po.Dn, in number of pores / mm^2. To estimate the mean pore diameter, pores were

assumed to have circular shape. By measuring the surface area of each pore and averaging the calculated diameters, the mean pore diameter Ct.Po.Dm was obtained.

The reference image was modified to obtain structures with desired Ct.Po.Dn and Ct.Po.Dm. The modification of Ct.Po.Dm, was performed such that the average pore size would decrease radially from the endosteal towards the periosteal surface. The reason for this is that trabecularization of cortical bone commonly starts from the endosteal surface [99] and larger pores are usually observed close to the endosteum [124].

To obtain bone images with average pore size varying radially, the total number of pores and subsequently Ct.Po.Dn were kept constant at $10\frac{pore}{mm^2}$, according to results of a previous work by Bousson et al [125]. To obtain the exact Ct.Po.Dn of $10\frac{pore}{mm^2}$, some pores were randomly removed from the reference SAM image. The cortical bone in the resulting image was then divided into four concentric curved bands with approximate width of $750\mu m$ (Figure 2-1.a).

By morphologically dilating or eroding pixels from the pores falling within each band and averaging Ct.Po.Dm over the whole image we created 8 bone structures with varying average Ct.Po.Dm ranging from 30 μm to 100 μm. Figure 2-1.b and Figure 2-1.c show examples of two bone slices with the same Ct.Po.Dn and different average Ct.Po.Dm.

A similar workflow was followed to generate bone images with varying Ct.Po.Dn. A reference image with average Ct.Po.Dm of 60 μm was modified by randomly adding/removing pores, all the while maintaining a higher Ct.Po.Dn in the endosteal region and a lower Ct.Po.Dn near the periosteal surface. This provided 8 different structures with average Ct.Po.Dm of 60 μm and Ct.Po.Dn ranging from $5\frac{pore}{mm^2}$ to $25\frac{pore}{mm^2}$.

For each combination of Ct.Po.Dn and Ct.Po.Dm, three structures were created with different random pore distributions resulting in a total of 45 structures. The ranges for Ct.Po.Dn and Ct.Po.Dm were chosen in agreement with those reported in previous works [104,126–128].

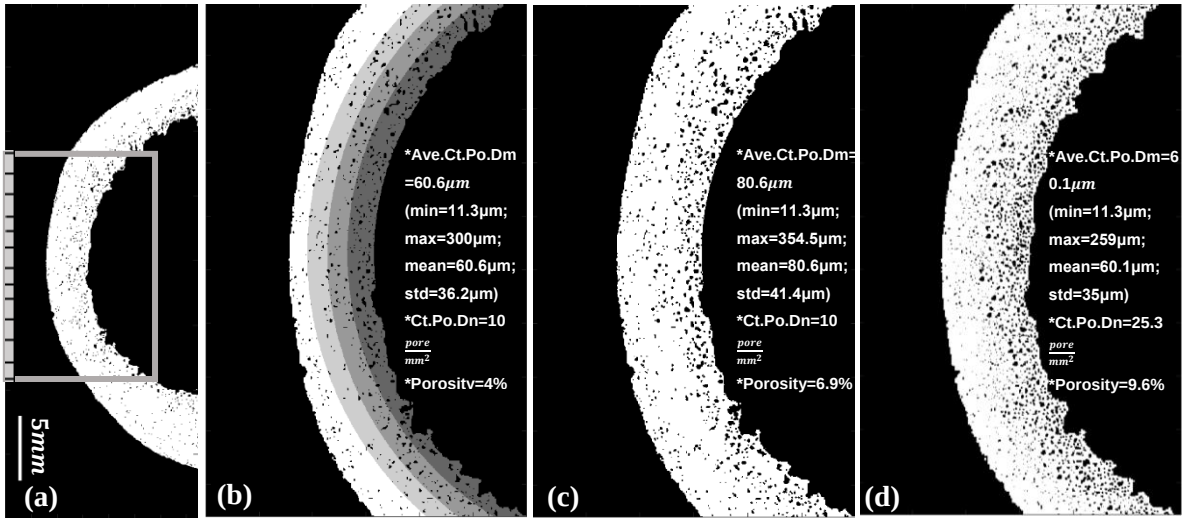

Figure 2-1 a: Binarized SAM image of a human femur shaft cross-section with Ct.Po.Dn of 10 pore/(mm^2) , average Ct.Po.Dm of 60.6 µm (min=11.3µm; max=300µm; mean=60.6µm; std=36.2µm) and porosity of 4%. The left edge of the frame indicates the position and length of the 64-element array transducer with respect to the bone image; b: Detail of the region in the frame in figure 1-a. To manipulate the Ct.Po.Dm the cortical bone is divided in 4 regions based on the distance to the endosteum: the increase in pore size is smaller for the outer bands since trabecularization of the bone starts from the endosteal region; c: The average Ct.Po.Dm is artificially increased while keeping the Ct.Po.Dn constant. Ct.Po.Dn=10pore/(mm^2); Average Ct.Po.Dm=80.6µm (min=11.3µm; max=354.5µm; mean=80.6µm; std=41.4µm); Porosity=6.9%; d: Ct.Po.Dn is artificially increased while keeping the average Ct.Po.Dm constant; Ct.Po.Dn = 25.3pore/(mm^2); average Ct.Po.Dm = 60.1µm (min=11.3µm; max=259µm; mean=60.1µm; std=35µm); Porosity = 9.6%. Both an increase of Ct.Po.Dm and of Ct.Po.Dn lead to an increase of the sample Ct.Po.

2.4.2.2 In-vivo measurement of micro-structural parameters at the distal third of the tibia

49 female patients aging from 56 to 86 (mean age: 69 ± 7 y) took part in the present study which was approved by the German Radiation Protection Ordinance (z5-22464/2019-090-G). Starting at approximately 20 mm from the tibial endplate (ultradistal tibia), high-resolution peripheral quantitative computed tomography scans with a nominal isotropic resolution of $60\mu m$ were performed using a clinical HR-pQCT scanner (XtremeCT II, Scanco Medical AG, Brüttisellen, Switzerland). The volumetric bone mineral density (vBMD) was

obtained as described in [129]. The cortical bone was segmented following a procedure detailed by Burghardt et al [130]. Using the manufacturer's scripts, cortical porosity, pore diameter and pore density were obtained.

2.4.2.3 Data acquisition and calculation of the diffusion constant (numerical simulation study)

The SimSonic open-source software (www.simsonic.fr) [131] was used to compute a numerical solution to the elastic wave propagation in the 2D cortical bone structures described above. The approach was based on a Finite-Difference Time-Domain algorithm and could model the wave propagation in heterogeneous media with a combination of solid and fluid materials. A 64-element linear array transducer with central frequency of 8 MHz and element width of 0.3 mm was simulated. Simulations were carried out in the near field, resembling potential future *in-vivo* applications of ultrasound, where cortical bone is accessible; e.g., at the tibia shaft. Despite being derived from a femoral bone image, the present simulations remain informative considering the structural and acoustical similarities between the cortical bone of the tibia and femur [132,133]. The linear array transducer was placed at a distance of 3 mm from the periosteal surface. Homogeneous material properties (

Table 2-1) for bone and water were assigned to each pixel (bone tissue and pores, respectively) of the binary SAM image.

Table 2-1 Values of stiffness constants for isotropic cortical bone(Bossy et al., 2004) and water used in the simulations.

	Bone	Water
Density	1.85 ($\frac{g}{cm^3}$)	1 ($\frac{g}{cm^3}$)
$C_{11} = C_{22} = C_{33}$	29.6 (GPa)	2.37 (GPa)
$C_{12} = C_{23} = C_{31}$	17.6 (GPa)	2.37 (GPa)
$C_{44} = C_{55} = C_{66}$	6.0 (GPa)	0 (GPa)

In addition to the structures modified from one reference SAM image (45 structures), simulations were run for four other femur images obtained by scanning acoustic microscopy from different donors to account for the effect of individual differences. To have a wider range of average pore diameter (Ct.Po.Dm∈[55.34-71.42μm]) and pore density (Ct.Po.Dn∈[10-21 $\frac{pore}{mm^2}$]), simulations were also run on modified versions of these images where either average Ct.Po.Dm or Ct.Po.Dn were reduced to 60μm and 10$\frac{pore}{mm^2}$ respectively.

Perfectly matched layers with a thickness of 7.5 mm were added at the four boundaries of the simulation map, to ensure minimal reflections while not increasing the simulation time drastically. A grid step of 10μm was chosen for the simulations to meet 20 points per wavelength [134].

Each element of the array was excited with a Gaussian pulse with a central frequency of 8 MHz (3dB bandwidth = 3.33MHz). For each single-element transmit, the reflected signals

were recorded by all 64 elements. Figure 2-2 illustrates the data acquisition process for one transmit. The process was repeated for all 64 transducer elements providing an inter-element response matrix H, containing 64×64 time traces. Due to reciprocity, the inter-element response matrix H is symmetric such that $h_{ij} = h_{ji}$ where h is the backscattered signal in the time domain, and the indices i and j indicate the number of emitter and receiver elements, respectively.

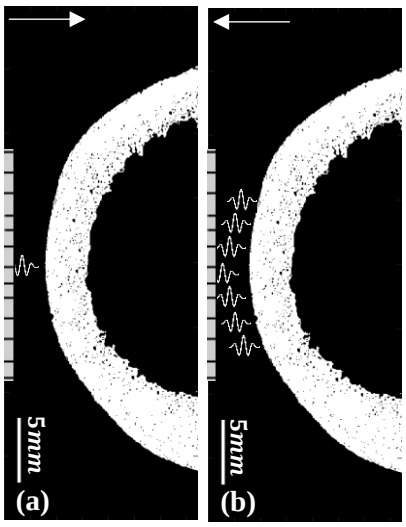

Figure 2-2 Schematic representation of data acquisition. a: An 8 MHz Gaussian pulse is transmitted from one transducer element to the multiple scattering medium; b: The response is recorded on all the elements of the array transducer. Repeating the process for all the elements results in an inter-element response matrix.

For all geometries, the diffusion constant D was determined according to a method proposed by Aubry and Derode [91]. The first step was to time-shift the h_{ij} signals such that all the response signals started at the same time. This time-shifting step was necessary to compensate for differences in arrival times due to differences in transmitter-receiver distances and to the curvature of the bone surface. The received signals have two main components: 1) the signal that initially has been transmitted and has travelled the exact distance between the

emitter and receiver, 2) the signal that has been reflected by the medium. Figure 2-3.a shows the signal emitted by element 1 and received by element 10 and Figure 2-3.b shows all the 64 received signals for the first emission. By setting a threshold of 0.02 times the maximum of the signal amplitude, the start of each signal was detected and shifted to time T = 0μs (Figure 2-3.c). Then the initial part of the signal (that has just traveled the emitter-receiver distance and was shifted to time T=0μs) was cut out and the shifting process with the same threshold is repeated for the backscattered signals from bone (Figure 2-3.d).

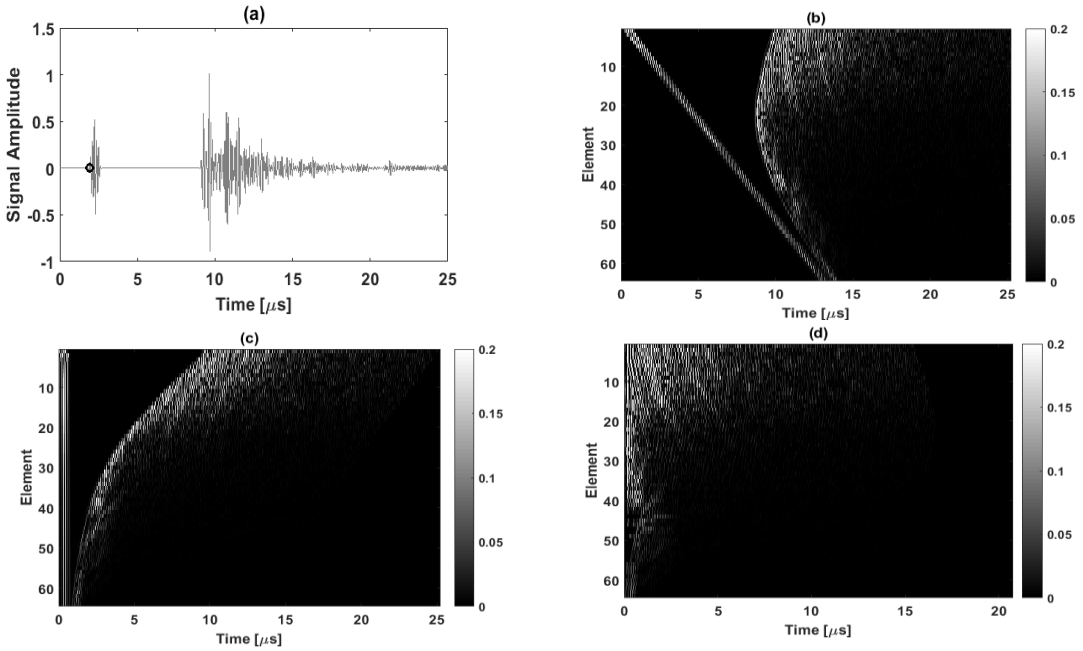

Figure 2-3 a) Signal emitted by element 1 and received by element 10 for one of the bone structures. The start of the signal is detected using a threshold equal 0.02 times the maximum of the signal (black circle) b) All 64 received signals for the first emission. c) The starts of the signals are detected and shifted to time T=0μs. d) The initial part of the signal (that has just traveled the emitter-receiver distance), is cut out and the backscattered signals from bone are time-shifted with the threshold equal 0.02 times the maximum of the signals.

After the time-shifting process, each signal was truncated into 0.5 μs half-overlapping time-windows (Figure 2-4).

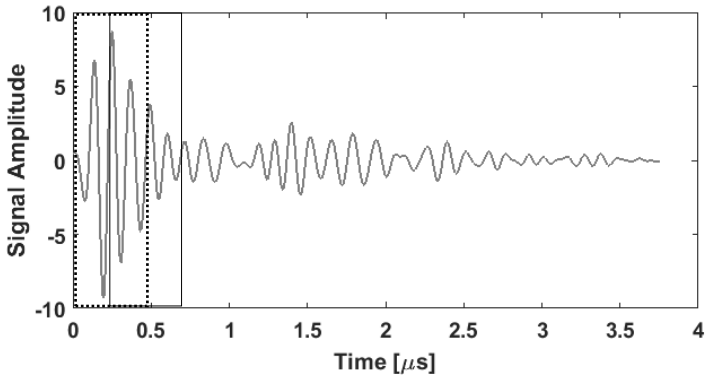

Figure 2-4 The first two time-windows are shown for one of the time-shifted signals.

By integrating the squared value of signals over each time window, the backscattered intensity $I_{ij}(T)$ was obtained:

$$I_{ij}(T) = \int_{T-\Delta/2}^{T+\Delta/2} h_{ij}^2(t)dt \qquad \text{Equation 2-9}$$

Where T is the time at the center of the time window and Δ is the width of the time window. The backscattered intensity $I(X,T)$ was calculated by averaging $I_{ij}(T)$ over the emitter-receiver pairs separated by the same distance $X = |X_{emitter} - X_{receiver}|$ where $X_{emitter}$ and $X_{receiver}$ indicated the location of the emitter and receiver elements, respectively. The initial part of the reflected intensity corresponds to the reflection [117] that takes place mainly at the first water-bone interface. Accordingly, data associated with the first time window ($0.5\mu s$) is cut out of the intensity matrix $I(X,T)$ to remove the initial part caused by reflection. At each time-window a typical backscattered intensity versus emitter-receiver distance (Figure 2-5) exhibits a steep peak (coherent contribution) over a wider pedestal (incoherent contribution), as described in [113]. The growth of the incoherent contribution over time provided

access to the diffusion constant[113]. To separate the two (coherent and incoherent) contributions, an antisymmetrization method was used[91]. Signals were first rewritten as:

$$h_{ij}^{A} = h_{ij}, \text{ for } i > j, \qquad \text{Equation 2-10}$$

$$h_{ij}^{A} = -h_{ij}, \text{ for } i < j,$$

$$h_{ij}^{A} = 0, \text{ for } i = j.$$

It can be shown[91] that the incoherent contribution of the backscattered intensity is:

$$I_{inc} = \frac{1}{2}(I + I^{A}) \qquad \text{Equation 2-11}$$

Where I^{A} is the backscattered intensity derived from H^{A}. For highly scattering media, the incoherent intensity can be approximated as follows [91]:

$$I_{inc}(X,T) \simeq (4\pi DT)^{-\frac{1}{2}} I(X,T) \exp\left(-\frac{X^2}{4DT}\right), \qquad \text{Equation 2-12}$$

Where D represents the diffusion constant and the term $\exp(-X^2/4DT)$ describes the temporal evolution of the incoherent intensity. To retrieve the constant D, a Gaussian curve was fitted to the function I_inc (X,T) at each time window (Figure 2-6). It was then normalized with respect to its maximum and its standard deviation was obtained. According to

Equation 2-12, the variance or squared standard deviation of the Gaussian curves over time follows a linear trend with slope equal to 2D. Identifying this slope with a linear fit allowed to measure D for all Ct.Po.Dm-Ct.Po.Dn combinations. All data processing was performed using Matlab 2016 (Mathworks, Inc., Natick, Massachusetts, United States).

Associations between D and the micro-structural parameters Ct.Po.Dm and Ct.Po.Dn were characterized in terms of the coefficient of determination R^2 and the root mean square error with respect to a power-law fit of the data. A Spearman rank correlation test was also performed to evaluate the monotonic relationship between D and those parameters.

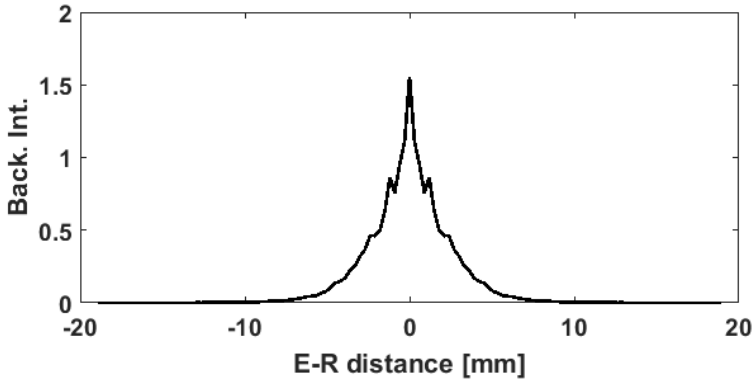

Figure 2-5 Backscattered intensity vs. emitter-receiver distance for a given time window T. A sharp peak corresponds to the coherent contribution and wider pedestal corresponds to the incoherent contribution of intensity.

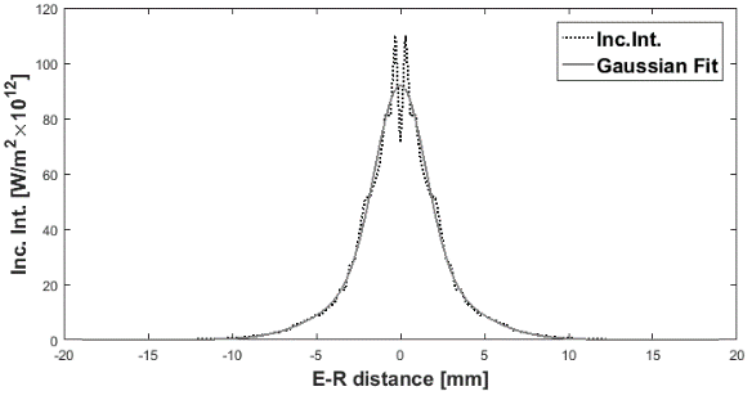

Figure 2-6 The incoherent intensity for a given time window T is fitted with a Gaussian curve.

2.4.2.4 Data acquisition and calculation of the diffusion constant in cortical bone (experimental study)

A linear array transducer (4DL14-5/38, Ultrasonicx, Richmond, Canada) was located against the tibia bone of patients transversely. Using the Ultrasonix Touch (BK Ultrasound) scanner, pulses with the central frequency of 7.8 MHz were transmitted using one element at a time, and the backscattered signals were received on all 128 elements. The process was repeated to obtain the inter-element response matrix. IRM for 49 patients was acquired. The image of the bone was constructed using the IRM and the surface of the bone was selected to determine which elements should be used for further processing the data considering that the size of the transducer (~4cm) is usually larger than the overall width of the tibia bone. Figure 2-7 depicts the detected bone surface of the tibia bone of a patient.

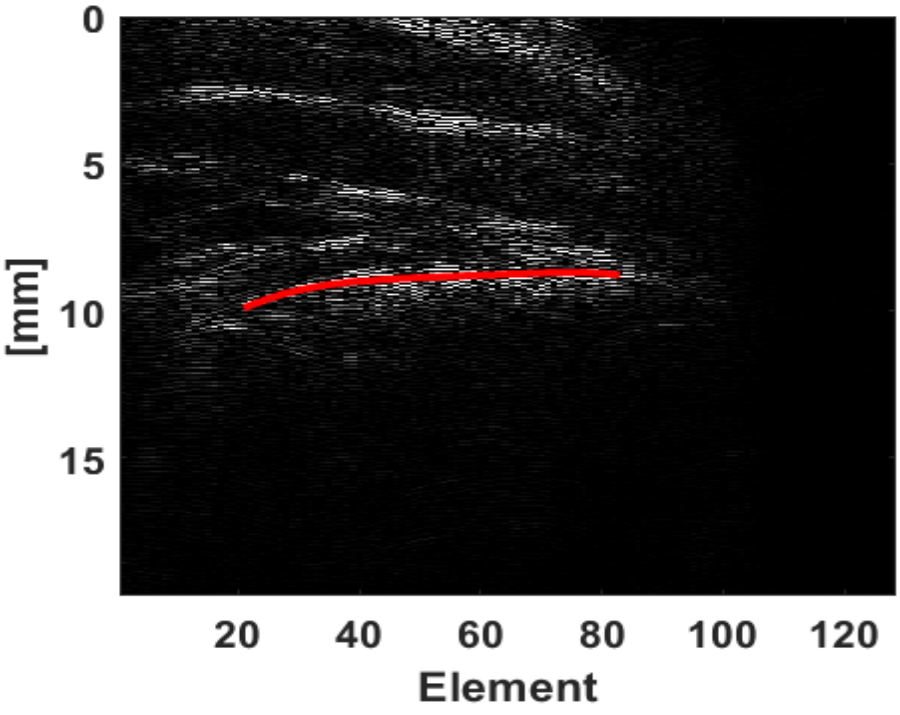

Figure 2-7 Bone surface is shown by the red line.

For each emission, the received signals were time-shifted so that the signals from the surface of the bone start at time $t = 0$ (Figure 2-8.b). While the signals received from the bone-muscle interface had relatively high amplitude, it was challenging and complicated to perform time-shifting using a simple threshold for feature detection. The reason was that the attenuation and the presence of ligaments and muscle layers affected the clarity of the signals. The larger the distance between the emitter and receiver, the more complicated this issue was. To overcome this problem, a second order polynomial curve was fitted to the profile of the received signals from bone for each emission event and the signals were shifted accordingly (Figure 2-8.a).

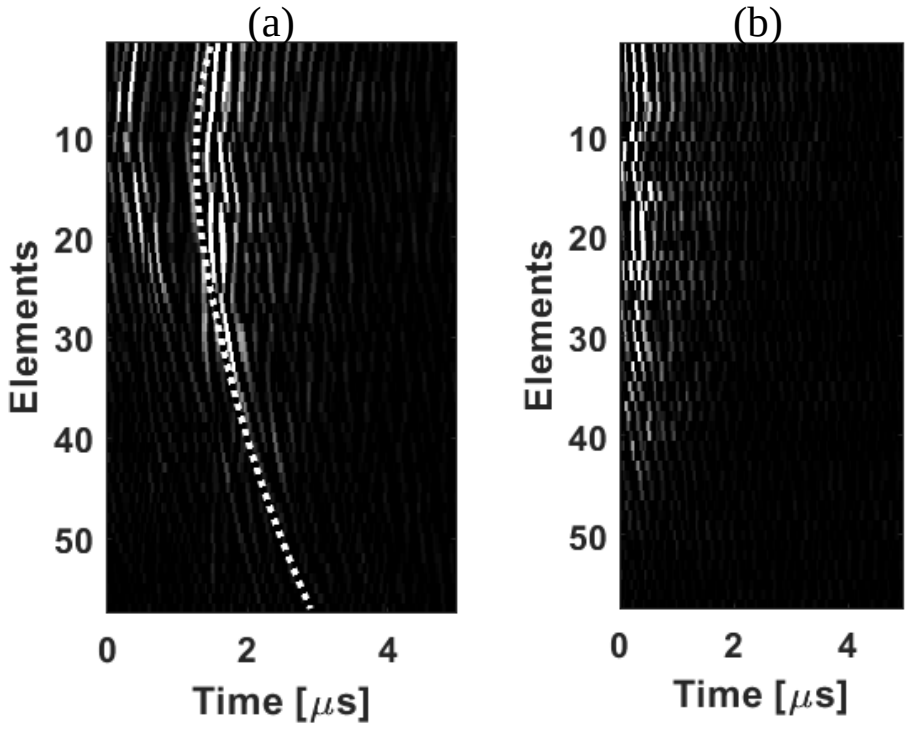

Figure 2-8 (a) Received signals for one emission event. The dashed line illustrates the polynomial fit associated with the signals from bone surface. (b) The time-shifted signals for the same emission event.

The total backscattered intensity (Figure 2-9.a) was calculated following the method elaborated in section 2.4.2.3. The length of the time-windows was $0.5\mu m$ and they had a 50% overlap. As mentioned previously, the total backscattered intensity at each time-window, was comprised of a steep peak which was the coherent contribution over a wider pedestal which was the incoherent contribution of the intensity. To separate the coherent peak from the incoherent part, at each time-window, the backscattered intensity was normalized with respect to its maximum. Then, its slope over the emitter-receiver range of 0 to 4.5mm was calculated and by setting a threshold (0.17), the wider and smoother part of the intensity was detected as the incoherent contribution which was fitted with a Gaussian curve subsequently (Figure 2-9.b). The reason was that the temporal growth of the diffusive halo (incoherent intensity) can be estimated with a Gaussian relation as explained in section 2.4.2.3. Variance of the Gaussian curves increases linearly as a function of time and the slope of the variance-time linear fit, gives 2 ×D.

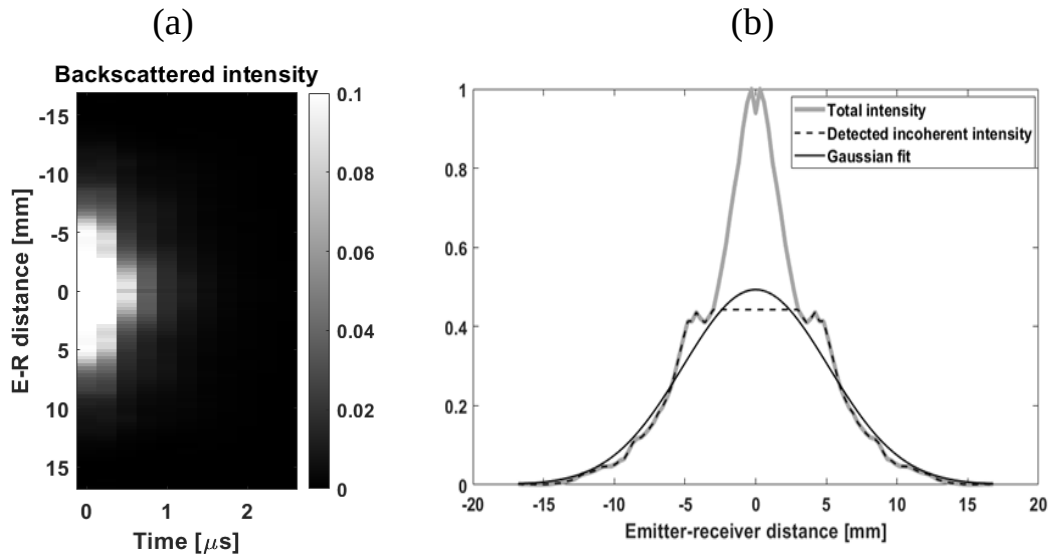

Figure 2-9 (a) Backscattered intensity, (b) the total intensity, detected incoherent contribution and its Gaussian fitted curve at time $t = 0.25\mu s$.

2.4.3 Results

2.4.3.1 Numerical simulations

The reference SAM image of a femur of a 71 year old male donor had average Ct.Po.Dm = 60.7μm (min=11.28μm; max=525.76μm; std=44.31μm), Ct.Po.Dn = 19.83 $\frac{pore}{mm^2}$ and porosity = 8.79%, before porosity manipulation. To confirm the choice of pixel size, one structure (modified from the original reference SAM image) with Ct.Po.Dm =30μm, Ct.Po.Dn=10 $\frac{pore}{mm^2}$ and the pixel size of 10μm was resampled down to 5μm. Results for D were compared for the two pixel sizes of 10μm and 5μm. A 2% difference in D was found between simulations run with a 5 μm pizel size and simulations run with a 10 μm pixel size, while the computational cost for the smaller pixel size indicated a 700% increase. In addition, the signals corresponding to emitter 32 and receiver 32 were compared for that image with the two mentioned pixel sizes. The root mean square error of the difference was 2%. Results suggest that 10μm was a reasonable pixel size that allowed to maintain accuracy while mitigating computational costs.

The selected time-window length for all the simulations was 0.5μs. The choice of time-window length was evaluated by comparing the obtained diffusion constant values for 7 different time-windows ($\Delta \in [0.25, 0.4, 0.5, 0.6, 0.7, 0.8, 0.9, 1]\mu s$) for a structure with average Ct.Po.Dm = 60μm and Ct.Po.Dn = 10$\frac{pore}{mm^2}$. The coefficient of variation (CV$= 100 \times (\frac{std}{mean})$) of D for those given time-windows, was 1.59% suggesting that a variation of the time window has a minor effect on D. Hence $\Delta = 0.5\mu s$ was an acceptable time-window.

In Figure 2-10, the incoherent intensity (in grey shade) is plotted as a function of time and receiver-transmitter distance, for two images modified to have different average Ct.Po,Dm. The growth of the diffusive halo over time is larger for the sample with smaller pore size (and lower porosity). The variance of the Gaussian fit of the incoherent intensity was obtained at each time widow, for two different structures (Figure 2-11). As explained in the previous section, this variance is expected to increase linearly with time. The slope of its linear fit, which is proportional to the diffusion constant, was smaller for the structure with higher porosity (Figure 2-11). When pore density was kept constant (Figure 2-12), the diffusion constant decreased as the average pore size increased. A power law was fitted to model the D-Ct.Po.Dm relation: $D = 285.9 Ct.Po.Dm^{-1.49}$ $(R^2 = 0.99, p = 4.96 \times 10^{-5}, RMSE = 0.06)$. In Figure 2-13, the diffusion constant for samples with constant Ct.Po.Dm of $60\mu m$ is plotted for different pore densities. A power fit of this plot provided the relation $D = 6.91 Ct.Po.Dn^{-1.01}$ $(R^2 = 0.94, p = 2.8 \times 10^{-3}, RMSE = 0.09)$, between D and Ct.Po.Dn.

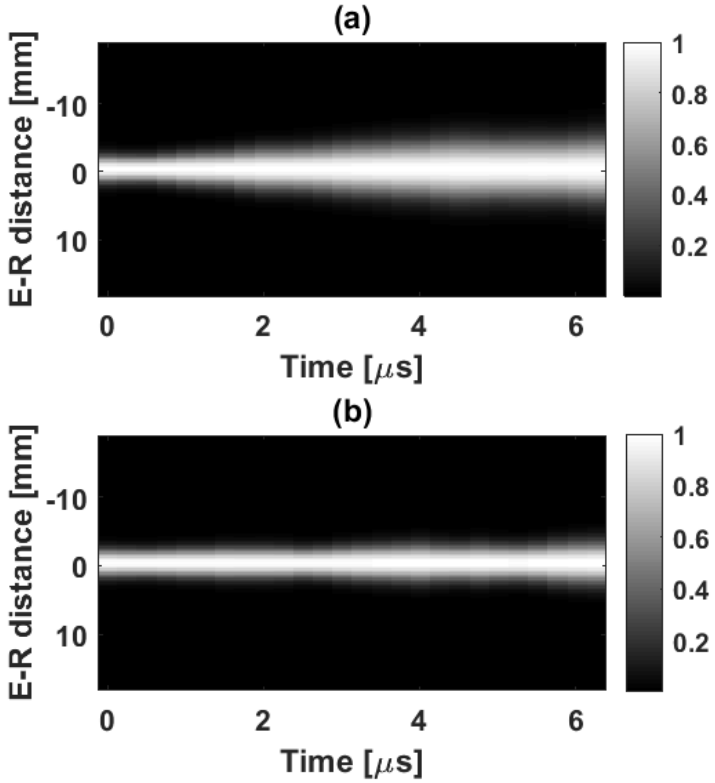

Figure 2-10 Incoherent intensities corresponding to bone samples with pore density of 10 pore/(mm^2) and mean pore diameter of 50 μm (a) and 90 μm (b) are shown. The growth of the incoherent intensity is more pronounced for the sample with smaller pore size.

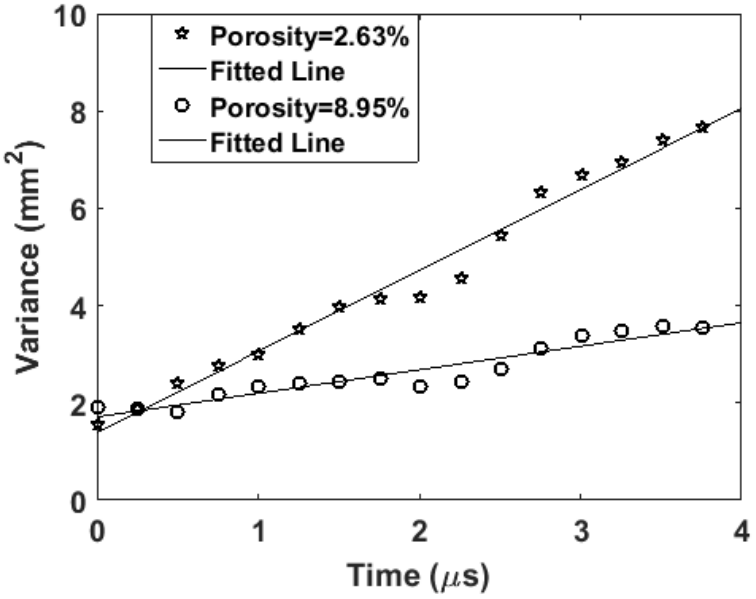

Figure 2-11 Variance of the Gaussian fit of the incoherent intensity versus time for bone samples with 8.95% and 2.63% porosity (Ct.Po.Dn =10 pore/(mm^2) , Ct.Po.Dm_circles= 90 μm , Ct.Po.〖Dm〗_stars= 50μm). The variance increases at a higher rate for the sample with lower porosity.

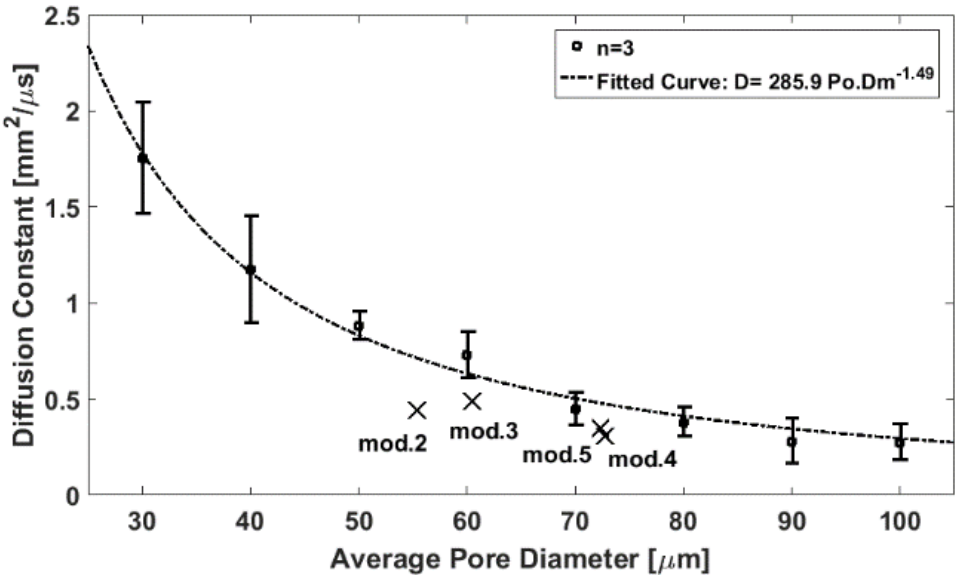

Figure 2-12 Diffusion constant for samples with Ct.Po.Dn of 10 pore/(mm^2) and different pore sizes. Error bars are associated with 3 different generated geometries for each size-density combination. Fitted Curve: D=285.9Ct.〖Po.Dm〗^(-1.49) ; R^2=0.989, p=4.96×〖10〗^(-5) , RMSE = 0.06. Results from modified femur SAM images of other donors are shown by crosses (mod2: Ct.Po.Dn = 10 pore/(mm^2) Ct.Po.Dm = 55.34 μm. mod3: Ct.Po.Dn = 10 pore/(mm^2), Ct.Po.Dm = 60.48μm. mod4: Ct.Po.Dn = 10pore/(mm^2), Ct.Po.Dm = 72.70μm. mod5: Ct.Po.Dn = 10pore/(mm^2), Ct.Po.Dm = 72.29μm).

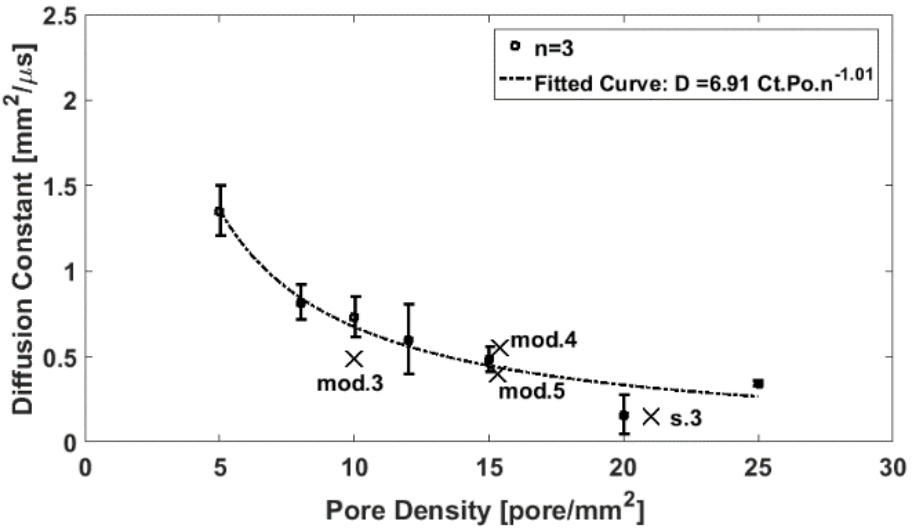

Figure 2-13 Diffusion constant for samples with average Ct.Po.Dm of 60μm and different pore densities. Error bars are associated with 3 different generated geometries for each size-density combination. Fitted Curve: D=6.91Ct.Po.〖Dn〗^(-1.01); R^2=0.94 , p=2.8×〖10〗^(-3), RMSE = 0.09. Results from SAM images of other donors are indicated by crosses. Results from modified femur SAM images of other donors are shown by crosses (mod3: Ct.Po.Dn = 10pore/(mm^2), Ct.Po.Dm = 60.48μm. mod4: Ct.Po.Dn = 15pore/(mm^2), Ct.Po.Dm = 59.84μm. mod5: Ct.Po.Dn = 15.34pore/(mm^2), Ct.Po.Dm = 60.19μm. s3: Ct.Po.Dn = 21pore/(mm^2), Ct.Po.Dm = 59.16μm).

The average and standard deviation of the diffusion constant D for all the structures were 0.69 $\frac{mm^2}{\mu s}$ and 0.47 $\frac{mm^2}{\mu s}$ respectively. The p values for the Spearman correlation between D and parameters Ct.Po.Dm and Ct.Po.Dn were 4.96×10^{-5} and 2.8×10^{-3} respectively; suggesting significant correlations and monotonous relationships between D and those micro-structural parameters.

To account for individual differences, additional femur SAM images from other donors were used in simulations to obtain the diffusion constant values. Table 2-2 summarizes the results. Results from the modified versions of those samples at Ct.Po.Dn=10$\frac{pore}{mm^2}$ and average Ct.Po.Dm=60μm are presented in Figure 2-12 and Figure 2-13 respectively, and summarized in Table 2-2.

Table 2-2 Diffusion constant values for bone samples from different donors.

	Average Ct.Po.Dm (μm)	Ct.Po.Dn ($\frac{pore}{mm^2}$)	D ($\frac{mm^2}{\mu s}$)
Sample 1 (original sample modified to obtain figures 9 and 10)	60.7	19.83	0.09
Sample 2	55.43	16.52	0.24
Modified sample 2 (Ct.Po.Dn artificially reduced to $10\frac{pore}{mm^2}$)	55.34	10.01	0.44
Sample 3	59.16	21.00	0.15
Modified sample 3 (Ct.Po.Dn artificially reduced to $10\frac{pore}{mm^2}$)	60.48	10.00	0.49
Sample 4	72.92	15.53	0.25
Modified sample 4 (Ct.Po.Dn artificially reduced to $10\frac{pore}{mm^2}$)	72.70	10.02	0.31
Modified sample 4 (average Ct.Po.Dm artificially reduced to $60\mu m$	59.84	15.39	0.55
Sample 5	71.42	15.74	0.22
Modified sample 5 (Ct.Po.Dn artificially reduced to $10\frac{pore}{mm^2}$)	72.29	10.02	0.35
Modified sample 5 (average Ct.Po.Dm artificially reduced to $60\mu m$	60.19	15.34	0.40

2.4.3.2 In-vivo experiments

The backscattered data was acquired from the tibia bone of 49 female patients aging from 56 to 86 (mean age: 69 ± 7 y) and D was calculated by exploiting the temporal growth of the incoherent intensity as instructed in section 2.4.2.4. Figure 2-14.a illustrates the incoherent intensity normalized with respect to its maximum at each time-window. The variance of the Gaussian fitted curves at each time-window increases linearly with time as shown in Figure 2-14.b. D is half of the slope of the variance-time linear fit.

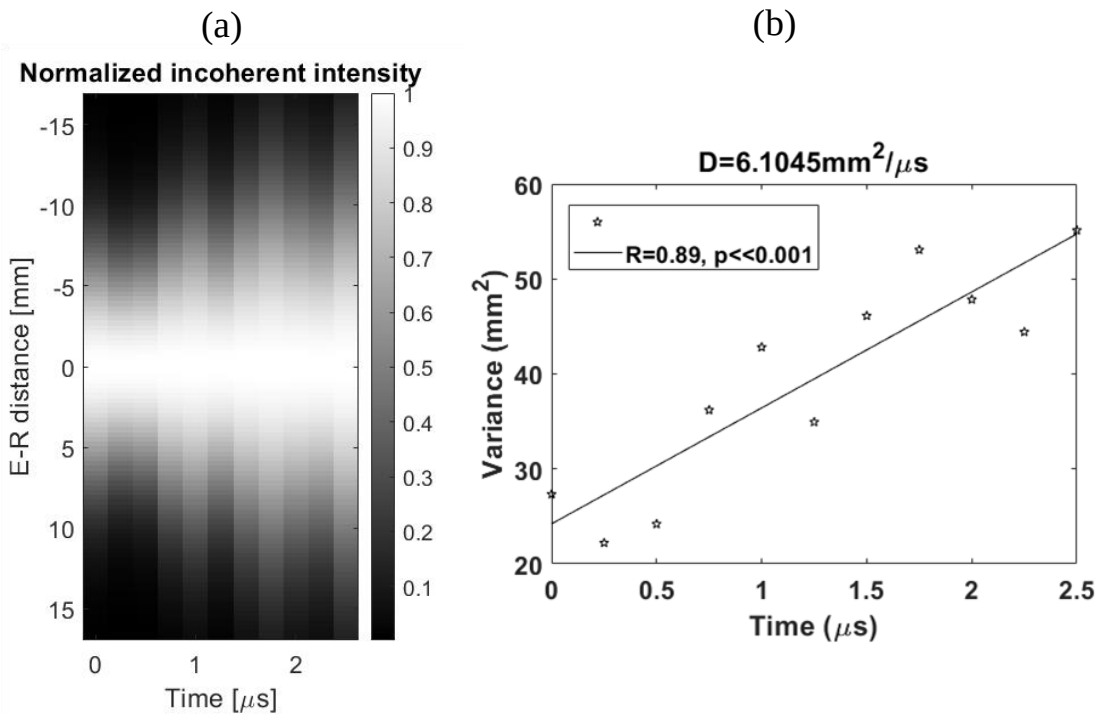

Figure 2-14 (a) Normalized incoherent intensity. (b) Variance-time linear fit gives 2D.

Figure 2-15 summarizes the results for D (mean: $4.96 \pm 1.93 \frac{mm^2}{\mu s}$) versus structural parameters Ct.Po. (mean: 15.89 ± 3.94 %), average Ct.Po.Dm. (mean: $125.87 \pm 18.32\ \mu m$),

Ct.Po.Dn. (mean: $1.58 \pm 0.65 \frac{pore}{mm^2}$) and vBMD (mean: $990.33 \pm 42.70 \frac{mg}{cm^3}$) measured using HRpQCT for 48 out of 49 patients. D associated with one of the patients was rejected as outlier due to large discrepancy (>200%) between that and the mean D for the rest of the patients. Contrary to the simulation results, here the correlation between the structural parameters and D was not significant (p>0.05). Possible explanations are provided in the discussion section.

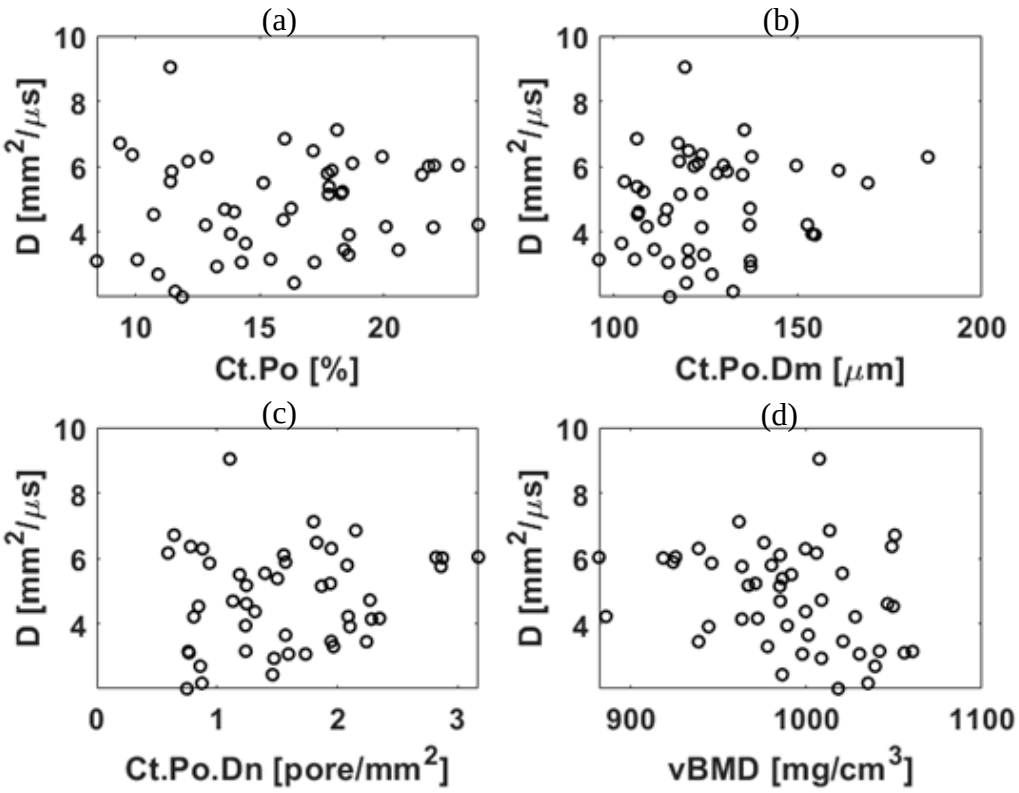

Figure 2-15 D vs (a) CT.Po., (b) average CT.Po.Dm, (c) Ct.Po.Dn. and (d) vBMD.

2.4.4 Discussion

2.4.4.1 Numerical simulations

High-resolution Scanning Acoustic Microscopy images of human cortical bone were processed to model the ultrasound backscatter from cortical bones with different pore densities and pore diameters.

The diffusion constant was calculated for different cortical microstructures by measuring the growth rate of the incoherent portion of the backscattered intensity over time. The effects of pore size and pore density on the diffusivity of the medium were studied independently. Increasing average Ct.Po.Dm and Ct.Po.Dn both resulted in a significant and consistent decrease in the diffusion constant. This result suggested that the diffusion constant as assessed by quantitative ultrasound could be used to characterize the cortical bone microstructure, with potential applications to diagnosis and monitoring of osteoporosis. Our results showed that an increase in either pore size or pore density contributes to higher number of scattering events taking place in the medium, leading to lower diffusion constants.

In healthy bone, the average diameter of Haversian canals ranges from about 40 to 100 μm [104,126]. Results from a study on femur neck biopsies suggests that osteonal canals with diameters as large as 172 μm exist in cortical bone. However, such large pores contribute to only about 2.5% of the total pore population [135]. For this reason, the mean Ct.Po.Dm did not exceed 100 μm in our simulations. Our findings demonstrated that the acoustic diffusion constant of cortical bone was strongly related to the average pore diameter, in the healthy Ct.Po.Dm range (30-100 μm; Figure 2-12; $R^2_{powerlaw} = 0.98$). Similarly, the acoustic diffusion constant was highly dependent (Figure 2-13; $R^2_{powerlaw} = 0.94$) on variations of the pore

density in the 5-25 $\frac{pore}{mm^2}$ range which was close to the ranges reported in the literature (6-30$\frac{pore}{mm^2}$) [127,136].

The present study, evaluates the diffusion constant as a tool to evaluate changes in the porous microstructure of cortical bone. Ct.Po.Dm and Ct.Po.Dn combined are related to porosity (ie the ratio of pore volume over total volume) which is a major determinant of the tissue mechanical properties and resistance. However, the specific focus of this study was to evaluate the independent effects of Ct.Po.Dm and Ct.Po.Dn on D. The numerical procedure utilized here has the advantage of providing full control over the cortical porosity by allowing the manipulation of pore density and pore size independently.

To account for the effect of individual differences, results from four femur images in addition to the original reference image (sample 1) are presented in Table 2-2. For each sample, a reduction of Ct.Po.Dn, caused an increase in D. For samples 4 and 5, a reduction of average Ct.Po.Dm, increased the diffusion constant value, indicating that higher pore sizes are associated with less diffusive regimes. Comparison between samples 2, 4, 5 and Ct.Po.Dm-reduced versions of samples 4 and 5, indicated that for relatively high pore densities (Ct.Po.Dn≈ 16 $\frac{pore}{mm^2}$), the diffusion constant did not present a monotonous behavior. An increase in Ct.Po.Dn for samples from different donors at Ct.Po.Dn=10$\frac{pore}{mm^2}$, resulted in a decrease in D (Figure 2-13) which was in accordance with the results from modified versions of sample 1. As shown in Figure 2-12, an increase in Ct.Po.Dm resulted in an overall decrease in D for samples from other donors (crosses) as well as the modified versions of the reference SAM image (sample 1). However, results from modified femur images of other donors indicated slightly smaller values for D compared to the results from sample 1. Different factors

such as the shape of the bone, local concentration of the pores close to the periosteal region, and presence of relatively large pores (Ct.Po.Dm>$300\mu m$) may have resulted in slightly different diffusion constant values for different samples with the same average Ct.Po.Dm and Ct.Po.Dn.

Our approach is affected by several limitations. First, our simulations did not model absorption and the decay of the backscattered signals was only due to scattering. We expect absorption to affect the correlations between acoustic diffusion and cortical bone microstructure reported here, to an extent that is yet to be determined. The main reason for neglecting absorption in our simulations of ultrasound backscatter was the lack of a reliable numerical model for absorption of shear waves. The influence of absorption should be addressed in future studies. The effect of cortical thickness (ranging from 0.25 to 6 mm [137]) on the diffusion constant could also be investigated in the future, considering the fact that thinning of the cortical shell is one of the signs of osteoporosis. However, it is worth noting that in our simulations, no second echo (from the inner cortical wall) was observed. This, is attributed to high amounts of multiple scattering at the operating frequency of the simulations. Another point to notice is that the size of the time-window for integration of the backscattered intensity must be small enough to allow for analysis of the intensity while having the adequate length to include at least one scattering event. Thus, pre-existing knowledge regarding the length of the scattering mean free path, and therefore of the range of pore diameter and density, is beneficial when choosing the length of the time window. The time window used in processing the data corresponds to four wavelengths in the solid phase. However, changing its length for one of the structures from 0.25μs to 1μs did not have a significant effect on D (CV=1.59%). The material properties of the two phases (bone and water) were assumed to be homogeneous

within the same bone and for all simulations. This is not the case in real bone. 2D simulations like those performed in this study represent a strong simplification of the highly heterogeneous 3D bone structure, mainly because they fail to model out-of-plane diffraction and out-of-plane scattering [138]. While 3D simulations could provide more accurate models, they could not be done because of their excessive computational cost. Supported by the translational symmetry of cortical bone pores in the diaphysis of long bones, we assumed 2D models to hold validity. Finally, adding a layer of soft tissue surrounding the bone would also improve the simulations in terms of mimicking in-vivo experiments. Considering all the simplifying assumptions, it is worth noting that the main purpose of this study is to reveal the existence of a monotonous relation between micro-structural parameters and D in a qualitative context rather than a quantitative one. The power-law fits are exclusively used to show the decreasing, monotonous trend that D manifests as Ct.Po.Dm or Ct.Po.Dn increase, rather than to predict an exact quantitative relationship between D and the pore size-density combination. This will be the subject of future studies, which will combine numerical, experimental and analytical methods.

2.4.4.2 In-vivo experiments

Contrary to the simulation study, the changes in the micro-structural parameters Ct.Po., Ct.Po.Dm., Ct.Po. did not result in monotonous behavior in D. One possible explanation could be the limitations that are associated with the HRpQCT. Since the resolution of HRpQCT ($60\mu m$) was relatively large compared to the physiological range of the cortical average pore diameter (40-100μm [126]), smaller pores were not accounted for in our experimental study. Hence, the presented micro-structural parameters (Ct.Po.Dm., Ct.Po.Dn. and Ct.Po.), may not have provided an accurate representation of cortical bone. This is especially a valid point

considering the reported range of the cortical pore density (6-30 $\frac{pore}{mm^2}$ [136,139]) and pore diameter (40 to 100 μm [104,126]) in the literature. This means that while based on our HRpQCT data, the results of average Ct.Po.Dm. for two patients is different, if we take the smaller pores into account, they might have quite the same average Ct.Po.Dm. resulting in very small deviation in D (as it is observed in Figure 2-15.b). The same explanation would apply to Ct.Po.Dn. and Ct.Po. with which D was not significantly correlated. Ct.Po.Dn. in particular did not have large variance (mean: $1.58 \pm 0.65 \frac{pore}{mm^2}$), so regardless of the resolution limitations, it was expected to get similar D values. The limitations regarding the CT resolution are especially important because they result in overestimation of the average pore diameter and based on our simulation results in section 2.4.3.1, D does not vary significantly when diameter is high. Hence, the findings from the in-vivo study are aligned with our findings from the simulations. It is worth noting that our collaborators have confirmed that ultrasound backscatter and attenuation coefficients also do not demonstrate significant correlations with micro-structural parameters obtained from HRpQCT, however, those attenuation and backscatter coefficient are in association with the fracture incidents. An ongoing study is being done to evaluate the correlation between the fracture risk and D.

2.4.5 Conclusion

The current numerical study takes advantage of multiple scattering of ultrasound in diffusive media to measure the diffusion constant in cross-sections of cortical bone. Scanning acoustic microscopy images of human proximal femur shaft cross sections were modified to control the average cortical pore diameter and density. *In-silico* the diffusion constant was found to be monotonously influenced by both scatterer size and density. These results support

the use of ultrasound multiple scattering for the assessment of cortical bone, and proposes the acoustic diffusion constant as a potential tool for the characterization of the cortical bone microstructure. While due to limitations with in-vivo HRpQCT imaging we have not yet been able to effectively use D as a clinical diagnostic tool, an ongoing study is being done on low-trauma incident fractures and their correlation with D, as well as other parameters such as attenuation and backscatter coefficient.

2.5 Diffusion constant measurement in feline kidney

Chronic kidney disease (CKD) is very common in cats. The gold standard indicator of kidney function to assess feline chronic kidney disease (CKD) is glomerular filtration rate (GFR) which is relatively demanding in terms of time and resources[140]. Cats with chronic kidney disease are staged using urine and blood tests which are not able to detect changes in renal perfusion, or the presence of tubulointerstitial fibrosis, both of which have been described as factors that may lead to progression and development of end-stage kidney disease. Hence, development of a non-invasive approach to evaluate micro-structure of the kidney may be beneficial. Contrast enhanced multiple scattering ultrasound is used to measure the diffusion constant in cat kidneys which is expected to be influenced by changes in vascularization and contrast agent population.

2.5.1 Methodology

20 cats with any stage of CKD are prospectively recruited from the NC State University College of Veterinary Medicine community and through referring clinics. 23 healthy cats without CKD are recruited from the same population as negative controls. All patients undergo a physical examination and blood pressure analysis. Patients with CKD are categorized to control and stage 1, 2, 3, and 4 groups. B-mode ultrasound is performed to locate the kidney, then 0.05 ml Definity ultrasound contrast is bolus-injected. Pulses are transmitted at the central frequency of 5.2 MHz and the backscattered response is recorded using an array transducer (L7-4). The process of data acquisition and calculation of D is explained in details in section 2.4.2.3. Figure 2-16 indicates the data acquisition process, b-mode and contrast enhanced images of a feline kidney.

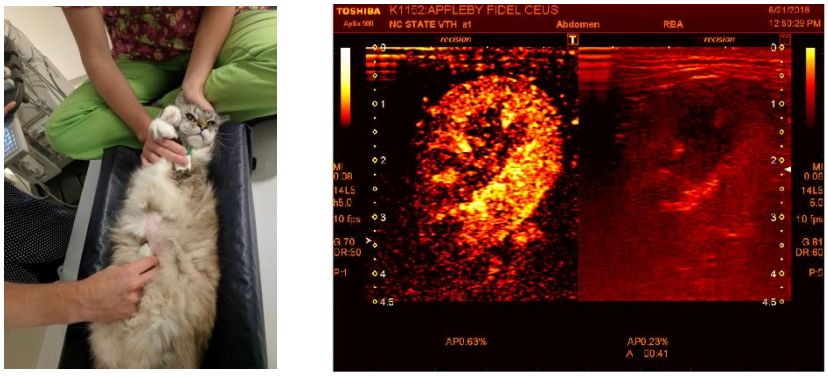

(a) (b)

Figure 2-16 (a) Data acquisition from the kidney. (b) left: Contrast enhanced image; right: B-mode image.

2.5.2 Results/Discussion

A total of 43 cats are evaluated with ultrasound multiple scattering (23 controls, 10 stage 1, 10 stages 2-4). Figure 2-17 summarizes the D results for control, stage 1 and stage 2-4 CKD cats. A significant decrease ($p=0.0021$) in diffusion constants (D) is present in cats with stages 2-4 chronic kidney disease (mean D: 1.04 $mm^2/\mu s$) when compared to control cats (mean D: 1.69 $mm^2/\mu s$) and cats in stage 1 CKD (mean D: 1.77 $mm^2/\mu s$). Reduction in kidney size and increase of structural abnormalities could have caused an increase in vascularization, leading to more multiple scattering by the microbubbles and consequently lower D values for stage 2-4 CKD cases. D seems to effectively characterize the healthy and diseased cases. To strengthen the present study, a larger population with higher number of stage 2-4 CKD cases needs to be evaluated. In addition, the histology data of the kidneys can shed light on the changes in the micro-structure and vascular system to further validate our results. Unfortunately, we were not able to acquire the histology data.

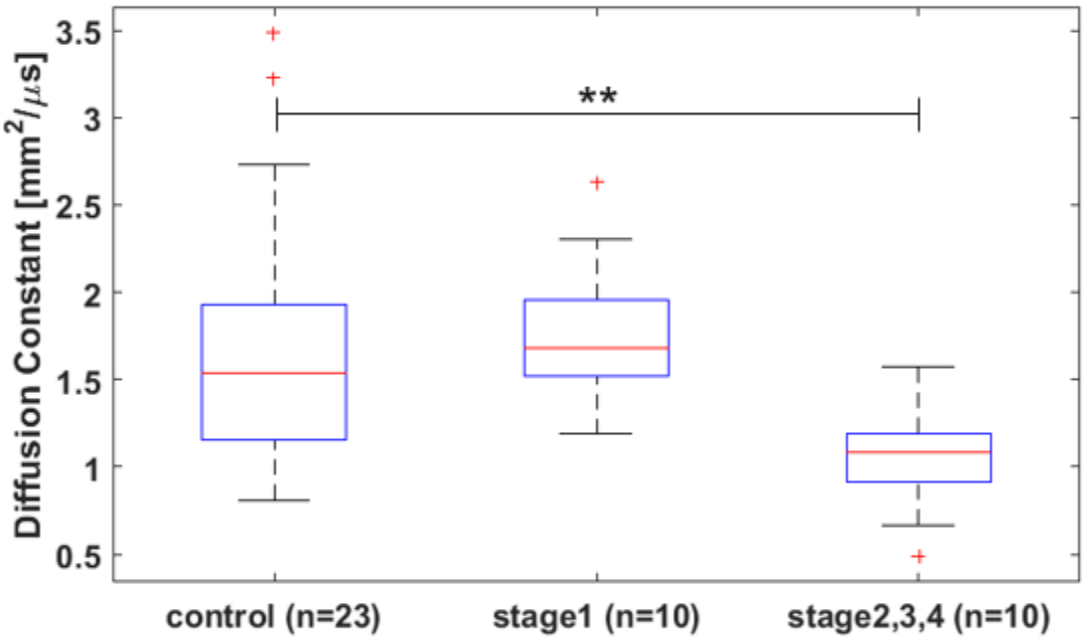

Figure 2-17 Diffusion constant for control, stage 1 and stage 2-4 CKD cats.

Chapter 3: Frequency-dependent analysis of ultrasound apparent absorption coefficient in porous structures (application to cortical bone)

The effect of matrix viscoelastic absorption on frequency-dependent attenuation in porous structures mimicking simplified cortical bone is addressed in this numerical study. An apparent absorption is defined to quantify the difference between total attenuation (resulting from both absorption and scattering) and attenuation exclusively due to scattering. A power-law model is then used to describe the frequency-dependent apparent absorption as a function of pore diameter and density. The frequency response of the porous structures to a Gaussian pulse is studied to determine the frequency range over which the system can be considered linear. The results show that for low scattering regimes (normalized frequency < 0.80), the system and its apparent absorption can be considered linear. Hence, the total attenuation coefficient results from the summation of scattering and absorption coefficients. However, for highly scattering regimes, the system can no longer be considered linear, as the apparent absorption vs. frequency deviates from a linear trend. To study the independent effect of change in pore size and pore density on attenuation, this parameter and its scattering and absorption contributions are estimated in porous structures with varying pore diameters ($\phi \in [40,120]\mu m$) and pore densities ($\rho \in [5,25]\frac{pore}{mm^2}$) at 5MHz and 8MHz. Results show that both scattering and absorption contribute to the total attenuation. They also illustrate that, although absorption only occurs in the solid matrix, the apparent absorption $\alpha_{app.abs}$ is a function of porosity, presumably due to the presence of multiple scattering. For large values of $k\phi$, an increase in pore size or density does not lead to increase in α_{scat} and only results in an increase

of the total attenuation as a result of increase in $\alpha_{app.abs}$. On the other hand, in low/intermediate scattering regimes, an increase in either pore size or pore density results in increase in α_{scat} while $\alpha_{app.abs}$ remains constant.

3.1 Introduction

Osteoporosis is a common bone disease characterized by the deterioration of bone tissue due to aging, menopause and certain medications which results in an increase in bone susceptibility to fracture. Long bones are generally comprised of a compact cortical shell surrounding trabecular bone which is a network of interconnected rods in a marrow matrix. It has been shown that osteoporosis changes the micro-structure of both cortical and trabecular bone[141,142]. While trabecular bone is metabolically more active, the load-bearing capacity of cortical bone in long bones, and the link between cortical porosity and bone mechanical properties[101,103–106,143–145], indicate the importance of evaluating cortical bone for fracture risk assessment. In cortical bone, osteoporosis commonly leads to an increase in pore size and is related to changes in pore concentration, although large merging pores can lead to lower pore densities[146,147].

Quantitative ultrasound (QUS) is a non-invasive radiation-free modality that has been playing an increasing role in osteoporosis assessment[148]. It not only provides information on bone mass but also on bone micro-architecture and mechanical competence[149] which are recognized to be relevant markers of bone quality[150].

The focus of QUS studies on cortical bone has mainly been on the measurement of speed of sound and investigation of wave propagation through wave velocity analysis[151,152]. In addition, other studies have focused on attenuation measurements of cortical bone in different

frequency ranges[44] which showed that even over a large bandwidth, the total frequency-dependent attenuation in cortical bone follows a linear regression .

Among QUS parameters, it has been shown that changes in pore size and pore concentration in cortical bone have a significant impact on attenuation[153]. Attenuation in porous media such as cortical bone is caused by scattering due to solid-fluid impedance difference at the pores on one hand, and absorption due to dissipative mechanisms in the solid matrix on the other hand. Scattering arises at the interface between inclusions, materials or grains with different elastic properties. These differences are associated with multiple phases, crystal defects from dislocations, grain structure, precipitates, etc[154]. The general problem of expressing attenuation due to scattering through a medium including scatterers with given size, shape, material property, and density of scatterers has been the subject of many studies. When the concentration of scatterers is low, the loss caused by a single scatterer is not affected by the presence of other scatterers. In that case, the scatterers are decorrelated and the total energy loss can be calculated from the single scattering. Single scattering is dominant and the scattering from an individual scatterer can be treated independently[154]. In that case, the combined scattering attenuation effect would simply be the arithmetic summation of individual scatterer contributions. On the other hand, when the concentration of scatterers is high, multiple scattering effects need to be taken into account and evaluating scattering attenuation is more complex. Assuming that absorption is negligible compared to scattering, multiple scattering theories have been previously used to estimate attenuation in trabecular bone[155]. However, this assumption may not be valid for cortical bone, where absorption plays a significant role in total attenuation as shown by Pinton[156] . Hence, an attenuation model which can incorporate both scattering and absorption is needed for cortical bone. Such a model, which

would accurately estimate the total frequency-dependent attenuation as a function of cortical porosity will potentially enable one to solve an inverse problem and get access to micro-structure of cortical bone from measuring attenuation. In another study by our group, the frequency-dependent attenuation due to scattering was modeled in media resembling cortical bone[157], but the effect of absorption on attenuation was not taken into account.

The aim of the present work is to address the effect of micro-structural changes of cortical bone on attenuation due to absorption. We first numerically mimic the simplified structure of cortical bone by assuming 2D mono-disperse pores, randomly distributed in absorbing bone tissue. For different combinations of pore size and pore concentration we simulate the wave propagation and estimate the total attenuation which comes from scattering and absorption. Then we use two scattering models to estimate the frequency-dependent attenuation and show how these two models fail to accurately predict attenuation due to combination of absorption and scattering. This justifies the need for accounting for absorption. In the next step we study the effect of scattering and absorption on total attenuation separately. This is done by simulating absorbing and non-absorbing bone tissue to isolate the effect of absorption on total scattering. We finally show that even though the multiple scattering theory can estimate the attenuation due to scattering, when scattering and absorption co-exist, the common assumption that a linear combination of scattering and absorption can describe attenuation fails in highly scattering regimes, where multiple scattering dominates. Instead, a parametric model accounting for the effect of micro-structure on absorption is proposed.

3.2 Methodology

3.2.1 Numerical Measurements

The SimSonic (www.simsonic.fr)[131] research freeware is used for 2D finite-difference time domain simulations to model wave propagation in slabs of porous media in order to estimate the frequency-dependent attenuation.

3.2.1.1 Simulation framework

Mono-disperse structures: To obtain different mono-disperse porous structures with a range of pore diameter (ϕ)- density (ρ) combinations, a Monte Carlo method[158] is implemented which randomly distributes fluid pores of a given diameter in a solid slab until the desired overall pore density is achieved. Overlap between pores is not allowed. Material properties of cortical bone (

Table 2-1) and water are assigned to the solid and fluid phases of the binary structures respectively. The ranges for pore diameter and densities are ($\phi \in [40,120]\ \mu m$) and ($\rho \in [3,25]\frac{pore}{mm^2}$) respectively, and correspond to the values found in the literature for cortical bone[139]. For each combination of diameter and density, 3 different structures are created to account for different realizations of the pore distribution. A total of 270 structures is created.

Poly-disperse Structures: Two computed tomography (CT) images obtained from human femoral bone are used to evaluate apparent absorption coefficient with respect to changes in $k\phi$ in poly-disperse media. The procedure of acquisition of the specimens and CT images is explained elsewhere[159].

Emitting pulse: Gaussian pulses with a central frequency within the spectroscopy range of 1 to 8 MHz with 0.5 MHz intervals and -6dB bandwidth of 20 percent are transmitted through the medium. 30 receivers are located throughout the depth of structure to record the signal as it propagates. The emitter and all of the receivers are large enough to cover the width of structure and the pores are homogeneously distributed. Hence, the transmitted wave is a plane wave, and the recorded signals are averaged over the whole width of the structure.

Length of the signal: To evaluate the time wave has been travelling in the medium, the length of the signals received by each one of the 30 receivers is obtained. To do so, first the signal is normalized with respect to its maximum, and by using a 0.0005 threshold, the beginning of the signal and end of the coda is found to measure the length of the signal.

Boundary conditions: Perfectly matched layers at the two ends of structure in the wave propagation direction reduce reflections from those boundaries. Symmetric boundary

conditions in the direction perpendicular to the wave propagation are implemented to eliminate diffraction and ensure plane wave transmission.

Simulation parameters: The grid step of $\Delta x = 10\mu m$ exceeds the 20 points per wavelength spatial sampling requirement proposed by[134] Bossy ensuring the accuracy of the simulation results while keeping the computational costs sufficiently low. Choosing CFL=0.99 (Courant-Friedrichs-Lewy), the temporal grid step is defined as:

$$\Delta l = 0.99 \frac{1}{\sqrt{d}} \frac{\Delta x}{c_{max}} \qquad \text{Equation 3-1}$$

Where Δx is the spatial grid step, c_{max} is the highest speed of sound in the simulation medium and d is the dimension of space (d=2 for 2D simulation).

3.2.1.2 Attenuation measurements

The attenuation coefficient is measured using the Time-Distance Matrix Approach (TDMA) described in previous work by the authors[153]. Briefly, the received signals in the time-domain recorded by 30 receivers are transformed into the frequency domain using Fast Fourier Transform (FFT). The magnitude of the signals in the frequency domain is recorded in a matrix $S(f, x)$ where x is the position of a given receiver and f represents the frequency. A Gaussian window with length of 200 points is then applied to the signals recorded by the receivers as the emitted Gaussian pulse propagates through the medium resulting in $S(f, x)$. The Gaussian window is used to smooth the received signals in frequency domain and give a more accurate estimation of the magnitude of the signal at each frequency (f) and receiver position (x).

Wave propagation in the structure is associated with energy loss which leads to an exponential decay of the signal[160]. Hence, the amplitude of the signals contained in the frequency-distance matrix can be approximated as follows:

$$|S(f,x)| = e^{-\alpha(f)x} \rightarrow \alpha(f) = -\frac{\ln|S(f,x)|}{x} \qquad \text{Equation 3-2}$$

As a result, the attenuation coefficient α can be obtained from the slope of a linear fit of $\ln|S(f,x)|$ vs. $-x$.

3.2.1.3 Spectroscopy

The spectroscopy analysis allows investigating the changes in attenuation with respect to frequency. Throughout this paper, we report the attenuation as a function of normalized frequency $k\phi$ where k is the wave number. This enables us to study the attenuation behavior in different scattering regimes ($k\phi$ <0.8: low scattering regime, 0.8< $k\phi$ <1: medium scattering regime, 1< $k\phi$: high scattering regime). Some scattering models such as the Independent Scattering Approximation are suited for specific scattering regimes and cannot be expected to describe the attenuation in other regimes accurately[157]. For each pore diameter-density combination, 16 different simulations are executed to investigate the whole spectroscopy range (1-8 MHz frequency range with 0.5 MHz intervals). For each simulation, a new structure is generated to obtain different realizations of a given pore size-density combination, in order to

take randomness of the distributions into account. An example of a simulated structure and the emitted signal are depicted in Figure 3-1.

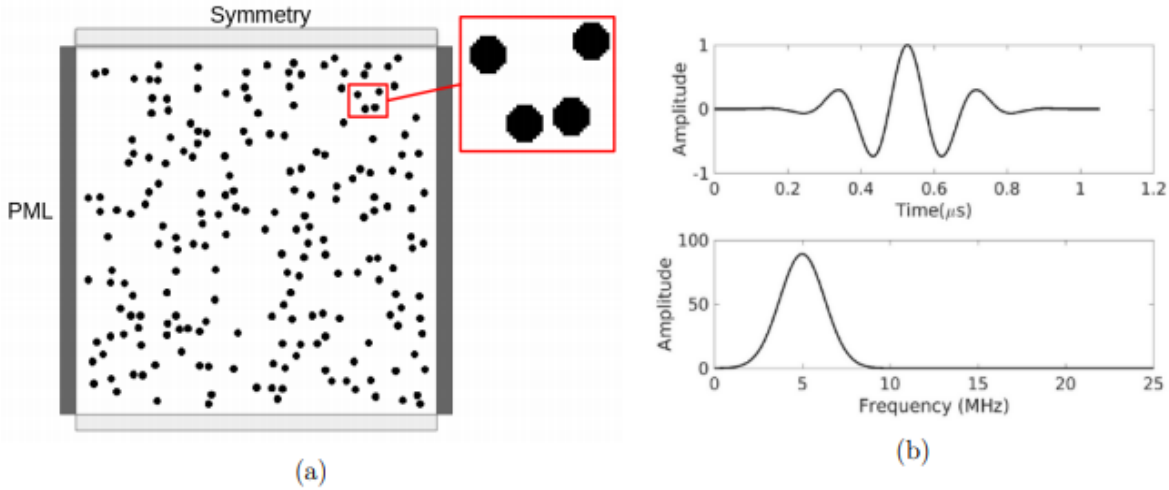

Figure 3-1 a) Structure schematic along with the boundary conditions. b) Emitted signal at 5 MHz.

3.2.2 Modeling attenuation

In this section we study two scattering models to investigate their applicability to ultrasonic attenuation in porous structures mimicking simplified cortical bone. These models are evaluated by the spectroscopy data acquired by numerical simulation.

First model: According to[161] without solving the wave equation and on the basis of scatterer size ϕ to the wavelength λ ratio and the functional dependence of scattering losses α_{scat} on frequency, following relationships can be often established:

$$\alpha_{scat} \sim \begin{cases} f^4.\phi^2, & Rayleigh\ domain\ k\phi \ll 1 \\ f^2.\phi, & Stochastic\ domain\ k\phi \approx 1 \\ \phi^{-1}, & Geometric\ domain\ k\phi > 1 \end{cases} \qquad \text{Equation 3-3}$$

Based on the chosen frequency and pore diameter range, and on the acoustical properties of bone defined in 3.2.1.1, different domains need to be selected to model the attenuation due to scattering. In order to determine which model depicts the structures mimicking cortical bone, we test different configurations presented in Equation 3-3.

Second Model: Previous works done by the authors[157] showed that the Independent Scattering Approximation (ISA) can be used to accurately predict the attenuation in simplified structures of cortical bone for $k\phi < 1$. Briefly, the ISA predicts the scattering attenuation as follows:

$$\alpha_{ISA} = \frac{\rho \sigma_{td}}{2} \qquad \text{Equation 3-4}$$

where σ_{td} is the total scattering cross section of one individual scatterer. The details of the ISA model and how to calculate the total scattering cross section are described in[157]. In this study, we use the ISA model combined with the relationship proposed in Equation 3-5 to model the total attenuation.

Attenuation due to scattering and absorption: Transmission of ultrasound waves in porous media is associated with scattering losses due to acoustic impedance difference between the matrix and pores. Aside from scattering, another major cause for attenuation is absorption by the solid matrix which contributes to the energy loss due to dissipation mechanisms within the medium[42]. Absorption by the pores was set to zero in the present simulations, and only the solid matrix is responsible for dissipation. In a study by Punurai[154] which characterized air voids inside a cement matrix using ultrasonic attenuation, it was shown that in any medium in

which attenuation due to scattering is significant, the total attenuation can be modeled as a linear combination of scattering and absorption as follows:

$$\alpha_{tot} = \alpha_{scat} + (1 - \nu)\alpha_{abs.nom} \qquad \text{Equation 3-5}$$

where ν is the porosity and $\alpha_{abs.nom}$ is the nominal absorption coefficient of the solid matrix. Although this relationship was used to model the air void scatterers, a previous study by the authors[157] showed that the Independent Scattering Approximation used in the Punurai study can also be used to model scattering in cortical bone. According to this relationship if we use the models to describe the attenuation due to scattering in a porous medium, and if we know the absorption coefficient of the matrix, the total attenuation can be estimated. As we will show in section 3.3 when scattering is combined with absorption in the matrix, both models fail to estimate total attenuation acquired from numerical simulations.

3.2.3 Isolating the effect of scattering and absorption

To isolate the effect of scattering and absorption, two different sets of simulations are run on each of the structures generated in section 3.2.1.1.

First: Simulations without absorption. In these simulations, the absorption coefficient in both the fluid and solid phases is set to zero and attenuation is exclusively attributable to scattering. Hence, the evaluated attenuation is the scattering attenuation coefficient α_{scat}.

Second: Simulations with consideration of absorption. In these simulations, both scattering by the pores and absorption by the solid matrix are responsible for the total

attenuation α_{tot}. In the solid phase, a nominal absorption coefficient of $\alpha_{nom} = 10 \frac{dB}{cm.MHz}$ [44] is used as the input for these simulations. Absorption in the pores remains set to zero, as absorption in marrow is much lower than absorption in the solid bone matrix.

Subtracting the scattering attenuation coefficient obtained in the first set of simulations from the total attenuation coefficient obtained in the second set of simulations, allows to assess the effective absorption in the medium. It is referred to as the *apparent absorption coefficient*, $\alpha_{app.abs}$ in this manuscript.

If Equation 3-5 held true, then one could conclude that $\alpha_{app.abs} = (1 - v)\alpha_{abs.nom}$. However, as we compare these two values in section 3.3 this equation does not hold true in all frequency ranges. Hence we will use a phenomenological model to describe the changes in apparent absorption as a function of frequency. Assuming that no absorption exists at zero frequency, we will use a power law model as follows:

$$\alpha_{app.abs}(f) = c.f^{\beta_{app}} \qquad \text{Equation 3-6}$$

where c is the model parameter and β_{app} is called the *apparent absorption exponent*. The goodness of fit is evaluated by measuring the R-square between data and fitted model. A *deviation factor* ϵ is also defined as:

$$\epsilon(f) = \frac{\left|\alpha_{app.abs} - \alpha_{nom}.f\right|}{\alpha_{nom}.f} \qquad \text{Equation 3-7}$$

$$= \left|1 - \left(\frac{c}{\alpha_{nom}}\right) f^{\beta_{app}-1}\right|$$

$\epsilon(f)$ is a dimensionless number which quantifies the divergence from the linear trend of absorption in a system containing random mono-disperse scatterers. In other words if $\epsilon(f)$ is 1, the assumption that the total attenuation is a linear combination of absorption and scattering holds true. On the contrary, as $\epsilon(f)$ starts to diverge from 1 the assumption would fail. Based on normalized frequency values, three scattering regimes are chosen as low ($k\phi$<0.8), medium (0.8<$k\phi$<1.0) and high scattering regimes ($k\phi$ >1.0). The deviation factor is evaluated for all frequency, pore density and diameter ranges. This is indicative of the conditions (frequency, diameter-density combination) under which the linear combination assumption starts to fail. The average value along with a 95% confidence interval is reported for each scattering regime.

3.2.4 Frequency Response: Investigating the linear behavior of the system

In the previous section, we defined β_{app} and $\epsilon(f)$ to evaluate when the linear combination assumption for scattering and absorption starts to fail. In this section we analyze this with a linear systems formalism.

Ultrasound propagation within a visco-elastic system including scatterers can be broken into two individual systems: I. a viscoelastic matrix with absorption coefficient α_{nom} II. a porous structure containing scatterers in a non-viscoelastic matrix. If we assumed that these two systems are linear time-invariant (LTI), one could conclude that:

$$\mathcal{F}_{tot}(\omega) = \mathcal{F}_{scat}(\omega).\mathcal{F}_{abs}(\omega) \qquad \text{Equation 3-8}$$

where $\mathcal{F}(\omega)$ represents the frequency response of the system and tot, $scat$ and abs indexes refer to total (viscoelastic matrix with presence of scatterers), scattering (non-viscoelastic matrix with presence of scatterers) and absorption (viscoelastic matrix without presence of scatterers) respectively. The schematic of these systems is illustrated in Figure 3-2.

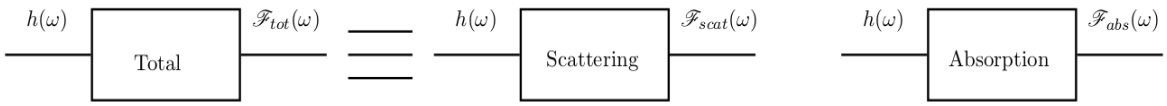

Figure 3-2 Frequency response of a system composed of scattering and absorption, to an impulse $h(\omega)$.

This suggests that in the frequency domain, the through-transmitted signal from an absorbing medium with absorption coefficient α_{nom} and scatterers is equal to the product of two signals: One is associated to the same medium with the exact same distribution of scatterers but no absorption; and the other is associated to an equivalent, purely absorbing medium with no scatterers.

Assuming an exponential decay over space of the amplitude of the frequency response, using Equation 3-1 and Equation 3-8 one can infer:

$$|\mathcal{F}_{tot}(\omega, x)| = e^{-\alpha_{tot}(\omega)x} = e^{-\alpha_{scat}(\omega)x}.e^{-\alpha_{abs}(\omega)x} \qquad \text{Equation 3-9}$$

$$= e^{-(\alpha_{scat}(\omega)+\alpha_{abs}(\omega))x}.$$

Hence:

if the system is LTI $\Longrightarrow \alpha_{tot}(\omega) = \alpha_{scat}(\omega) + \alpha_{abs}(\omega)$. Equation 3-10

The equation manifests that if a system can be assumed to be LTI, the total attenuation coefficient is the summation of nominal absorption coefficient and scattering coefficient. On the contrary, the failure to meet this criterion demonstrates a non-linear behavior of the system.

In order to determine the linearity of the system, three sets of simulation were conducted:

System a. Pure absorbing homogeneous bone with α_{nom}= 10 $\frac{dB}{cm.MHz}$

System b. Structure with non-viscoelastic matrix containing scatterers.

System c. The same structure with viscoelastic matrix and the same realization of scatterer distribution.

9 structures with combinations of $\phi \in \{40,80,120\}\mu m$ and $\rho \in \{5,10,15\} pore/mm^2$ are generated. An impulse described in 3.2.1.1 with central frequencies of 2, 5 and 8 MHz is transmitted through all the structures and the frequency responses of the systems i.e. $\mathcal{F}_a, \mathcal{F}_b$ and $\mathcal{F}_c$ are recorded. The normalized root mean square error (nRMSE) between $\mathcal{F}_c$ and $\mathcal{F}_a . \mathcal{F}_b$ is calculated, for the whole frequency, pore density and diameter ranges. The average value is reported for each scattering regime.

3.3 Results

3.3.1 Mono-disperse media

The spectroscopy data acquired by the numerical simulation from 3.2.1.1 are compared with the physics-based model discussed in 3.2.2. Figure 3-3 depicts these comparisons for ($\rho = 10\ pore/mm^2, \phi = 50\ \mu m$) and ($\rho = 5\ pore/mm^2, \phi = 70\ \mu m$). Since according to[157] the ISA models reliably predicts attenuation for low scattering regimes, we choose the cases in which $k\phi$ <0.8. Since the Rayleigh range was selected from Equation 3-3, we used a fourth order polynomial fit over the data acquired from 2D numerical simulation α_{tot}. As Figure 3-3 implies, both the ISA and Rayleigh model fail to predict the total attenuation due to scattering and absorption.

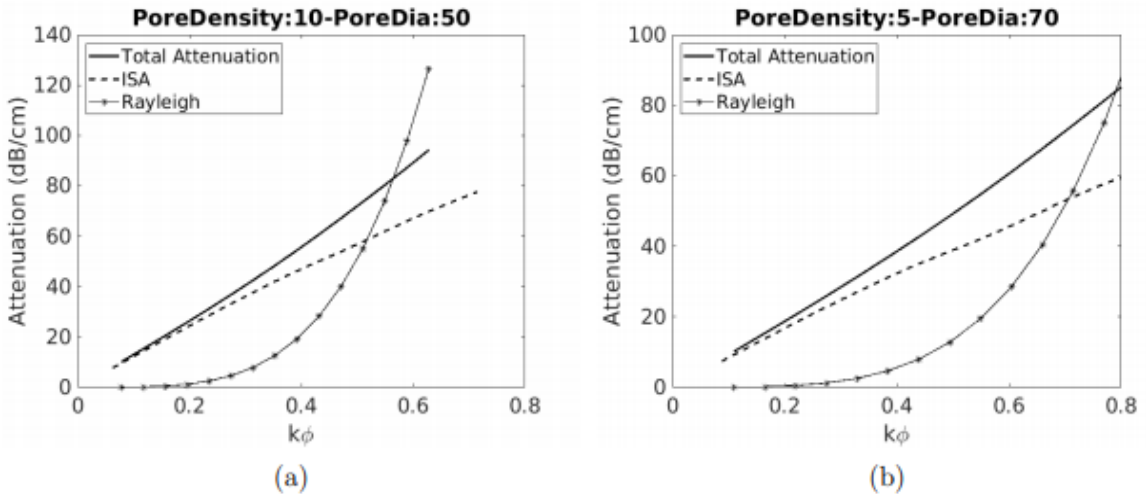

Figure 3-3 Comparison between α_{tot} estimated by numerical simulation and ISA - Rayleigh models.

The apparent absorption is calculated for all the diameter-density combinations mentioned in 3.2.1.1. Figure 3-4 illustrates the comparison between total attenuation α_{tot},

attenuation due to scattering α_{scat}, nominal α_{nom} and apparent absorption$\alpha_{app.abs}$. As the graph indicates, the apparent absorption changes linearly with respect to the normalized frequency and matches with the nominal absorption for lower values of $k\phi$. However as the normalized frequency increases, the apparent absorption diverges from the nominal value and starts to follow a non-linear trend.

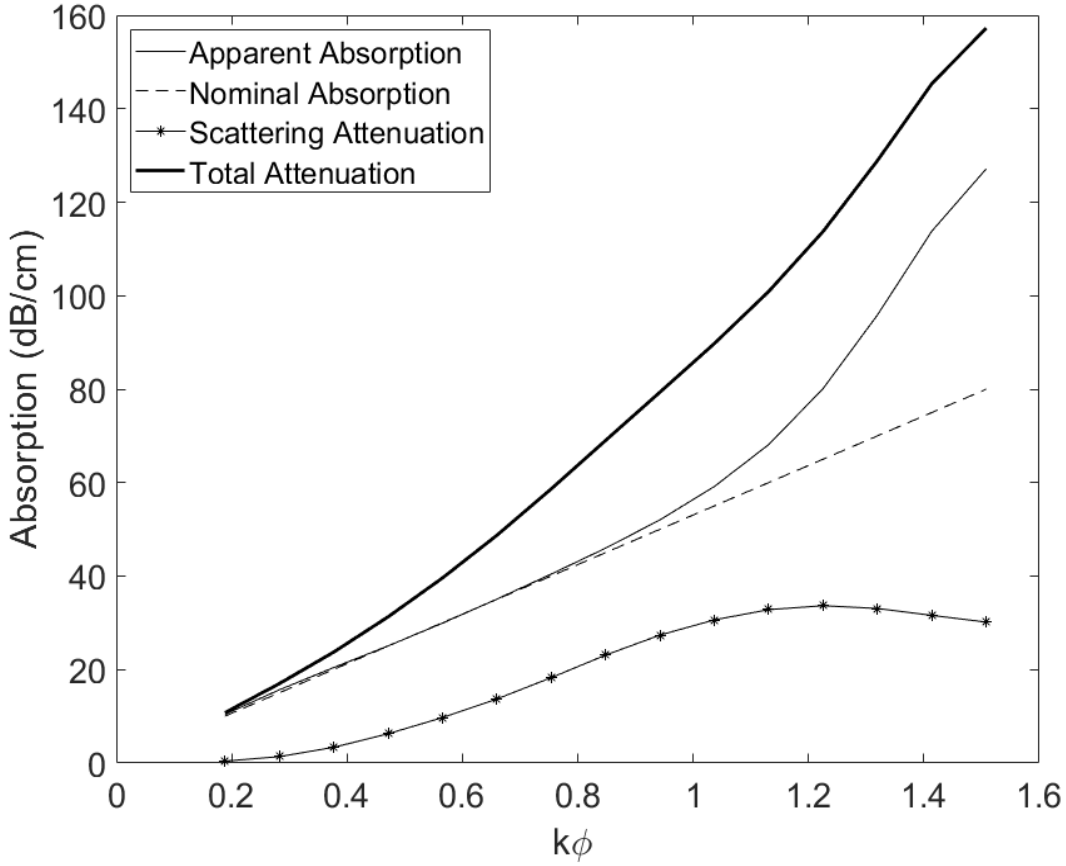

Figure 3-4 Attenuation due to scattering, absorption and apparent absorption as a function of normalized frequency ($k\phi$) for pore size = 120 μm; pore density = 5 $pore/mm^2$; - c/α_{nom}= 0.45; β_{app} = 1.58

Equation 3-6 is used to fit the apparent absorption data as a function of frequency. Figure 3-5 reveals the apparent absorption and the corresponding fit for 100μm pore diameter

and 16$pore/mm^2$ pore density. For all the structures, the R-square value changes from 1 to 0.97 indicating that the chosen power law fit can accurately predict the apparent absorption as a function of frequency.

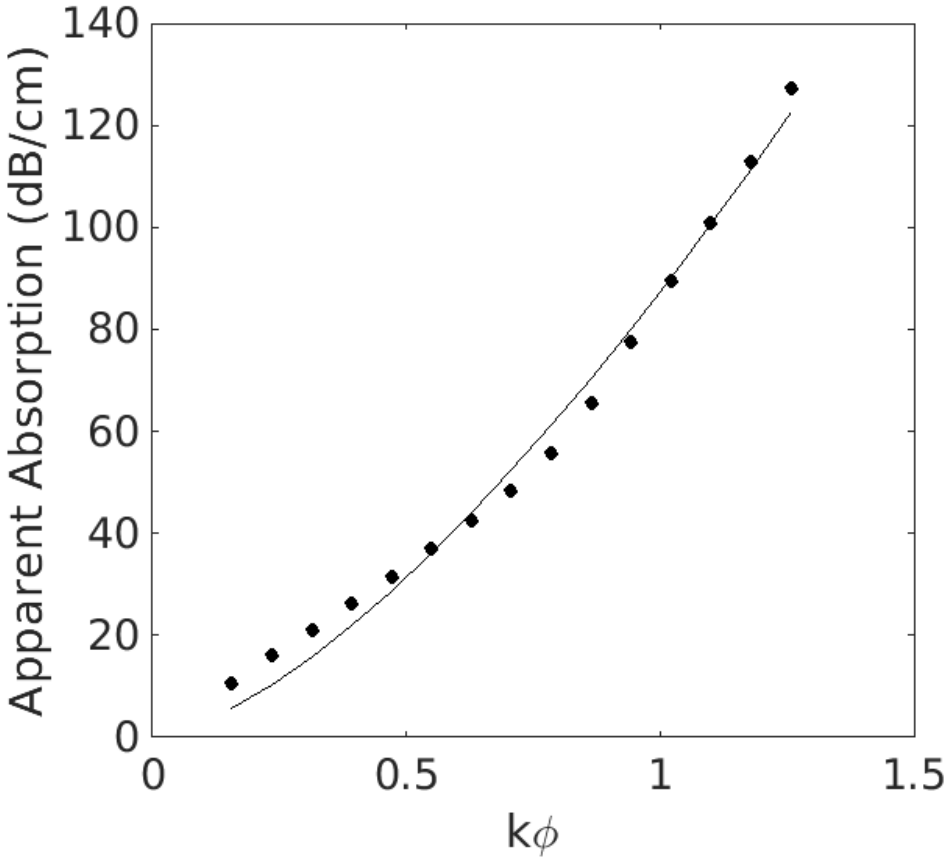

Figure 3-5 Apparent absorption fit using equation Equation 3-6 for Pore size: 100 μm; Pore Density: 16 $pore/mm^2$; R-square of the fit: 0.98

Figure 3-6 depicts the effect of pore density on linear divergence of apparent absorption as a function of normalized frequency. As the figure implies, an increase in pore density leads to increasing the parameter β_{app} in Equation 3-6 for higher values of $k\phi$.

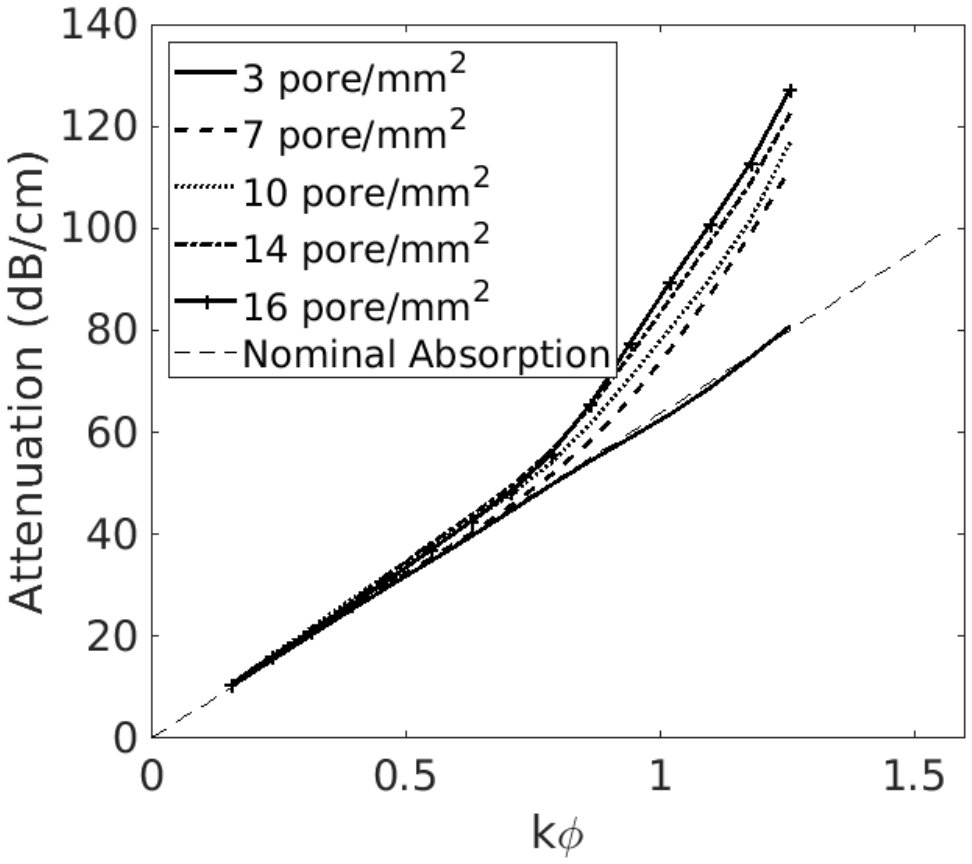

Figure 3-6 The effect of pore density change on apparent absorption as a function of normalized frequency.

Based on the apparent absorption data, for $k\phi$ < 0.8 we observe that β_{app}=1.0003 $\pm$ 0.0372 indicating that one can assume that for $k\phi$ < 0.8 the apparent absorption changes linearly with respect to frequency. However, for $k\phi$ > 0.8 we observe that β_{app}>1.

In order to investigate the reason for the non-linear behavior of apparent absorption, we compare the frequency responses in three different structures as described in 3.2.4. Figure 3-7 illustrates the frequency response of viscoelastic and non-viscoelastic systems for two different pore size-density combinations. In this figure, the reference curve represents the normalized impulse signal emitted through the system in the frequency domain. The

"Nonvisco. Bone w Scatterer" and "Visco. Bone w Scatterer" curves depict the frequency response of the signal propagated through non-viscoelastic ($\mathcal{F}_b$) and viscoelastic bone tissue ($\mathcal{F}_c$) with presence of scatterers, respectively. The "Visco. Bone w/o Scatterer" curve illustrates the frequency response of purely viscoelastic bone tissue associated with $\mathcal{F}_a$. The product of "Visco. Bone w/o Scatterer" and "Nonvisco. Bone w Scatterer" curves is shown by "visco*non-visco". A comparison between the "Visco. Bone w Scatterer" and "visco*non-visco" curves shows whether the system is linear i.e. if $\mathcal{F}_c = \mathcal{F}_a.\mathcal{F}_b$.

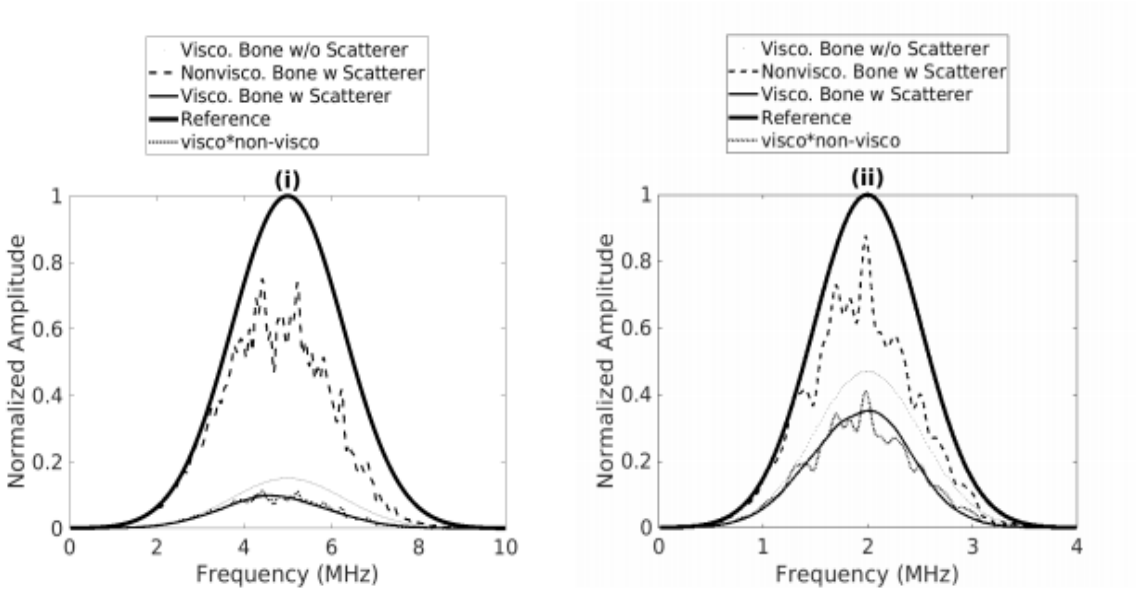

Figure 3-7 Frequency response of systems for structure (i): Pore diameter =80 μm and Pore density = 5 $\frac{pore}{mm^2}$to \$5 \ MHz\$ Gaussian impulse. nRMSE = 5.11% (kϕ=0.63) (ii): Pore diameter =120 μm and Pore density = 10 $\frac{pore}{mm^2}$ to 2 MHz Gaussian impulse. nRMSE = 6.07% (kϕ =0.38)

The deviation factor ϵ and nRMSE between $\mathcal{F}_c$ and $\mathcal{F}_a.\mathcal{F}_b$ in three scattering regimes are evaluated and illustrated in Figure 3-8 and Figure 3-9. As the figures depict, both ϵ and nRMSE increase above 10% as $k\phi$>0.8 matching the trend observed in Figure 3-6.

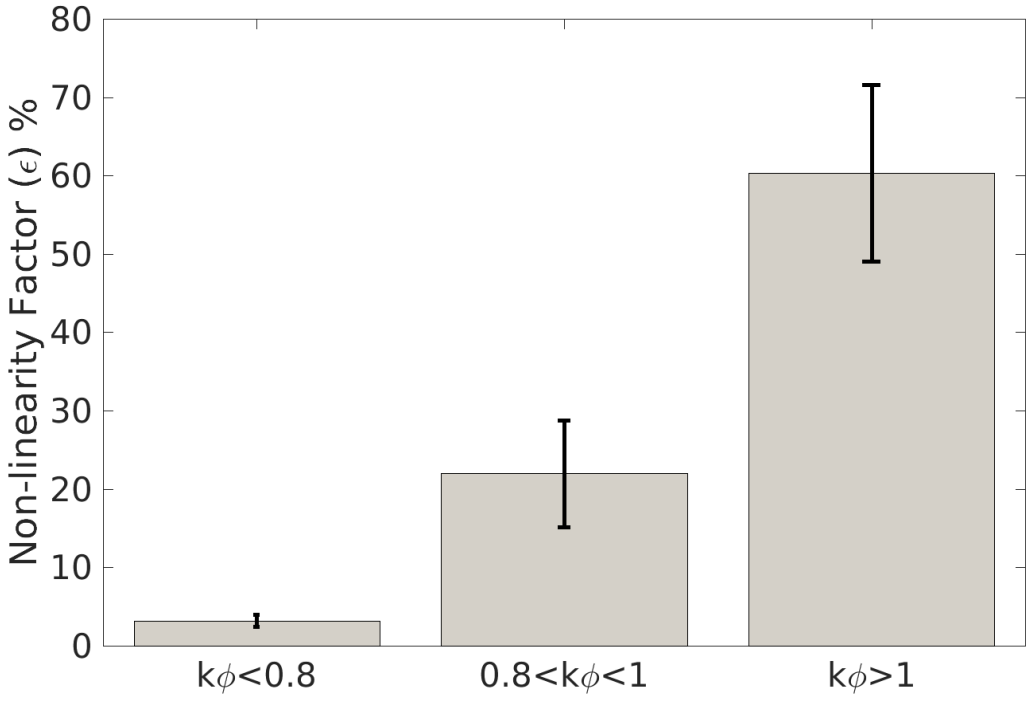

Figure 3-8 Deviation factor ϵ for low $k\phi$<0.8, medium 0.8< $k\phi$ <1.0 and high 1.0< $k\phi$ scattering regimes. Error bars are associated with the standard deviation of ϵ for all the combination of pore sizes/densities and frequency satisfying each $k\phi$ condition (40 combinations for each case).

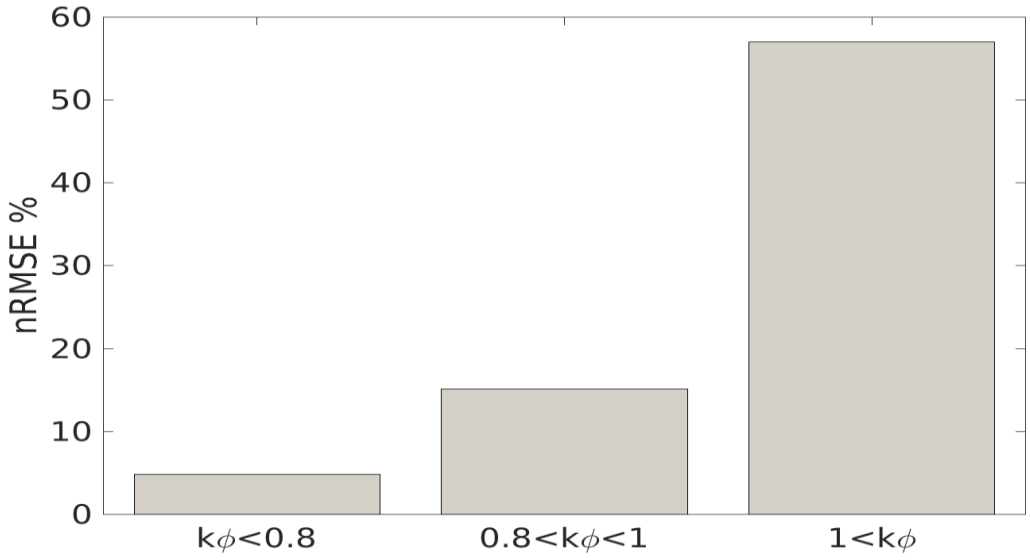

Figure 3-9 nRMSE percentage between $\mathcal{F}_c$ and $\mathcal{F}_a.\mathcal{F}_b$ for low $k\phi$ <0.8, medium 0.8< $k\phi$ <1.0 and high 1.0< $k\phi$ scattering regimes.

3.3.2 Polydisperse media

The apparent absorption coefficient is calculated using 2D simulations on CT images of two femur cortical bone samples with average pore diameter of 95.1μm and 96.3μm. The pore densities for the two samples are 12 $pore/mm^2$ and 10 $pore/mm^2$ respectively. The results indicating the similar deviation from the nominal absorption value as Figure 3-6 are depicted in Figure 3-10.

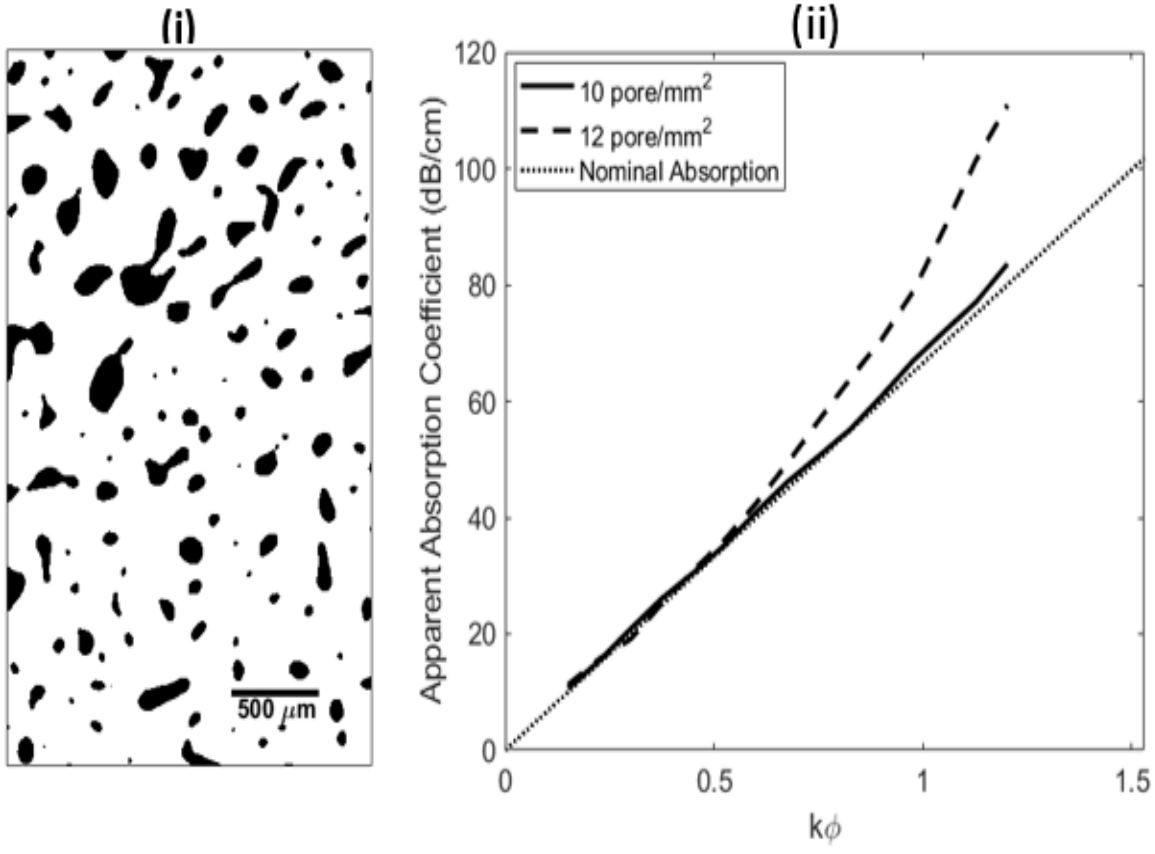

Figure 3-10 (i): Average pore diameter =95.1μm and pore density = 12 $pore/mm^2$ (ii): Apparent absorption coefficient vs. normalized frequency $k\phi$ for two polydisperse structures.

3.3.3 Exclusive effect of change in pore diameter and pore density

Figure 3-11.a illustrates the influence of pore density on the various components of attenuation at 8 MHz. It is obtained for $\phi = 60\mu m$ and ρ ranging from 5 $\frac{pore}{mm^2}$ to 25 $\frac{pore}{mm^2}$. The effect of pore density on attenuation for samples with larger pores ($\phi = 100\ \mu m$) is depicted in Figure 3-11.b. Figure 3-11.c and Figure 3-11.d exhibit α_{total}, $\alpha_{scat}$and $\alpha_{app.abs}$ for structures with varying pore diameters ranging from 40 to 120μm with constant pore densities of 10 $\frac{pore}{mm^2}$ and 20 $\frac{pore}{mm^2}$ respectively. All simulations are repeated for central frequency of 5MHz and the corresponding results are illustrated in Figure 3-12. The error-bars in figures are obtained from repeating simulations on three realizations of each random porous structure.

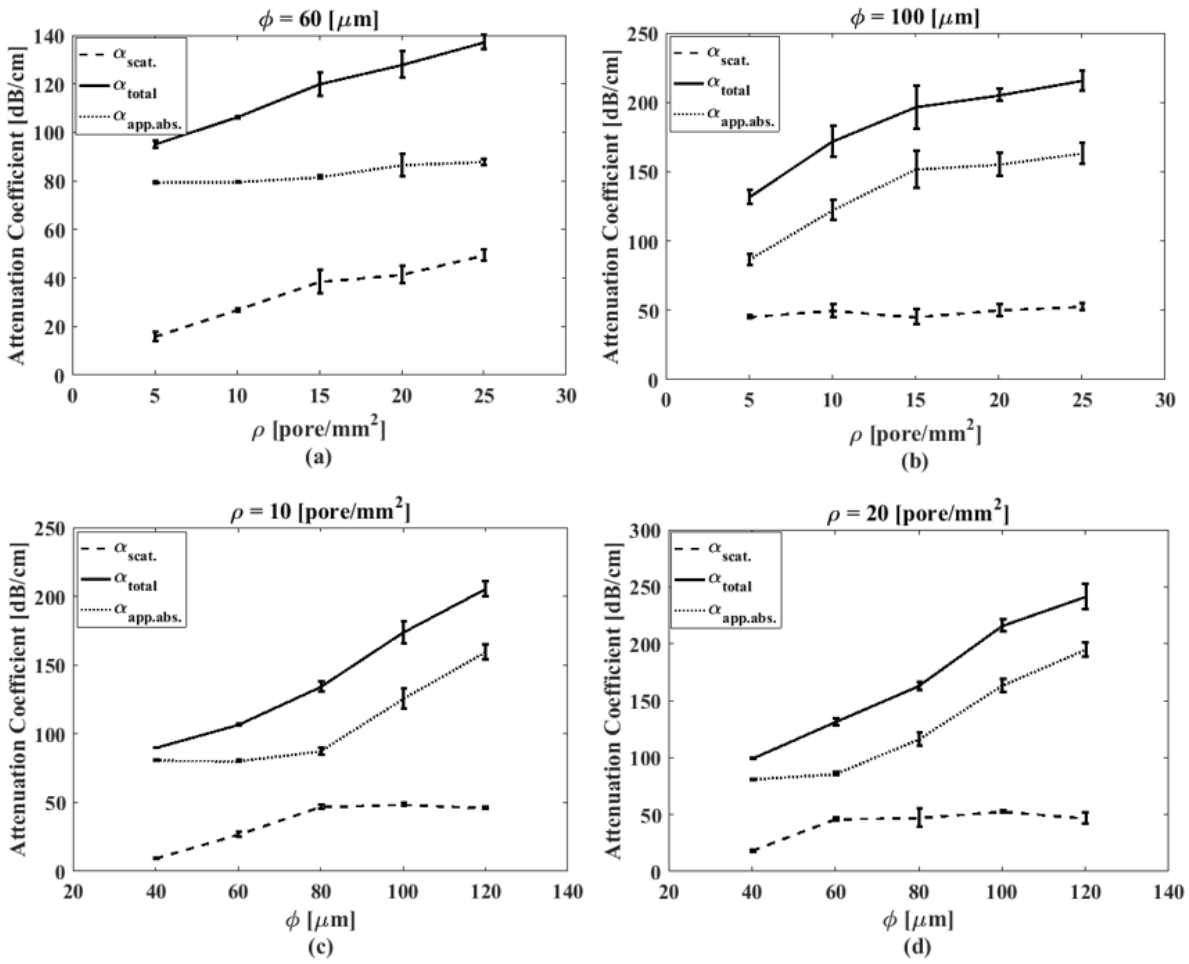

Figure 3-11 Attenuation coefficient α_{total}, scattering coefficient α_{scat} and apparent absorption coefficient $\alpha_{app.abs}$ for samples with a) constant $\phi = 60\ \mu m$ and varying ρ, b) constant $\phi = 100\ \mu m$ and varying ρ, c) constant ρ= $10\frac{pore}{mm^2}$ and varying ϕ and d) constant ρ= $20\frac{pore}{mm^2}$ and varying ϕ. (Number of realizations for each sample =3; Central Frequency = 8MHz)

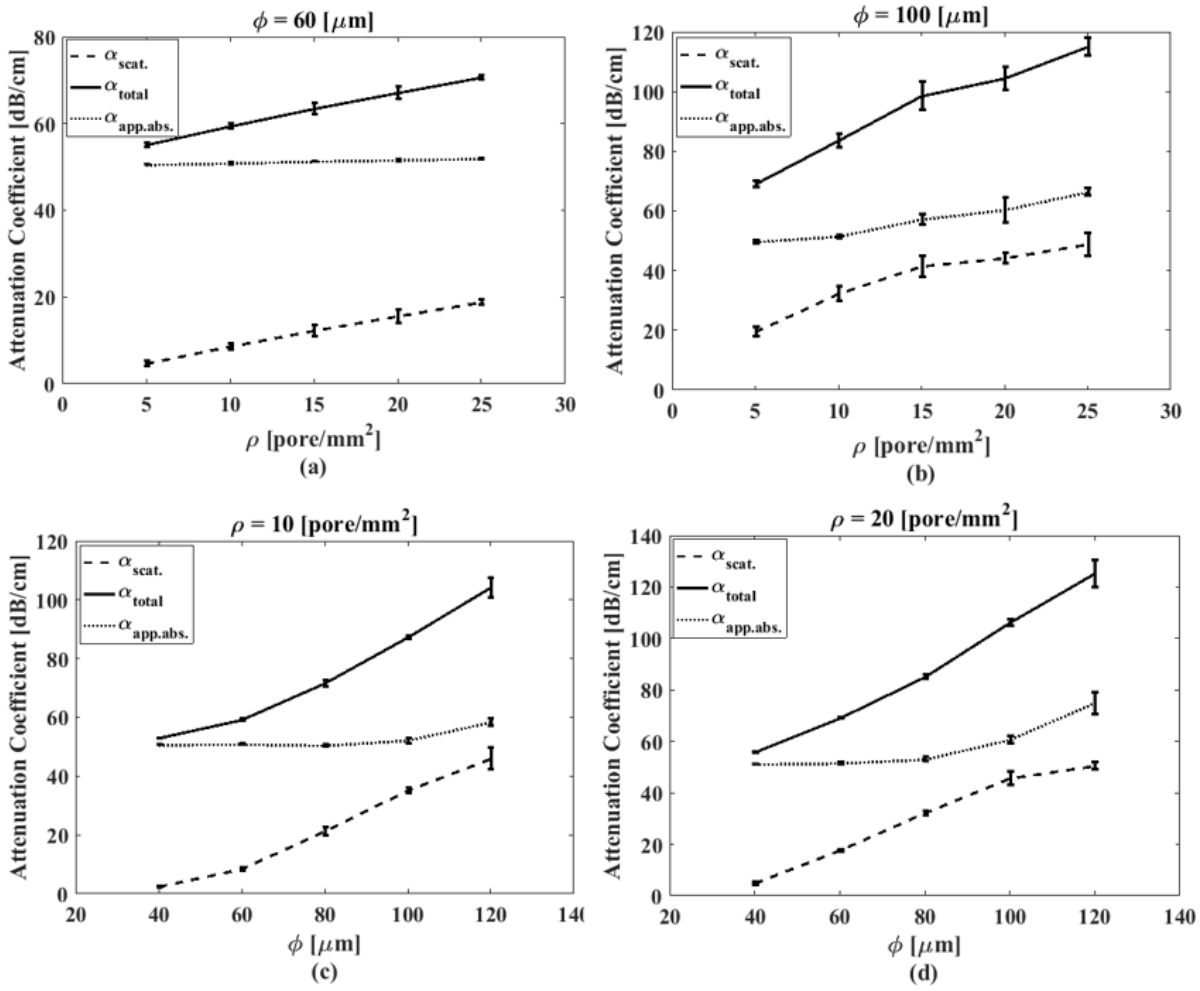

Figure 3-12 Attenuation coefficient α_total, scattering coefficient α_scat and apparent absorption coefficient α_(app.abs) for samples with a) constant ϕ=60 μm and varying ρ, b) constant ϕ=100 μm and varying ρ, c) constant ρ=10 pore/(mm^2) and varying ϕ and d) constant ρ=20 pore/(mm^2) and varying ϕ. (Number of realizations for each sample =3; Central Frequency = 5MHz)

Different behaviors are observed at 5 MHz and 8 MHz. At 5 MHz, the scattering attenuation seems to be more sensitive to changes in the micro-architecture than the absorption attenuation (Figure 3-12). At 8 MHz, the scattering attenuation is less sensitive to pore density than the absorption attenuation for larger pore diameters ($\phi = 100\ \mu m$), while the reverse can be observed for smaller pore diameters ($\phi = 60\ \mu m$).

The length of the signals received by each of the 30 receivers are calculated as instructed in section 3.2.1.1. Figure 3-13.a illustrates the signal received by receiver 30 normalized by its maximum for a sample with $\phi = 100\mu m$ and $\rho = 10\frac{pore}{mm^2}$. The beginning of the signal and end of the multiply scattered part (coda) are marked using a 0.0005 threshold. Figure 3-13.b depicts the length of the signals received by the 30 receivers (at 8 MHz) as wave travels within the porous structures with varying ϕ and constant $\rho = 10\frac{pore}{mm^2}$ (at $\phi = 80\ \mu m$, $k\phi = 1$). For pore diameters larger than $80\mu m$ the length of the coda is increasing significantly (147% increase in signal length from receiver 1 to 30 for $\phi = 120\mu m$), suggesting that the wave has taken longer paths within the medium. This can be linked to the observation of increase in apparent absorption coefficient in higher scattering regimes as wave is spending more time travelling in the highly absorbing bone matrix.

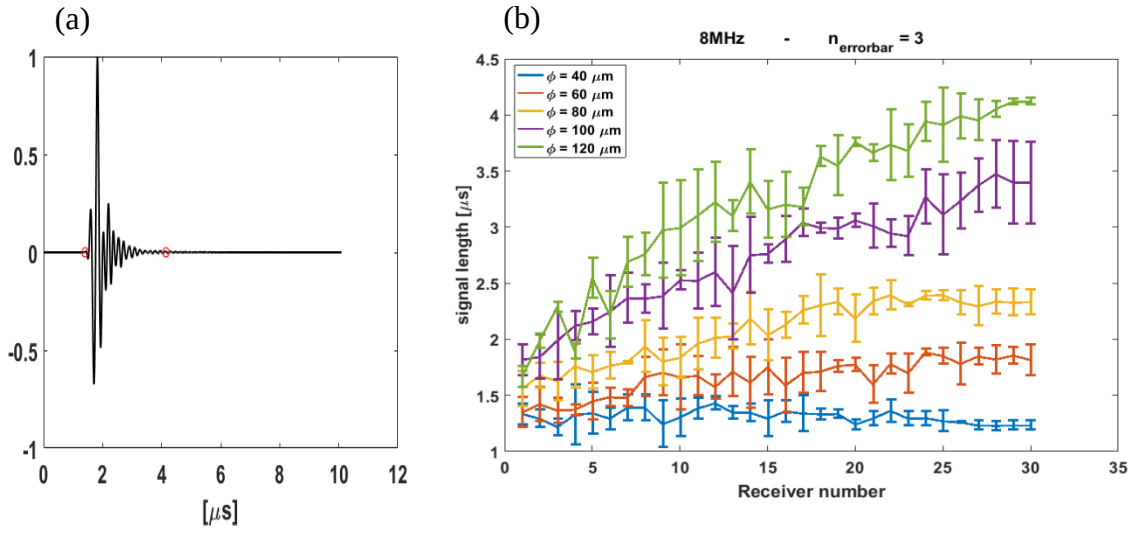

Figure 3-13 (a) Signal received by receiver 30 for a structure with $\phi = 100\mu m$ and $\rho = 10\frac{pore}{mm^2}$. (b) Length of the signals received by receivers 1 to 30, for structures with different pore diameters and constant $\rho = 10\frac{pore}{mm^2}$.

3.4 Discussion

The goal of this study was to address the individual effects of scattering and matrix viscoelasticity on the frequency-dependent ultrasonic attenuation in random mono-disperse structures mimicking simplified cortical bone. Numerical simulations were conducted on 2D structures for various pore diameter and pore density ranges (corresponding to ranges observed in cortical bone) with and without consideration of absorption in the solid matrix, in order to isolate the effect of absorption. Cortical bone is assumed to be transversely isotropic[162] validating the use of computationally cost-effective 2D simulations instead of 3D. First, we compared the attenuation data from numerical simulations to the predictions by two models: the Rayleigh and ISA models. These models have been successfully applied in random complex media where either the absorption in the matrix is not significant[163] or the effect of scattering is much higher than that of absorption such as in trabecular bone[155]. In this study we showed that although these two models are capable of estimating the attenuation due to scattering however when the scattering is combined with absorption of matrix both these models fail. This indicates that the assumption that total attenuation comes from the linear combination of scattering and absorption[154] does not hold true in the presence of multiple scattering. We introduce a parameter called *apparent absorption* quantifying the difference between total attenuation and attenuation exclusively due to scattering. Figure 3-4 illustrates an increase in α_{tot}, α_{scat} and $\alpha_{app.abs}$ as a result of an increase in the normalized frequency when $k\phi$< 0.8. But after a certain point ($k\phi$ =1), with an increase in $k\phi$, α_{scat} seemed to reach its maximum value while α_{tot} keeps increasing as a result of an increase in absorption. This suggests that while losses due to scattering do not exceed a plateau value, there will still be increase in attenuation due to absorption. The fact that, due to multiple scattering, the wave

might have traveled longer paths in the absorbing solid matrix can explain this observation[153,164]. While the scatterer size relative to the wavelength affects the propagation and attenuation of the wave, a previous study by the authors[157] have illustrated the importance of normalized frequency $k\phi$ for attenuation assessment as opposed to exclusive consideration of the pore size. This is why in the present study apparent absorption coefficient is investigated as a function of $k\phi$. It is shown that the frequency-dependent apparent absorption can be predicted by a phenomenological model as $\alpha_{app.abs}(f) = c.f^{\beta_{app}}$, where the model parameters depend upon pore diameter and density. For low scattering regimes ($k\phi$ < 0.8), one can show that the apparent absorption behaves linearly i.e. $\beta_{app} \approx 1$ resulting in $\alpha_{tot} = \alpha_{nom} + \alpha_{scat}$. However for higher scattering regimes ($k\phi$ > 0.8), the apparent absorption starts to follow a non-linear trend where $\beta_{app} > 1$, leading to $\alpha_{tot} = \alpha_{app.abs} + \alpha_{scat}$, and $\alpha_{app.abs} \neq \alpha_{nom}$. To quantify the divergence from a linear trend of absorption in a system containing random mono-disperse scatterers, a deviation factor was calculated for all the structures. This parameter was averaged over different pore densities and it was shown that it significantly increases as the scattering regime changes from low to high.

The structures were also analyzed by breaking them into two LTI systems and comparing the frequency-responses of the systems. The nRMSE of the product of frequency responses was measured and averaged over different pore densities and According to Figure 3-9 it was shown that it significantly increases as the scattering regime changes from low to high, showing the same trend as deviation factor. This indicates that for low scattering regimes ($k\phi$ <0.8), a viscoelastic system with mono-disperse random pore distribution can be considered as an LTI system where the frequency response of the whole system ($\mathcal{F}_c$) is approximated by

the multiplication of two equivalent scattering ($\mathcal{F}_b$) and absorbing systems ($\mathcal{F}_a$). As the scattering regime changes to high, the linearity assumption of the system fails.

The model proposed in this study was based on 2D numerical simulations mimicking the wave propagation within simplified models of cortical bone. Unlike an experimental study, the simulation tool enabled the independent control over the micro-structural parameters such as pore diameter and pore density, which was needed to establish the parametric model. This justifies the choice of simplified microstructures over real cortical microstructures, but also has obvious limitations in how accurately it represents bone.

While this study was focused on mono-disperse structures, the results from two poly-disperse bone samples (Figure 3-10) indicate that $\alpha_{app.abs}$ follows the same trend as the normalized frequency $k\phi$ increases (Figure 3-6). Our results suggest that in poly-disperse structures, the deviation from nominal absorption coefficient happens at relatively higher densities. The fact that the median pore diameter of the sample with ρ= 12 $pore/mm^2$ is 72.3μm indicates that majority of the pores have diameters below the average pore diameter of 95.1μm and that effectively contributes to propagation and attenuation in the medium. More work on the effect of diameter distribution in poly-disperse media and its influence on wave attenuation needs to be done in the future to complement the present study.

Although the main focus of this study was cortical bone, the results can be applied to any random complex medium in which the following assumptions can be made. 1- Absorption in the matrix plays a significant role in attenuation. 2- The absorption coefficient in the scatterers is negligible compared to matrix's. 3- Highly scattering regime is the main scattering mechanism. Although the scattering cross section is different in 3D, leading to different

attenuation values, the results and overall trends observed in this study are expected to apply to 3D structures as well. This is especially true in cortical bone, which is transverse isotropic, and where the pores have a cylindrical shape.

In addition to investigating the frequency-dependent attenuation in cortical bone, we isolated the effect of an increase in pore size and pore density independently on the attenuation coefficient as well as on its scattering and absorption components. The dependence of α_{total}, α_{scat} and $\alpha_{app.abs}$ on micro-structural changes of bone mimicking structures is well depicted in Figure 3-11 and Figure 3-12. An increase in pore size and pore density has in all cases resulted in an increase in total attenuation. In all of the structures, $\alpha_{app.abs}$ which contributes to absorption losses was larger than α_{scat}. This suggested that while both absorption and scattering contribute to the total attenuation, absorption is likely to be dominant in cortical bone. This is in agreement with previous research[43]. As explained earlier, to run the simulations with consideration of absorption there needs to be an input value for absorption coefficient. It was anticipated that $\alpha_{app.abs}$ would be equal to the nominal input value for the absorption coefficient. When operating at 5MHz (Figure 3-12), $\alpha_{app.abs}$ did not diverge much from the nominal value (50dB/cm). However, in Figure 3-12.c and Figure 3-12.d for $\phi \geq 100\,\mu m$ an increase in $\alpha_{app.abs}$ was observed. At 8MHz, $\alpha_{app.abs}$ was equal the nominal input value (80dB/cm) for smaller pore diameters ($\phi < 80\,\mu m$ at $10\frac{pore}{mm^2}$ and $\phi < 60\,\mu m$ at $20\,\frac{pore}{mm^2}$; Figure 3-11.c,d), and increased beyond these values. Figure 3-11.a and Figure 3-12.a suggested that the change in pore density does not affect $\alpha_{app.abs}$ in a moderately scattering regime. $k\phi \geq 1$ is associated with highly scattering regime and the threshold for pore size to attain that limit is 79 μm and 127 μm for 8MHz and 5MHz respectively. This explains the fact that

$\alpha_{app.abs}$ was increasing with increase in ρ in Figure 3-11.b while the change in pore density was not affecting $\alpha_{app.abs}$ in Figure 3-11.a when the diameter is below $79\mu m$. Similarly, Figure 3-12.a and Figure 3-12.b illustrated that for a relatively smaller constant pore size (ϕ = $60\mu m$) and varying ρ, $\alpha_{app.abs}$ remained constant with changes in ρ, while it was not the case if the constant pore size increased to 100 μm. Figure 3-11.b, Figure 3-11.c and Figure 3-11.d suggested a limit to the amount of scattering attenuation, since α_{scat} was not exceeding the value 50dB/cm. When $k\phi$ became greater than one (ie for pore diameter greater than $80\mu m$ at 8 MHz), geometric scattering did not participate in the spatial spread of the energy, and the scattering attenuation stoped increasing with increase in pore diameter. An increase in ϕ (Figure 3-11.c, Figure 3-11.d) and ρ (Figure 3-11.b) was expected to cause a decreasing trend in the apparent absorption since the fraction of absorbing material (bone tissue) was decreasing. However the opposite was observed, and α_{total} was increasing as a result of increase in absorption. To explain this, we hypothesize that in a highly scattering regime ($k\phi \geq 1$), the total path length in the absorbing solid phase increases with an increase in ϕ and ρ due to multiple scattering. To examine this hypothesis we compare the signal length as wave travels within the medium (Figure 3-13.b). In Figure 3-13.b while for a low/intermediate scattering regime ($\phi < 80\mu m$ at 8 MHz), the signal length received on receivers 1 to 30 does not change much, for structures with larger pore diameter, the length of the signal seems to be increasing considerably as wave travels into the medium. For instance a 147% increase in the signal length is observed for $\phi = 120\ \mu m$ while this increase is only 49% for $\phi = 80\ \mu m$.

A grid step of $10\mu m$ was chosen to meet the 20 points per wavelength limit for simulations while keeping the computational costs low. However, this might have led to an inaccurate scattering response from the smaller pores. Another limitation of this study is that

the mode conversion effects on attenuation resulting from the friction between the solid and fluid phase, as well as intrinsic anisotropy of bone tissue have not been taken into account. The purpose of the present study was less to develop a new model of attenuation in porous media, and more to shed light on the fact that, when the surrounding matrix is absorbing in a highly heterogeneous medium, the interaction between scattering and absorption is complex and nonlinear.

3.5 Conclusion

The mechanisms regulating the influence of the micro-architecture of porous structures on ultrasound attenuation are complex. This article attempts to provide insights on the relative contribution of scattering and absorption to attenuation, and their dependence on the microstructure. This study investigates the dependence of attenuation and its constituents, scattering and absorption on the normalized frequency $k\phi$, Ct.Po.Dm. and Ct.Po.Dn. for porous structures mimicking cortical bone. The losses due to absorption in porous structures were quantified by a parameter called apparent absorption coefficient ($\alpha_{app.abs}$).

In a highly scattering regime, an increase in pore size and pore density results in an increase in the total attenuation while the scattering attenuation remains constant. This suggests that, for larger pore sizes, the apparent absorption increases despite of the fact that there is less absorbing material within the porous structure. This could be attributed to longer paths taken by the wave in a highly scattering medium due to the presence of multiple scattering. On the contrary, in the low/intermediate scattering regimes, the changes in scattering attenuation due to an increase in pore size and pore density are responsible for changes in the total attenuation, while the absorption attenuation remains constant and equal to its nominal input value, ie not influenced by changes in porosity.

In higher scattering regimes, an increase in $k\phi$ does not affect the scattering attenuation coefficient, but the total attenuation still increases indicating an increase in absorption losses. Instead of common models combining scattering and absorption linearly to obtain the total attenuation, we showed that the following parametric relationship can be used:

$$\alpha_{tot} = \alpha_{scat} + cf^{\beta_{app}}$$ Equation 3-11

The dependence of $\alpha_{app.abs}$ upon the normalized frequency could be exploited to solve inverse problems in order to obtain structural parameters such as pore diameter and pore density from attenuation measurements in bone.

Chapter 4: Characterization of biological tissues using backscatter statistics

Ultrasound backscattered signals encompass information based on the micro-structure of heterogeneous media. Shannon entropy has been used to evaluate these micro-structural changes in biological tissues in the past. Here we evaluate polydimethylsiloxane (PDMS) samples with different scatterer concentrations, lung mimicking phantoms, and cortical bone structures with varying average pore diameter (Ct.Po.Dm.), density (Ct.Po.Dn.) and porosity (Ct.Po.). The objective is to exploit entropy which is an indication of randomness in the signals to characterize cortical bone for osteoporosis evaluation, as well as assessment of porous phantoms mimicking healthy and edematous lung.

4.1 Introduction to entropy and its applications to tissue characterization

Multiple scattering of ultrasound waves is associated with loss of energy and a diffusive regime which have previously been used to characterize heterogeneous media such as cortical bone through measurements of the attenuation coefficient[44,153,164,165], and the diffusion constant[166]. In addition, multiple scattering affects the statistics of the signal amplitude. Several studies have investigated the potential of statistical models to characterize scattering media. Based on its simplicity and convenience, the Nakagami distribution[167] has been used to characterize liver, breast masses and tissue mimicking phantoms[168–173]. Another method in statistical analysis of ultrasound signals is based on the Shannon entropy which quantifies the uncertainties in the system[174]. The definition of Shannon entropy in information theory encompasses the probabilistic features of ensembles of messages, as the definition of entropy

would apply to statistical ensembles of micro-states in statistical mechanics[175]. In a QUS imaging study, Tsui et al. have demonstrated that the concentration of scatterers in phantoms affects the Shannon entropy[176]. Similar entropy imaging techniques have been implemented to evaluate fatty liver disease, cataract lens and breast tumors[177–181].

4.1.1 Cortical bone

Quantitative ultrasound (QUS), as a safer modality has been used to evaluate trabecular bone through measurements of speed of sound (SOS) and broadband ultrasound attenuation (BUA) in accessible sites such as the calcaneus[34,56,182]. In spite of the fact that cortical bone has high load-bearing capacities of cortical bone and strong correlations between its micro-structural and mechanical parameters[101,104,106,143,144], it has not been studied as extensively as trabecular bone[183]. Cortical bone is a transversely isotropic structure in which cylindrical shaped units (osteons) are embedded in the bone tissue. Ultrasound wave propagation in cortical bone is affected by its structure due to acoustical impedance difference between the osteons and bone tissue. Entropy as a measure to quantify the disorder in the medium is used in the present study to characterize heterogeneous structures through experiments on polydimethylsiloxane (PDMS) (Dow Corning Sylgard 184) samples with varying concentrations of Barium Tantanate (BaTiO3), and simulations on cortical bone structures obtained from CT images. Entropy measurement of PDMS-BaTiO3 samples is done as a proof of concept to assess its applicability in characterizing scattering media with different microstructures. Implementing the same approach to characterize cortical bone structures with respect to parameters like porosity, pore diameter and density, makes entropy a potentially effective tool for clinical evaluation of cortical bone in the future.

4.1.2 Pulmonary edema

Pulmonary edema is associated with elevated levels of fluid in lungs and occurs as a result of respiratory distress and increased pulmonary micro-vascular permeability[184]. In severe cases, the accumulation of fluid happens beyond local fluid-binding sites and fluid overflows into interstitial spaces, perivascular spaces and even the alveoli[185]. While X-ray and computed tomography (CT) imaging are common modalities to assess the damage to the respiratory system, they are associated with certain limitations such as lack of portability and risk of ionizing radiation in case of regular monitoring[186–189]. Ultrasound is a great alternative modality considering its safety, portability and lower cost compared to CT. Several studies have exploited ultrasound to assess lungs through imaging techniques based on the detection of certain artifacts like b-lines and a-lines[188,190–193]. Conventional lung ultrasound methods are mostly qualitative and associated with limitations such as user subjectivity and frequency-dependence[192]. While alveoli in lungs act as scatterers and make echo-location-based conventional ultrasound imaging elusive, quantitative ultrasound techniques can alternatively be applied to characterize lung. Efforts through measurement of the diffusion constant have been made in the past to evaluate lung[194]. In the present study we introduce a quantitative ultrasound (QUS) approach based on measurement of Shannon entropy to characterize a lung mimicking phantom with varying air VF.

4.2 Methodology

4.2.1 PDMS phantom preparation and ultrasound data acquisition

To make the ceramic-silicon composite samples, the two parts of PDMS are measured such that the weight ratio of the base to the curing agent is 25 to 1. They are mixed in a plastic beaker and BaTiO3 powder is added to the mixture with ratio of 4:1, 2:1, 4:3, 1:1 and 1:2 corresponding to 4, 7, 11, 14 and 24 volume fraction (VF) percentages, respectively. The BaTiO3 act as scatterers due to acoustical impedance with the surrounding matrix. The resulted ceramic-silicone mixture is stirred consistently, degassed in a vacuum chamber, cured at 100 °C for 2 hours and cut into approximately 12 mm thick cylinders with 100 mm diameter. A total of 5 PDMS phantoms are used in this study.

A 128 element L7-4 array transducer is used to acquire full synthetic aperture data at a central frequency of 5 MHz, from a Verasonics Vantange (Verasonics Inc. Kirkland, WA, USA) 128 system. The data for each phantom is acquired three times, at slightly different locations to account for the deviation between the results. The beam-formed radio-frequency (Rf) signals (focus ~ 6mm from the surface of the sample) are also acquired to obtain the entropy maps of the PDMS phantoms.

4.2.2 Acquisition of the CT images of cortical bone samples used in the numerical simulation study

43 human femur bone specimens are obtained and cut to small cubic samples with nominal size of 3× 4×5 mm^3. For each specimen a synchroton radiation micro-computed tomography (SRμCT) three dimensional scan and a full set of two-dimensional radiographic cross-sectional images (pixel size: 6.5 μm) are acquired and binarized as discussed in[159]. The

image processing procedure to obtain structural parameters Ct.Po., Ct.Po.Dm. and Ct.Po.Dn. is detailed in a previous study[158].

4.2.3 In-vivo measurement of micro-structural parameters at the distal third of the tibia

49 female patients aging from 56 to 86 (mean age: 69±7 y) took part in the present study which was approved by the German Radiation Protection Ordinance (z5-22464/2019-090-G). Starting at approximately 20 mm from the tibial endplate (ultradistal tibia), high-resolution peripheral quantitative computed tomography scans with a nominal isotropic resolution of 60μm were performed using a clinical HR-pQCT scanner (XtremeCT II, Scanco Medical AG, Brüttisellen, Switzerland). The volumetric bone mineral density (vBMD) was obtained as described in[129]. The cortical bone was segmented following a procedure detailed by Burghardt et al[130]. Using the manufacturer's scripts, cortical porosity, pore diameter and pore density were obtained.

4.2.4 Finite-difference time-domain (FDTD) simulations on cortical bone structures

SimSonic[131] which is an open source software is used to model ultrasound wave propagation in bone structures. FDTD simulations are carried out on 7 cross-sectional images for each cortical bone specimen, resulting in 301 total simulations. Bone and water material properties[131] are assigned to solid and liquid phases of binarized images, respectively. According to previous studies on cortical bone[44], the total attenuation which incorporates both scattering and absorption losses is observed to be approximately 10 dB/cm/MHz. To the best of our knowledge, absorption coefficient of pure bone has not been reported. Hence, in our simulations, the absorption coefficient for the bone matrix is arbitrarily set at 3 dB/cm/MHz

which is below 10 dB/cm/MHz (total attenuation). As illustrated in Figure 4-1, for each acquisition, a plane wave at 5 MHz is transmitted in the medium and the backscattered signals are received on the transducer array. The speed of sound in bone matrix is assumed to be 4 $\frac{mm}{\mu s}$. The spacing between the elements is kept at 0.3 mm which meets the half-wavelength requirement and is extensively used in the fabrication of ultrasonic transducers[195]. Considering the small size of the structures (2.11× 3.18mm^2), the number of the elements is limited to 11. Perfectly matched layer (PML) boundary conditions are used to minimize the reflections from the edges of the sample. The gridstep for the simulations is set to 0.0065 mm, which meets the 20 points per wavelength simulation requirement[134]. The length of the acquisition is 3.2 μs which is longer than the corresponding time required for the wave to travel the whole structure back and forth. This allows us to extract longer backscattered signals, in order to take multiple scattering of the waves into account.

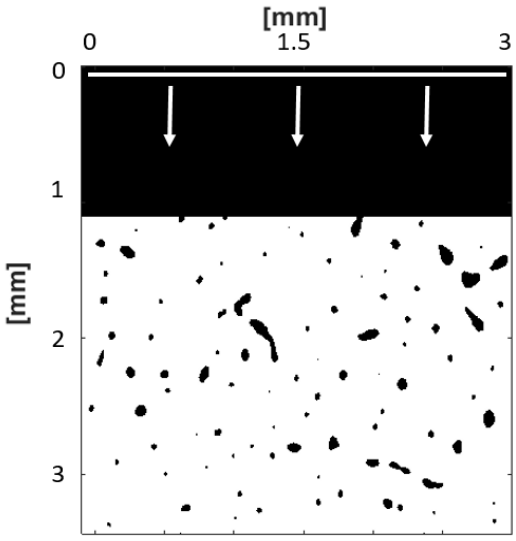

Figure 4-1 A plane wave is transmitted at 5MHz and the backscattered signals are received on the array transducer (located on the top)

4.2.5 Shannon entropy

To obtain the entropy map for each, a sliding window method is used to process the backscattered Rf signals locally.

The probability density function (PDF) of the amplitudes of the signals in each time window is obtained and Shannon entropy is calculated as follows[174]:

$$H_c = -\sum_{y_{min}}^{y_{max}} w(y)\log_2[w(y)]dy, \qquad \text{Equation 4-1}$$

where H_c is the entropy, w(y) is the amplitude distribution, y_{min} and y_{max} are the minimal and maximal values of the backscattered envelope $y = f(t)$. By assigning the calculated entropy value to each window, the entropy map is formed.

4.2.6 Entropy map for PDMS samples

The size of the window for PDMS samples is $0.6 \times 0.6\ mm^2$, with 50% overlap in both lateral and axial directions. The bin width of the histogram to get the PDF of the signals is set at 500.

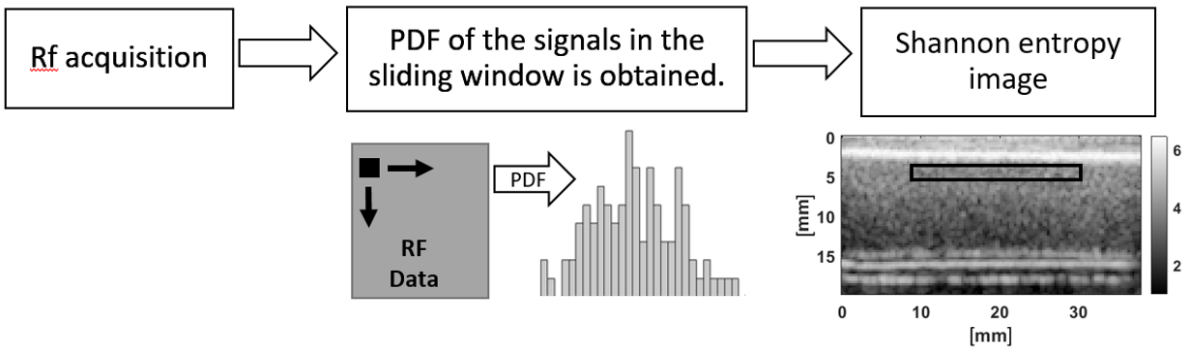

Figure 4-2 Algorithmic scheme to obtain the entropy image using PDF of the signals in the sliding window. The frame on the entropy image of a PDMS sample (scatterer VF = 4%) shows the region of interest.

Figure 4-2 demonstrates the process of acquiring the entropy image of a PDMS sample with 4% scatterer VF. For each sample the entropy is averaged over a 2.4×21.3 mm^2 region of interest.

4.2.7 Entropy map for cortical bone structures (numerical simulation study)

Considering the small size of the bone structures, the lateral resolution for bone entropy maps is limited to 11, 0.3mm elements. For each element, the received signals are normalized with respect to their maximum and truncated into 0.21μs half-overlapping time-windows for which the entropy is calculated and assigned to obtain the entropy map (Figure 4-6.a). The bin width of the histogram to acquire the PDF of the signals is set at 0.004.

4.2.8 In-vivo ultrasound data acquisition and obtaining the entropy map at the distal third of the tibia

A linear array transducer (4DL14-5/38, Ultrasonicx, Richmond, Canada) was located against the tibia bone of patients transversely. The backscattered is acquired using the Ultrasonix Touch (BK Ultrasound) scanner. The signals are focused in receive and the focus is adjusted approximately on the surface of the bone, and central and sampling frequencies are 7.8 MHz and 40 MHz respectively. Using the Hilbert transform, the envelope of the signals is obtained. The acquisition of the entropy map from the envelope image follows the process indicated in Figure 4-2. The lateral length of the window is 0.6 mm (equivalent to two elements) with 50% overlap and it is $0.51\mu s$ long in the direction of wave propagation. Bone is a highly scattering medium, the relationship between time and distance is not necessarily linear; this is why we are not converting time-windows to spatial windows. The windows have 85% overlap which provides a better resolution, in spite of the increased computational costs. The bin width of the histogram to obtain the PDF of the signals is 200. To reduce the computational costs, the entropy map is only obtained for an ROI on the image. The signals attributing to the ROI are $2\mu s$ long and start from the bone surface (Figure 4-3).

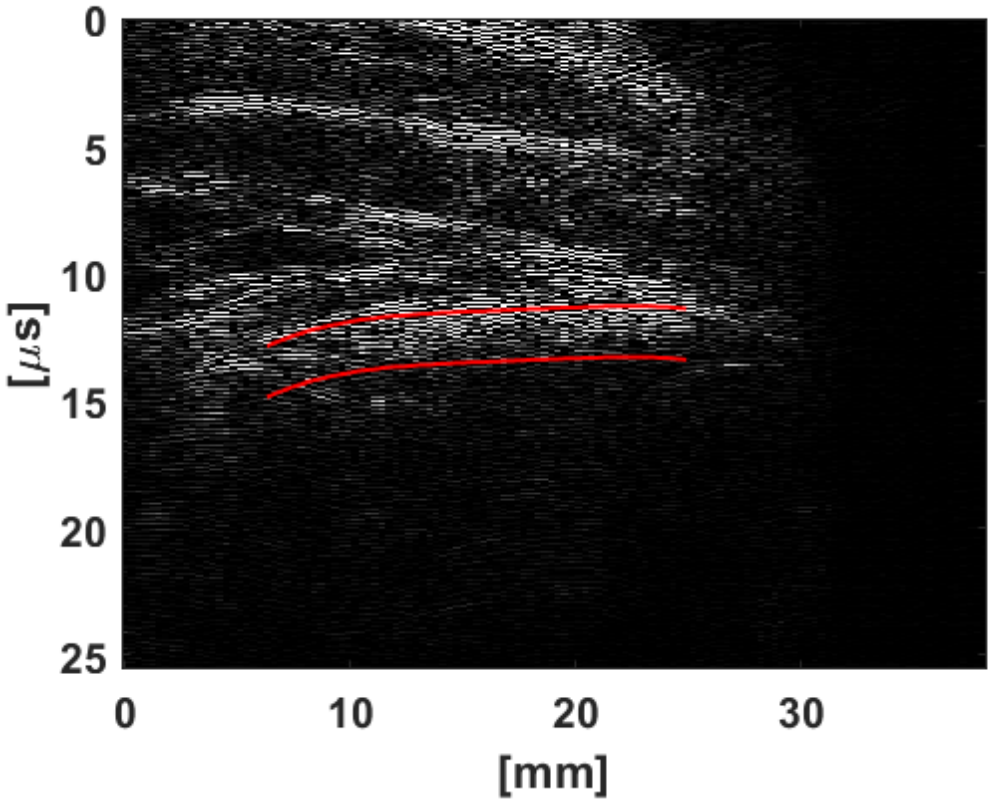

Figure 4-3 To reduce computational costs, the entropy map is obtained only using the signals within the two bounding red lines.

4.2.9 Ultrasound data acquisition and obtaining the entropy map for the lung phantom

Due to the resemblance of air-filled pores to alveoli, a 19×33×63 mm^3 sponge phantom is used to mimic lung parenchyma. To achieve different air VFs, water is added to the sponge and distributed homogeneously through shaking the sample. A linear array transducer with central frequency of 5.2 MHz is used for data acquisition. A 2cm-thick gelatin pad is used as the matching layer between the transducer and the sample. The beam-formed signals are focused on the surface of the phantom and the backscattered envelope detected image data is recorded on the Verasonics Vantage system (Verasonics Inc, Kirkland, WA). A

sliding 1.2×1.2 mm^2 window is used to acquire the entropy map. The windows overlap 50% laterally (limited by the number of elements on the array transducer), and 85% in depth. The experimental setup and schematic process of acquiring the entropy maps are illustrated in Figure 4-4.a and Figure 4-4.b respectively. The bin width of the histogram to get the PDF of the signals is set at 4000.

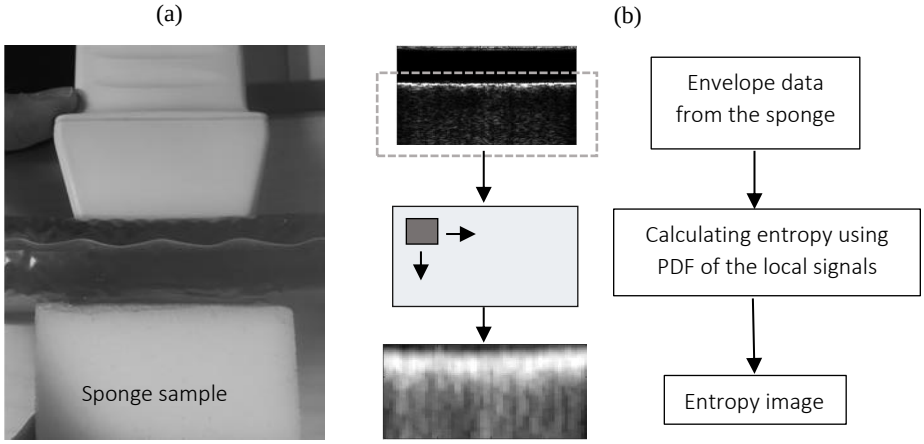

Figure 4-4 a) Experimental setup, b) Schematic process of obtaining entropy images.

4.3 Results

4.3.1 PDMS samples

Figure 4-5.b indicates the entropy average over the 2.4×21.3 mm^2 ROI (Figure 4-5.a) versus scatterer VF percentage of the PDMS samples. To account for deviations in scatterer distributions, three data sets are obtained and processed for each sample. The entropy is indicates an increasing trend with increasing particle VF from 4 to 14%. The increasing trend

is interrupted as VF is increased to 24% which could be due to attenuation and its effect on statistical parameters like entropy.

4.3.2 Cortical bone structures (numerical simulations)

The entropy map of a bone structure is illustrated in Figure 4-6.a. Considering that the multiply scattered signals, convey micro-structural information from a heterogeneous structure like cortical bone, the entropy is averaged over the whole map over a 3.2μs time span. Ct.Po.Dm. for 301 structures used in this study ranges from 51.9 μm to 157.4 μm, and Ct.Po.Dn. ranges from 5.79 $pore/mm^2$ to 16.26 $pore/mm^2$. Minimum and maximum Ct.Po. values are 33.69 % and 51.24% respectively. Figure 4-6.b illustrates the entropy as a function of Ct.Po. An increase in Ct.Po. results in an increase in entropy; however, for highly scattering structures with porosities higher than 45%, the power law fit seems to flatten, indicating a relatively constant entropy range. This is quite similar to the observation from the PDMS samples with the highest scatterer VF Figure 4-6.b and can be explained by increase in attenuation. Figure 4-6.c depicts a positive correlation between Ct.Po.Dm. and entropy (R = 0.74 , p $\ll$ 0.001). Since the average pore diameter ($\overline{Ct.Po.Dm.} = 86.1 \pm 21.5\ \mu m$) has a relatively large standard deviation among the sample population, only the structures within the first (71.7 μm) and second (80.6 μm) quartiles are used to evaluate the entropy versus Ct.Po.Dn. to limit the effect of change in the diameter. Results (Figure 4-6.d) suggest a positive correlation between entropy and Ct.Po.Dn. (R=0.62 , p $\ll$0.001) showing that increase in Ct.Po.Dn. is attributed to increase in randomness in the signals and consequent increase in entropy.

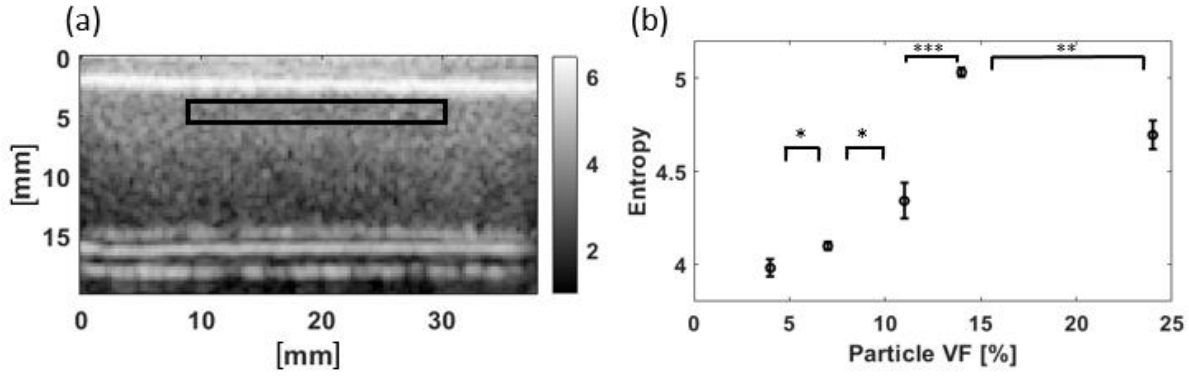

Figure 4-5(a) Entropy image of a PDMS sample with scatterer VF of 4%. The entropy is average over the 2.4×21.3 mm^2 ROI. (b) Average entropy versus scatterer VF.

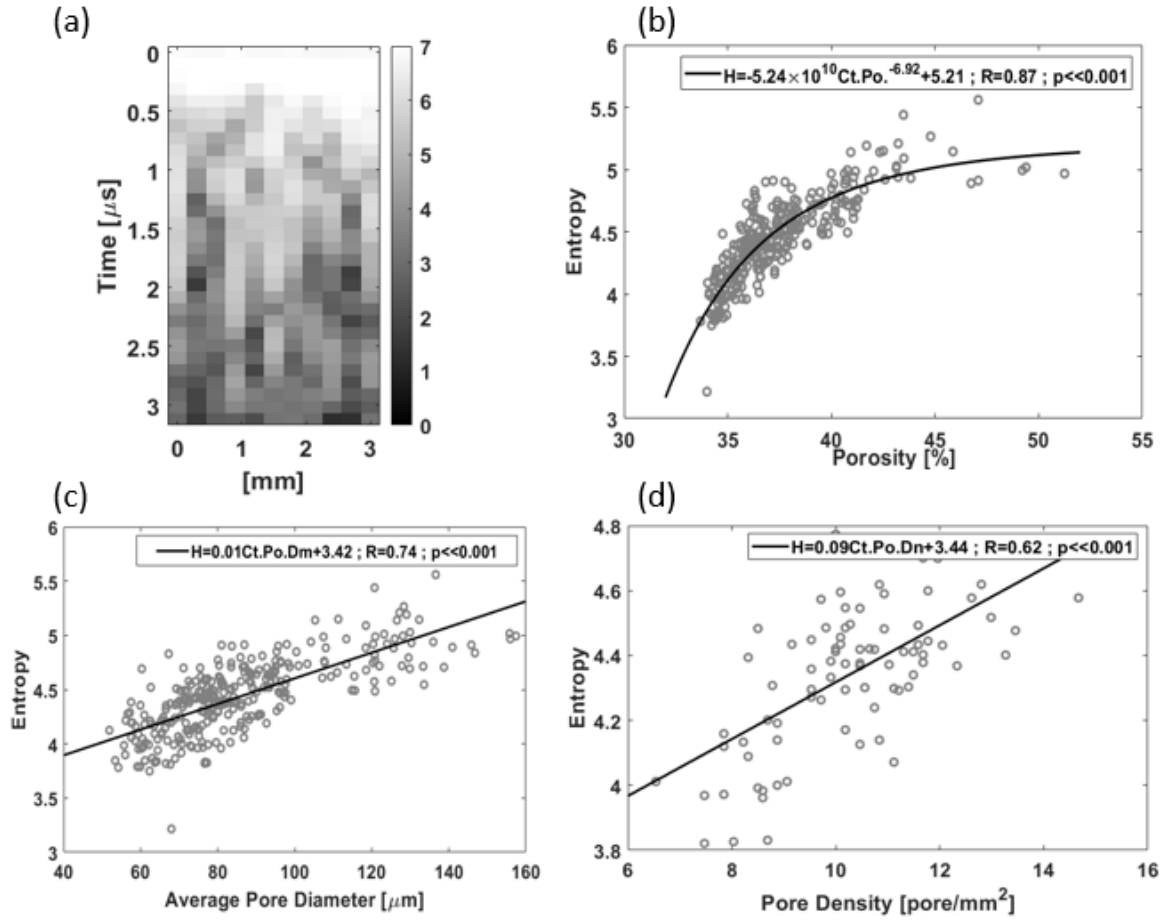

Figure 4-6 (a) Entropy map is formed using the backscattered signals from the bone. Entropy versus (b) Ct.Po. (R=0.87, p≪ 0.001), (c) Ct.Po.Dm. (R=0.74, p≪ 0.001), and (d) Ct.Po.Dn. for structures with 71.7 < Ct.Po.Dm. < 80.6 μm (R=0.62, p≪ 0.001).

4.3.3 Cortical bone (in-vivo experiments)

Figure 4-7 illustrates the entropy map corresponding to the ROI in Figure 4-3. The entropy is averaged over the ROI (all non-zero values in Figure 4-7) and evaluated as a function of structural parameters measured using HRpQCT.

Figure 4-8 summarizes the results for H (mean: 3.17 ± 0.32) versus structural parameters Ct.Po. (mean: 15.89 ± 3.94 %), average Ct.Po.Dm. (mean: $125.87 \pm 18.32\ \mu m$), Ct.Po.Dn. (mean: $1.58 \pm 0.65\ \frac{pore}{mm^2}$) and vBMD (mean: $990.33 \pm 42.70\ \frac{mg}{cm^3}$) measured using HRpQCT for 49 patients. Contrary to the simulation results, here the correlation between the structural parameters and H is not significant ($p>0.05$).

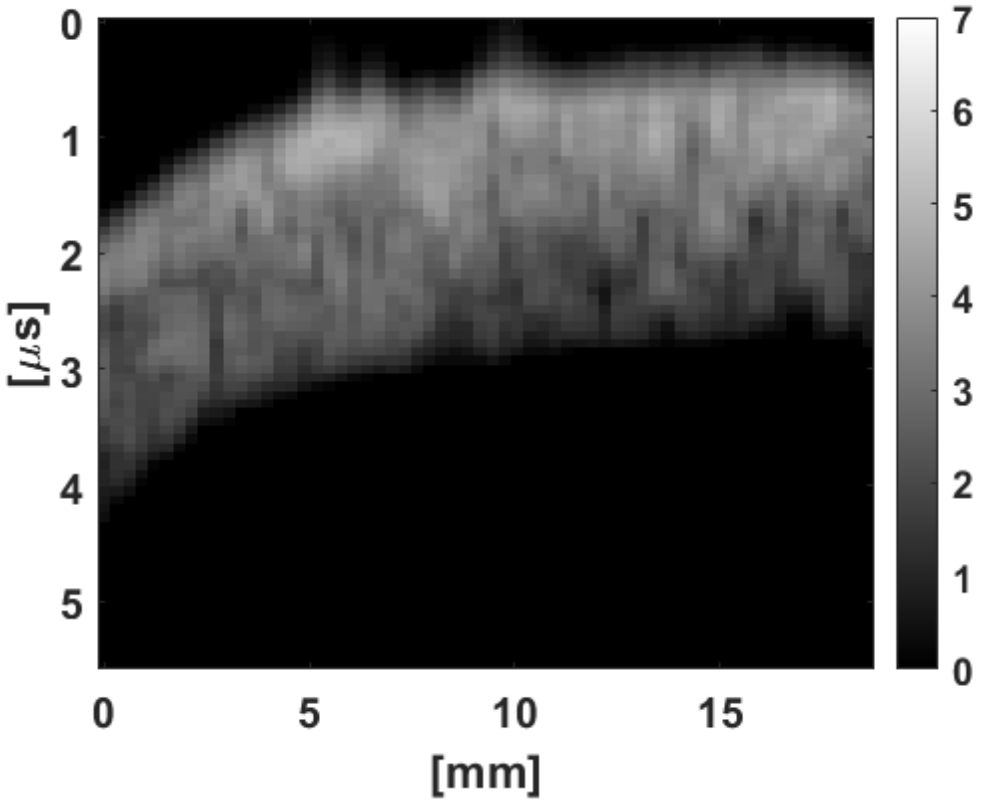

Figure 4-7 Entropy map of the distal tibia.

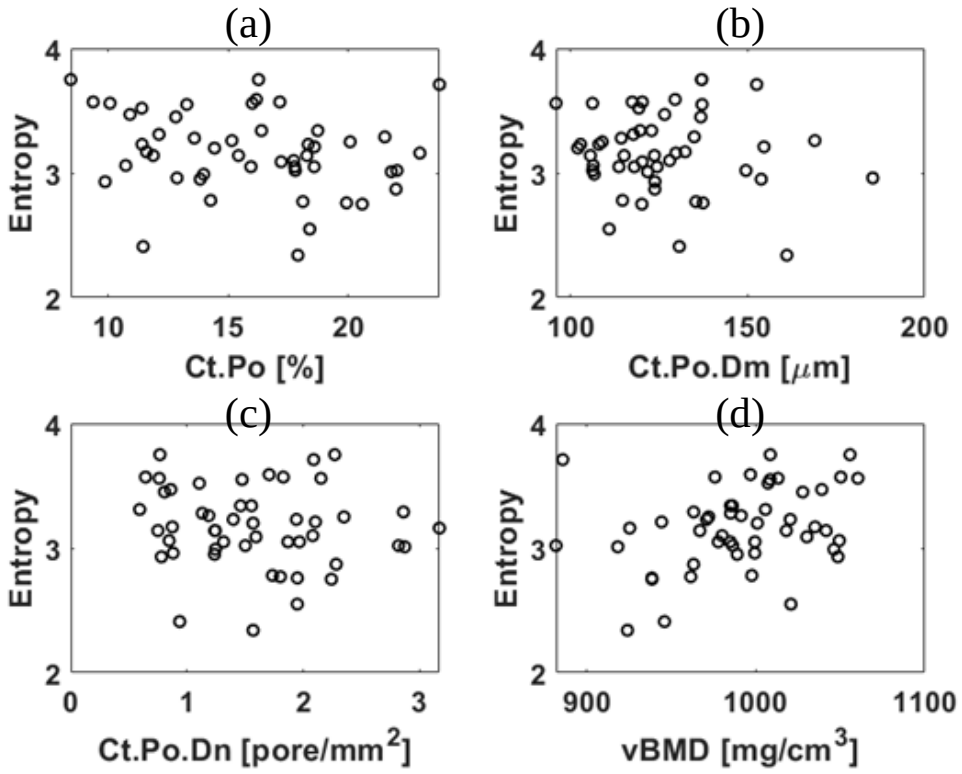

Figure 4-8 H vs (a) CT.Po., (b) average CT.Po.Dm, (c) Ct.Po.Dn. and (d) vBMD.

4.3.4 Lung phantom

Figure 4-9.a illustrates the entropy map for the phantom with 37.32% air VF. Large acoustic impedance difference between the gelatin pad and samples result in strongly reflected signals which are displayed as a region with high entropy value in Figure 4-9.a. A similar discrepancy between material properties of the muscles surrounding the lungs and the alveoli result in very bright lines in lung ultrasound imaging known as the pleural lines. Since boundaries and edges affect the statistics of the signals [196], the $2.5 \times 18.6\, mm^2$ region of interest (ROI) is located deeper into the medium (with approximate 4 mm distance from the top of the sponge). The entropy maps for 32 different air VFs ranging from 1.80 % to 65.82 %

are obtained. Figure 4-9.b depicts the entropy averaged over the ROI versus air VF. A positive and significant correlation between the two parameters is observed (Pearson correlation coefficient R = 0.67, p<<0.001).

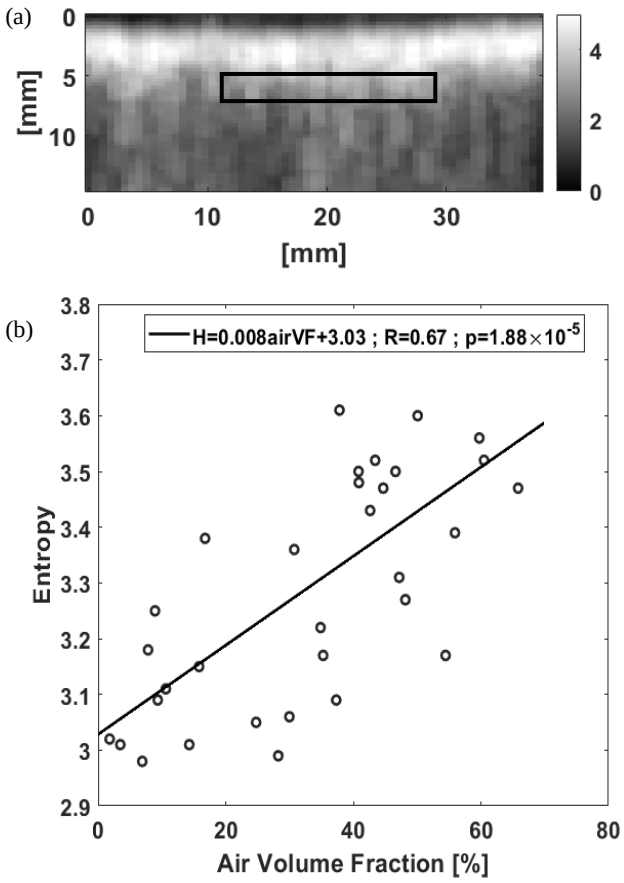

Figure 4-9 a) Entropy image of a sample with 37.32% air VF, b) Average entropy over ROI versus air VF.

4.4 Discussion

4.4.1.1 PDMS phantoms and cortical bone (numerical simulations)

In the past, statistical parameters such as entropy have been successfully exploited in QUS studies to evaluate structural changes in biological tissues such as liver and breast[177,180,181]. In the present study, we use entropy as a measure of randomness in ultrasound backscattered signals to assess PDMS samples with different concentrations of BaTiO3. The entropy results indicate an increasing trend as BaTiO3 VF increases from 4% to 15% suggesting that this parameter is significantly correlated ($p < 0.05$) to changes in the heterogeneity in the medium (Figure 4-5). While for lower VFs the entropy proves effective, with increase to 15% VF, it decreases. This observation can be justified by the fact that signals in highly scattering media are attenuated at higher rates. The attenuation in the signals, results in a reduction in the amplitudes and subsequent calculated entropy values since variance in the amplitudes reduces as well. While compensation for the attenuation might be a plausible solution, we believe that at high VFs, that would result in normalization of the noise which not only does not convey structural information from the deeper parts of the sample, but also introduces more errors to the overall QUS evaluation. Using the PDMS-BaTiO3 phantoms allows us to control the scatterer volume fraction and evaluate its effect on entropy. The control that we have on scatterer volume fraction and high absorption capacities of PDMS resemble a highly scattering and absorbing structure like cortical bone. Based on our findings on applicability of entropy measurement in PDMS samples with different levels of heterogeneity, we applied the same approach to evaluate cortical bone structures. Considering that in highly scattering media like cortical bone the concept of pulse-echo imaging is not valid due to the diffusion of the wave, we obtained the entropy maps in time rather that depth (Figure 4-6.a). In

other words, there is no linear relationship between propagation time and propagation distance. While a power-law fit indicates a positive correlation between Ct.Po. and entropy for porosities below 45%, the entropy plateaus at higher porosities (Figure 4-6.b) which is similar to Figure 4-5.b suggesting that attenuation is the dominant phenomenon affecting the entropy value due to changes in the signal amplitude. On the other hand, Ct.Po.Dm. is showing a monotonous behavior and is highly correlated (R=0.74, $p \ll 0.001$) with the entropy (Figure 4-6.c). Due to large variation in Ct.Po.Dm. (mean = 86.1 μm, std = 21.5 μm), the structures with Ct.Po.Dm. ranging from 71.7 μm (first quartile) to 80.6 μm (second quartile) are used to investigate the effect of change in Ct.Po.Dn. on entropy. Hence, only 75 out of the total 301 bone images are used in Figure 4-6.d where entropy is monotonously increasing with Ct.Po.Dn. ($R = 0.62$, $p \ll 0.001$). The reason to limit the number of structures, is to keep the diameter relatively constant while evaluating the effect of changes in Ct.Po.Dn. on entropy separately. To further study the independent effect of changes in the micro-structure on entropy, a larger data set needs to be exploited in the future where Ct.Po.Dn. and Ct.Po.Dm. are kept constant.

4.4.1.2 Cortical bone (in-vivo experiments)

Contrary to the simulation study, the changes in the micro-structural parameters Ct.Po., Ct.Po.Dm., Ct.Po. did not result in monotonous behavior in H. One possible explanation could be the limitations that are associated with the HRpQCT. Since the resolution of HRpQCT (60μm) was relatively large compared to the physiological range of the cortical average pore diameter (40-100μm [126]), smaller pores were not accounted for in our experimental study. Hence, the presented micro-structural parameters (Ct.Po.Dm., Ct.Po.Dn. and Ct.Po.), may not have provided an accurate representation of cortical bone. This is especially a valid point

considering the reported range of the cortical pore density (6-30 $\frac{pore}{mm^2}$ [136,139]) and pore diameter (40-100 μm [104,126]) in the literature. This means that while based on our HRpQCT data, the results of average Ct.Po.Dm. for two patients is different, if we take the smaller pores into account, they might have quite the same average Ct.Po.Dm. resulting in very small deviation in H (as it is observed in Figure 4-8.b). The same explanation would apply to Ct.Po.Dn. and Ct.Po. with which H was not significantly correlated. Ct.Po.Dn. in particular did not have large variance (mean: $1.58 \pm 0.65 \frac{pore}{mm^2}$), so regardless of the resolution limitations, it was expected to get similar H values. It is worth noting that our collaborators have confirmed that ultrasound backscatter and attenuation coefficients also do not demonstrate significant correlations with micro-structural parameters obtained from HRpQCT, however, those attenuation and backscatter coefficient are in association with the fracture incidents. An ongoing study is being done to evaluate the correlation between the fracture risk and D.

4.4.1.3 Lung mimicking phantom

The difficulties in conventional lung ultrasound imaging has led to implementation of qualitative artifact-detecting methods which are highly operator-dependent and vary based on the frequency [192]; hence, finding an alternate quantitative approach is crucial. The present study investigates the feasibility of using Shannon entropy as a statistical parameter to evaluate the multiply scattered signals in a heterogeneous medium mimicking lung. We used a thick gelatin pad as the matching layer to mimic the soft tissue that surrounds the lungs and covers the rib cage. While there are certain differences between the texture and material properties of living tissues with our experimental setup, we think that this preliminary study introduces an effective QUS method for lung tissue characterization. The results indicate that entropy is positively

correlated with air VF of the phantoms ($R = 0.67$, $p<<0.001$). It would be useful to assess the influence of frequency and scattering regime to optimize the effectiveness of statistical analysis of the backscattered signals in a future study. For cases with high air VF, attenuation reduces the penetration of the signals into the medium; hence, depth of the ROI is limited to approximately 6.5 mm from the surface of the phantom. We believe that in-vivo experiments might allow for more penetration due to differences between the material properties of the lung tissue and our phantoms. The preliminary results presented here, suggest that entropy as a measure of disorder in the signals can potentially be beneficial to monitor clinical edema cases.

4.5 Conclusion

The aim of the present study is to evaluate effectiveness of a statistical parameter like Shannon entropy as a measure of randomness in the backscattered signals with respect to micro-structural changes in cortical bone and a lung mimicking phantom. The simulations on cortical bone structures (Ct.Po., Ct.Po.Dm. and Ct.Po.Dn.) result in significant correlations with entropy. We believe that in the in-vivo study the limitations such as low resolution of HRpQCT might have affected the measured structural parameters. An ongoing study is being done on low-trauma incident fractures and their correlation with H, as well as other parameters such as attenuation and the diffusion constant to further evaluate the potentials of these QUS parameters to characterize biological tissues.

In addition to cortical bone and highly scattering PDMS phantoms, a lung-mimicking porous phantom with varying air VF is assessed through measurements of entropy. The

positive correlation between air VF and entropy suggests that it can potentially be exploited to assess pulmonary edema.

Chapter 5: Diffusion constant measurement of contrast enhanced phantoms mimicking vascular networks using super-harmonics

5.1 Introduction

The growth of the blood vessels from existing vessels is known as angiogenesis and is one of the fundamental markers of tumor growth and metastasis [197]. There are different imaging modalities to image vasculature and characterize tumorous and healthy tissues. Convenience, low cost, high spatial and temporal resolution, and non-invasiveness make ultrasound a desirable imaging modality compared to magnetic resonance imaging and micro-computed tomography imaging which respectively have low acquisition rate and ionization risks. Ultrasound Doppler imaging exploits the flow of the red blood cells in the vessels to obtain an image from the vasculature and works well when blood flow is sufficiently fast; however, when the rate of the blood flow is the same order as the tissue movement, Doppler imaging cannot discriminate between the vasculature and the surrounding tissue. Dual-frequency contrast enhanced ultrasound imaging is another modality which takes advantage of the nonlinear behavior of the bubbles injected in the blood stream to suppress the response from the tissue_ which does not demonstrate non-linear properties beyond the second harmonic [198,199]_ and obtain exclusive information from the vascular system. The micro-scale size of the bubbles prevents them from leaking into the extravascular space making contrast enhanced ultrasound imaging techniques desirable for characterization of biological processes such as angiogenesis that are associated with abnormalities in the vasculature. Dual frequency contrast

enhanced ultrasound imaging with the purpose of microvessel segmentation has been done in the past [200,201]. Improvements in superharmonic acoustic angiography have resulted in high contrast, high resolution (100-200 μm) images [202–204]. However, the small field of view both in depth and in axial direction is one of the limitations of high-spatial-resolution acoustic angiographic imaging [201]. In addition, it is computationally demanding in case of offline post-processing with the purpose of quantitative analysis.

There have been several quantitative ultrasound studies that investigate the scattering properties of contrast agents such as backscatter coefficient and attenuation with respect to pressure and frequency [205–207]. Changes in the concentration of scatters, their spacing, size and their acoustical properties affect the diffusivity of ultrasound waves in scattering media. The rate at which the wave diffusive halo grows in a scattering medium is indicated by the diffusion constant (D). This parameter has proven to be sensitive to micro-architecture of heterogeneous media [91,113,117]. There have been studies on bone and lung which employ a similar approach to investigate micro-structural changes based on the changes in the diffusion constant [166,194,208].

The increased tortuosity and complexity of the vessels in tumorous tissue affect the backscattered signals and can potentially be used to characterize healthy and diseased tissues. In a study by Mohanty et al [209] significant differences between diffusion constant of the vasculature of tumorous tissue and control tissue are observed. In the present study, we propose a similar quantitative ultrasound approach to characterize vessel networks with different vessel spacing by comparing the diffusive properties of different vasculature phantoms. Since it is desired to minimize the response from the tissue surrounding the vessels, a dual frequency approach is implemented in this study to obtain the superharmonic signals from the bubbles in the vessels.

5.2 Methodology

5.2.1 Microbubble preparation process

Microbubbles are bubbles traditionally containing a perfluorocarbon gas core surrounded by a phospholipid shell. The first step to creating microbubbles is to make the lipid solution. The lipid solution contains the lipids DSPC (1,2-distearoyl-sn-glycero-3-phosphocholine) and PEG2000 (1,2-distearoyl-sn-glycero-3-phosphoethanolamine-N-[methoxy(polyethylene glycol)-2000]) mixed with glycerol, propylene glycol, and PBS buffer. The lipid solution is then aliquot into vials with some air headspace. The vials are then sealed and capped. The headspace currently containing air is then gas-exchanged with the desired perfluorocarbon, decafluorobutane (DFB). This is done by vacuuming out the air with a vacuum pump followed by flowing in DFB several times within a contained gas-exchanged system. The final step in activating microbubbles is the vial containing the lipid solution and DFB headspace are mixed aggressively using an amalgamator, creating a foamy white solution which have microbubbles of various sizes. The microbubbles are best used soon after being activated, typically within a few hours. Microbubbles are stable if left sealed in 4°C for at least a month.

5.2.2 Phantom manufacturing procedure

The phantoms are made by Dr. Michael Daniele's group at NC State University. The first stage of the vessel phantom creation process involves using photolithography in a clean room to print a thin vessel design on the surface of a four inch silicon wafer. The surface of the wafer is ionized in a plasma cleaner for two minutes. The wafer is then moved under a hood and placed on a rotor. 4 mL of SU-8 2150 is then poured onto the wafer and spread evenly

across the ionized surface by the spinning motion of the rotor. The wafer is placed onto a 65 degrees Celsius hot plate for seven minutes and then moved to a 95 degree Celsius hot plate for an hour. The wafer is then moved into an exposure machine and placed under a filter sheet that has the desired vessel design. This vessel design filter sheet ensures that during the exposure process, only certain parts of the wafer surface are polymerized. What is left is the desired vessel pattern engrained in the resin surface of the wafer. The wafer is then placed back on the 65 degree Celsius hot plate for five minutes, the 95 degrees Celsius hot plate for 20 minutes and then the 65 degrees Celsius hot plate for another five minutes. The wafer is then placed in a dish of SU-8 developer under the hood and transferred into an ultrasonic bath until all bubbles on the edge of the wafer are gone. The wafer is then taken out of the SU-8 developer fluid, rinsed with acetone and isopropyl, then dried using an air gun. The wafer is then placed on the 65 degrees Celsius hot plate for three minutes then moved to a 150 degrees Celsius hot plate for 30 minutes. The hot plate temperature is then changed to 25 degrees Celsius and the wafer is left to cool for about an hour.

Polydimethylsiloxane (PDMS) is used to create the primary molds used to form the vessel structures. PDMS curing agent and PDMS elastomer are mixed together at a ratio of 1:10 curing agent to elastomer. The mixture is placed in a dessicator and degassed until all of the bubbles have left the mixture. The vessel printed wafer created in the cleanroom is obtained and placed on a sheet of foil. The edges of the foil are bended up around the edges of the wafer to give it walls. The wafer service with the vessel imprint is facing upwards. Half of the PDMS mixture is poured onto this wafer surface. The other half is poured into an identical circular foil dish without a wafer in it. Both PDMS samples are cured on a hot plate at 120 degrees Celsius for 20 minutes or until they have become solid. They are then removed from the hot

plate and the foil is removed from both samples. The PDMS on top of the wafer is carefully removed in one piece and should have a reverse vessel design nicely carved onto it. The other piece of PDMS should have its center cut out so it can serve as a wall around the vessel design printed on the first PDMS sample. These two pieces of PDMS are then bonded together using a plasma cleaner. Porcine gelatin is then combined with de-ionized water at a ratio of 1 gram gelatin powder for every 9 mL of water. The mixture is refrigerated and then sonicated in an ultrasonic bath. Half of the gelatin mixture is then poured into the PDMS vessel mold. The other half is poured into a similarly sized dish. These samples are refrigerated for a minimum of three hours, then taken out of the fridge and removed from the PDMS mold and blank dish. The two surfaces are combined using 1% rose bengal solution and bonded under 530-560 nm light. A razorblade is then used to cut along the printed divides between different vessel structures. The separated phantoms are then put in a small dish that is then filled to phantom height with 1% rose bengal and placed back under the light source. After 30 minutes the dish is removed and the phantoms are tested for flow. Two different sets of phantoms with tube spacing of 1mm (tube thickness = 500μm) and tube spacing of 1.5mm (tube thickness = 750μm) are designed and manufactured following the mentioned procedures. Figure 5-1 illustrates a phantom with 8 vessels that are 1mm apart.

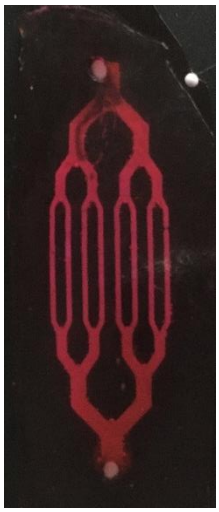

Figure 5-1 Phantom with 8 vessels with thickness of 500μm and spacing of 1mm.

5.2.3 Dual-frequency co-linear array transducer design and fabrication

An array with 64 transmit (T) and 128 receive (R) elements is designed and fabricated. While these two sets of elements need to be separated physically, they need to have overlapping foci; hence, the pitch of the elements is designed accordingly. Table 5-1 summarizes the design parameters for the co-linear array transducer. The T and R elements are coupled with nickel and alumina/epoxy isolation layers. The air backing used for the low frequency elements improves the transmission sensitivity. The materials used for T and R elements are PZT ceramic (CTS 3203HD, CTS Corporation, Elkhart, Indiana, USA) and 2-2 composites respectively. A 30 μm layer of E-solder separates the T and R elements to reduce the interference. More details on the fabrication process of this transducer are included elsewhere [210].

Table 5-1 Design parameters of the co-linear array transducer

Aperture	$8mm \times 18\ mm$	
Working mode	Transmission (3 MHz)	Reception (15 MHz)
Pitch	$280\ \mu m$	$140\ \mu m$
Element number	64	128

5.2.4 Data acquisition

A bolus injection of microbubbles into the gelatin sample is done such that all the vessels are filled with the bubbles. The white color of the bubbles makes it easy to observe the regions they have covered and detect a probable cloggage in the transparent phantoms. The phantom is then submerged in water and positioned next to the transducer such that the vessels would be parallel to the array of the elements. Figure 5-2 depicts the experimental setup.

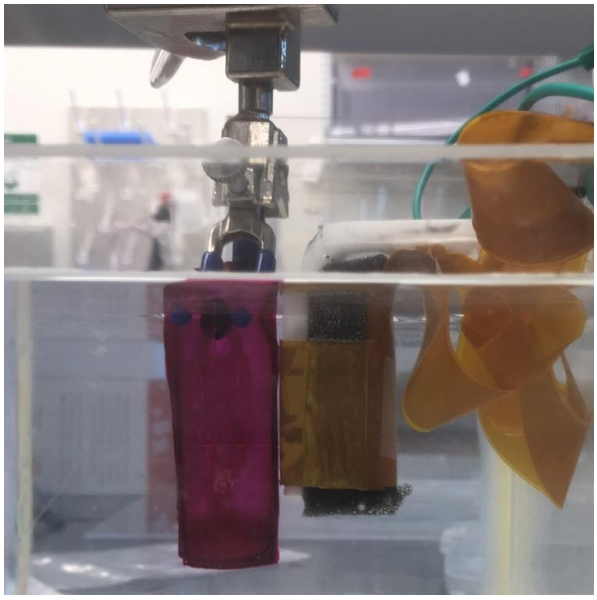

Figure 5-2 The experimental setup

Considering the size and acoustical properties of the bubbles, they are expected to resonate in the frequency range of 2-4 MHz and their superharmonic response detected from frequencies above 15 MHz results in a high contrast-to-tissue and high resolution [203]. To acquire the inter-element response matrix (IRM), each element in the transmission array emits a 3 MHz pulse. The resonating bubbles then produce high-frequency harmonics that are received by the high-frequency component of the co-linear array transducer. For each single

emission sequence, there is reception on all 128 elements. The process is repeated for all 64 transmitting elements, until a $64 \times 128 \times N$ response matrix is obtained where N is the number of time data points. In addition to dual-frequency data acquisition, a single frequency acquisition at 15 MHz is also performed using only the 128 high-frequency elements. The sampling frequency for all acquisitions is 62.5 MHz.

5.2.5 Post-processing the data

The diffusion constant is calculated as instructed in section 2.4.2.3.

5.3 Results

5.3.1 Single frequency experiments

At central frequency of 15MHz the inter-element matrix is obtained for phantoms with 1mm tube spacing and 1.5mm tube spacing. As explained in the methodology section, the backscattered intensity and its incoherent contribution are calculated. Figure 5-3 illustrates the backscattered intensity I and incoherent intensity I_{inc} for two different phantoms. The normalized incoherent intensity demonstrates a growth over time which can be exploited to calculate the diffusion constant. The fluctuations in I_{inc} are resulted due to the dominance of the reflections from the tubes, because at those locations, the signals received from the emitter and receiver pairs that are far from each other are minimal; as if the signal has not traveled into the multiple scattering medium. However, in spite of these local effects, the diffusive halos (Figure 5-3.b and Figure 5-3.d) show an overall spatial growth in incoherent intensity with increase in time which allows us to obtain the diffusion constant which is associated with micro-structure of the scattering medium.

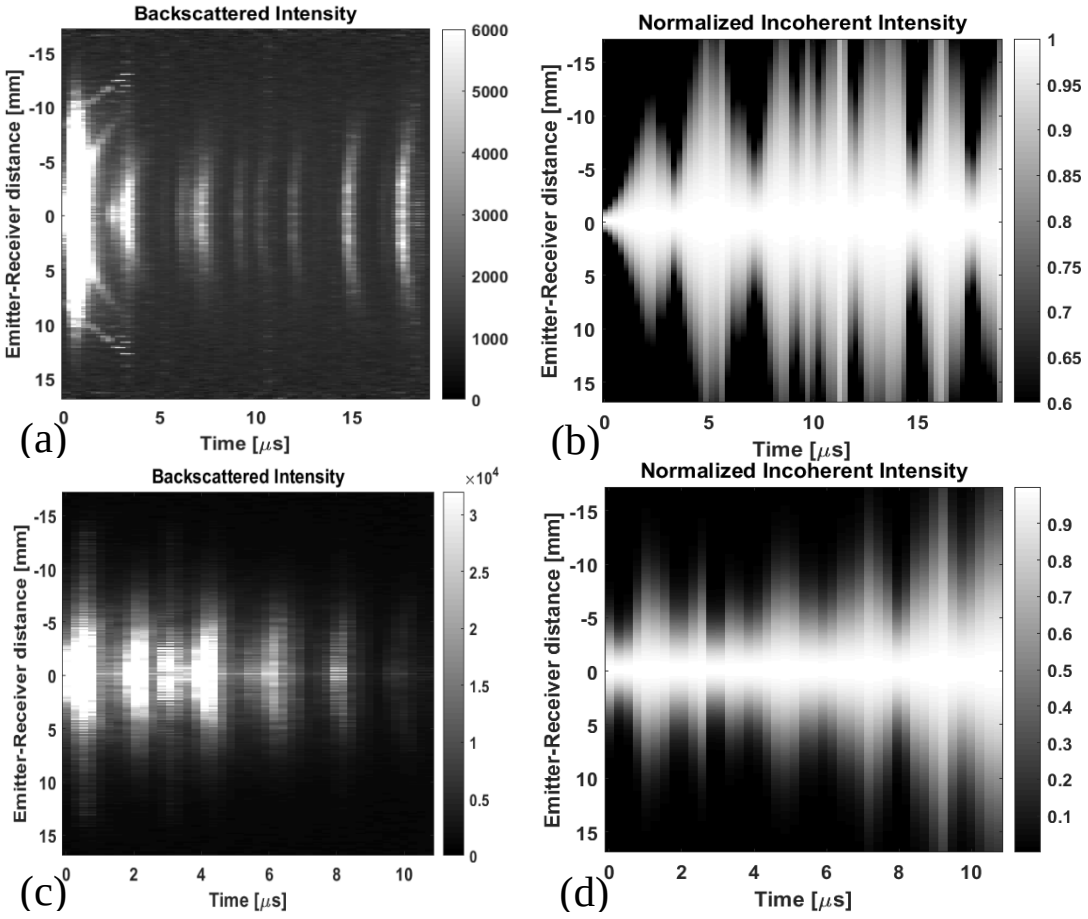

Figure 5-3 Backscattered intensity (a) and normalized incoherent intensity (b) of a phantom with tube thickness of 750μm and tube spacing of 1.5mm. Backscattered intensity (c) and normalized incoherent intensity (d) of a phantom with tube thickness of 500μm and tube spacing of 1mm.

At each time-window the variance of the Gaussian curves fitted to I_{inc} linearly increases with time. Figure 5-4 depicts the variance-time plots for two different phantoms. The slope of the linear fit is proportional to D.

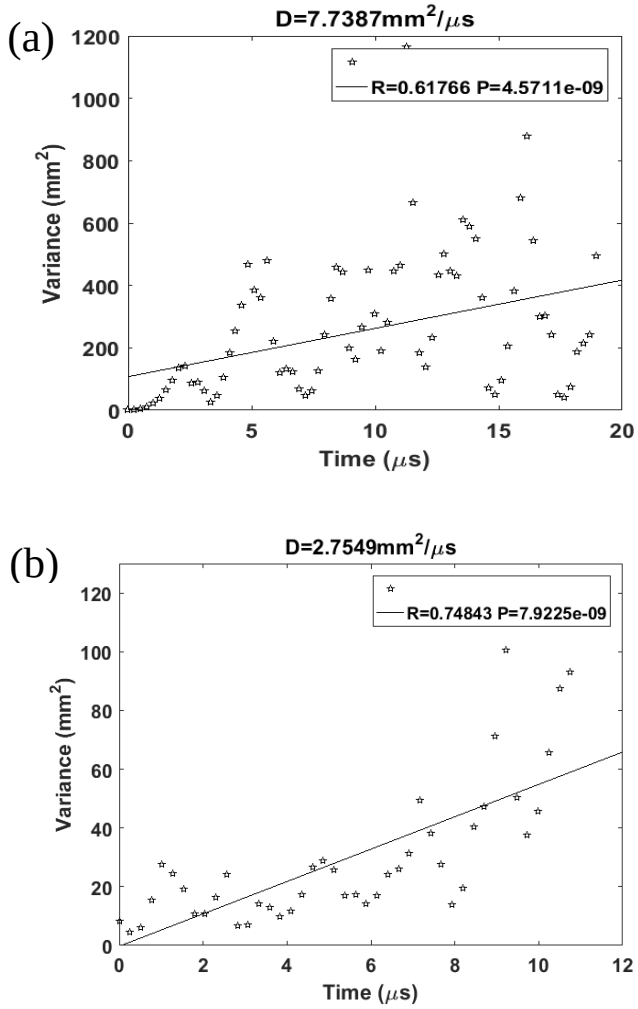

Figure 5-4 Variance-time plots for (a): a phantom with tube thickness of 750μm and tube spacing of 1.5mm (D=7.34mm^2/μs) and (b): phantom with tube thickness of 500μm and tube spacing of 1mm (D=2.75mm^2/μs).

Figure 5-5 summarizes the diffusion constant results for two phantoms with tube spacing of 1mm (mean D = 2.02 $mm^2/\mu s$, std. = 0.62 $mm^2/\mu s$) and one phantom with tube spacing of 1.5mm (mean D = 8.26 $mm^2/\mu s$, std. = 0.62 $mm^2/\mu s$). To account for the errors, IRM for smaller and larger phantoms is acquired 4 and 3 times, respectively. The T-test performed on the two sets of D values demonstrates a significant difference between them ($p = 1.25 \times 10^{-7}$).

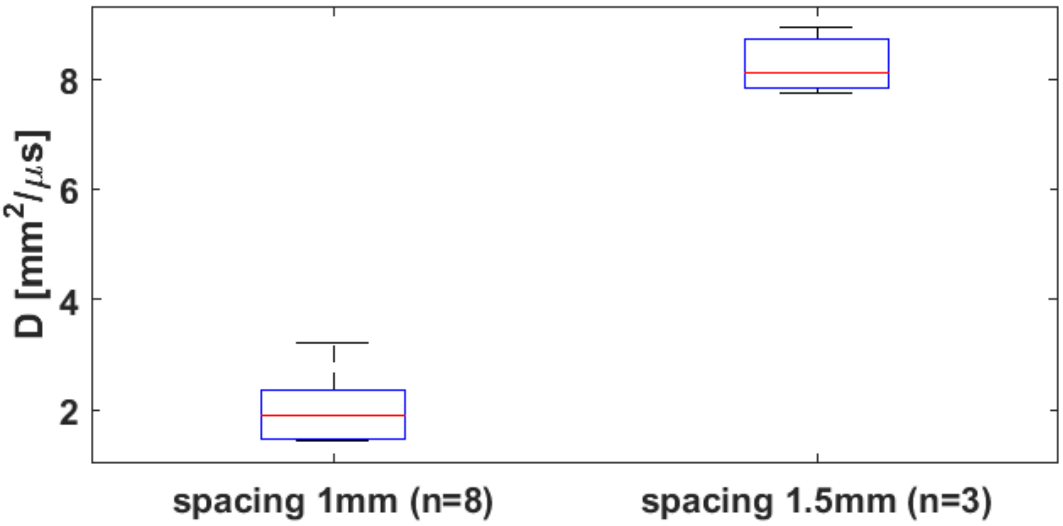

Figure 5-5 Diffusion constant values for a phantom with tube thickness of 750µm and tube spacing of 1.5mm and two phantoms with tube thickness of 500µm and tube spacing of 1mm. n shows the number of IRM acquisitions.

5.3.2 Dual frequency experiments

While theoretically dual-frequency contrast enhanced experiments are favorable in terms of isolating the response exclusively from the bubbles, the reduced pressure at higher harmonics makes it complicated to process the data as multiply scattered signals and the noise from the system are at the same order of amplitude. As explained in the methodology section, knowing the emitter-receiver distances is crucial in D calculation; hence, to implement our method, it is necessary to use a prototyped transducer which has both low-frequency and high-frequency arrays stacked on top of each other, and using two separate commercially available array transducers is redundant. To improve the SNR, instead of 1 element, 4 elements are used to transmit the 3MHz signals into the phantoms. The 4 element sub-apertures with 50% overlap are used for transmission of the signals. To elaborate, the first and second emissions are done by elements 1-4 and 3-6 respectively. The 128 received signals at 15 MHz are averaged

according to size of the emitting aperture to obtain inter-element matrices with the same number of emitters and receivers. In spite of the efforts made to improve SNR, high levels of noise caused failure to calculate the diffusion constant for phantoms with $750\mu m$ tube thickness and 1.5mm spacing. Figure 5-6 demonstrates the backscattered intensity and incoherent intensity for one of these phantoms (aperture length for each emission: 4 elements with 50% overlap).

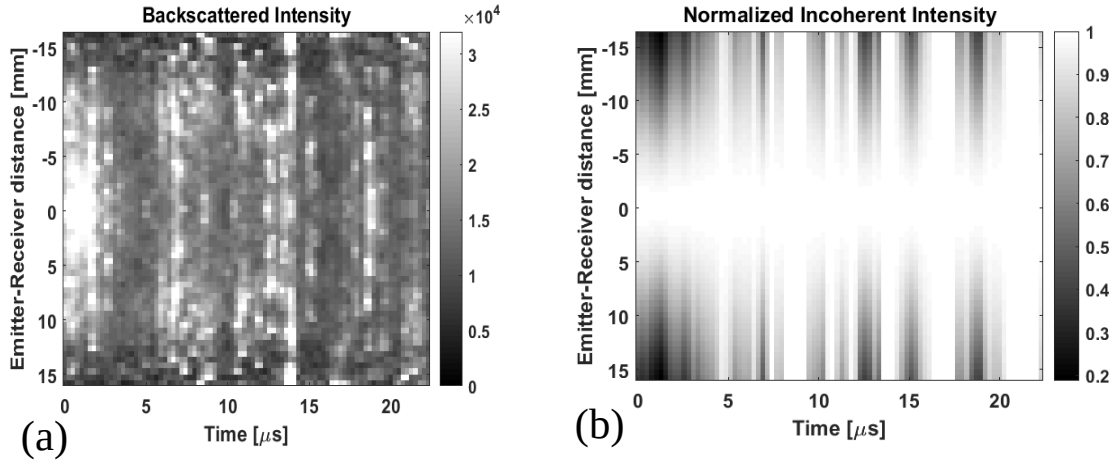

Figure 5-6 Backscattered intensity (a) and normalized incoherent intensity (b) for a phantom with 750µm tube thickness and 1.5 mm spacing. To improve the signals, at each emission event, 4 elements are used to transmit the 3MHz waves.

Backscattered intensity, its incoherent contribution and variance-time graph for a phantom with tube thickness of $500\mu m$ and spacing of 1 mm are shown in Figure 5-7. Similar to the previous case, aperture length is 4 elements (with 50% overlap) and the transmitting and receiving frequencies are 3 and 15 MHz respectively. The IRM acquisition on this phantom is repeated for three times and the resulted D values are 3.31, 3.86 and 4.65 $mm^2/\mu s$ (mean: $3.94\frac{mm^2}{\mu s}$, std.: $0.67\frac{mm^2}{\mu s}$).

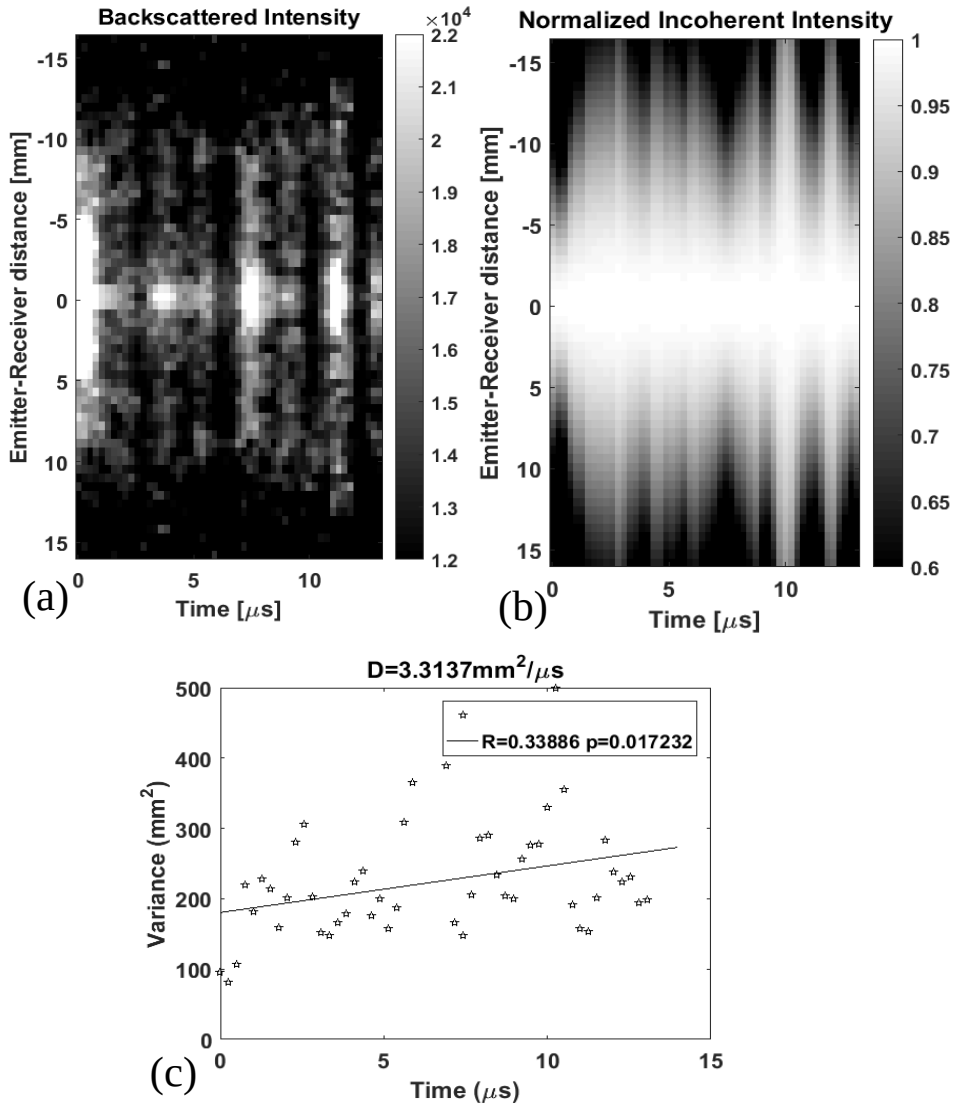

Figure 5-7 Backscattered intensity (a), normalized incoherent intensity (b) and variance-time graph (c) for a phantom with 500μm tube thickness and 1 mm spacing. To improve the signals, at each emission event, 4 elements are used to transmit the 3MHz waves.

5.4 Discussion

A prototyped dual-frequency co-linear array transducer is used to transmit pulses at 3 MHz to excite the microbubbles inside the vessels at a frequency close to their resonance frequency. The ultrasound signals which are the result of backscattering due to acoustical impedance difference between the bubbles and surrounding tissue and the non-linear

oscillations of microbubbles due to resonance [211], are then received at 15 MHz by the elements on the high-frequency array. Since the harmonics are different from the signals reflected from the tissue, they are the signature of microbubbles and give information exclusively from the vasculature. Moreover, the attenuation is limited to one-way, since bubbles act as sources of the high-frequency harmonics [201].

The diffusion constant is measured for gelatin phantoms mimicking 8 parallel vessels using the single frequency and dual frequency approaches. When transmitting and receiving at 15 MHz, increase in the spacing from 1 to 1.5mm results in an increase in the diffusion constant. The difference between D is significant ($p=1.25\times 10^{-7}$) for two different phantoms suggesting that this parameter can potentially be used to address the micro-structural changes in the vasculature. While these preliminary results are promising, efforts in designing more complex phantoms and increasing the variety of vessel sizes and spacing need to be made. Efficiency of the prototyped transducer also has a major role in the outcome of the experiments. In addition, uneven distribution of the bubbles in phantoms, resulted from the complexities of the manufacturing process, residual material left within the vessels and possible cloggages leads to interruption in the linear trend between variance and time as the diffusive halo grows.

The dual-frequency experiments suffer from poor signal to noise ratios to the extent that even after using 4 elements_ instead of 1_ for emission of the signal, no reliable diffusion constant value has been calculated for larger phantoms with tube thickness of $750\mu m$ and spacing of 1.5mm. D values measured for a phantom with tube thickness of $500\mu m$ and spacing of 1mm using the dual-frequency approach (mean D= $3.94\frac{mm^2}{\mu s}$) are slightly larger than the ones

measured with a single frequency (mean D= 2.02$\frac{mm^2}{\mu s}$) but they are still significantly different ($p=1.73\times 10^{-6}$) from D of the larger phantoms (mean D= 8.26$\frac{mm^2}{\mu s}$).

5.5 Conclusion

The sensitivity of the diffusion constant to vessel spacing makes this quantitative ultrasound approach a potential modality to detect tumorous tissue since angiogenesis is associated with increase in the density of the vessels. While there have been significant improvements in the high-spatial resolution acoustic angiographic imaging, heavy post-processing is required to obtain the quantitative parameters like density and spacing of the vessels. The diffusion constant, on the other hand, is sensitive to scatterer spacing and size and can potentially be exploited to link acoustical parameters such as transport mean free path and scattering mean free path to micro-structure of the medium. Our proposed technique successfully characterizes vessels with different spacing using a single frequency approach. A dual-frequency approach for measurement of the diffusion constant is proposed for the first time and the results are aligned with the ones obtained at single frequency. Improvements in the design of the dual-frequency transducer are vital since poor SNR is one of the major drawbacks of this project. Designing more complex vessel phantoms and conducting in-vivo experiments can be done in future to extend and support the present findings.

Chapter 6: Conclusion

Conventional ultrasound imaging based on echolocation is not practical in tissues such as bone and lung due to multiple scattering of ultrasound waves. In such media, the relation between distance and time is not linear. Ultrasound multiple scattering is influenced by the heterogeneities in the medium. Parameters such as the diffusion constant and ultrasound attenuation, as well as statistical parameters such as Shannon entropy are associated with multiple scattering and take advantage of this phenomenon to characterize different heterogeneous media based on micro-structural changes. This thesis summarized three QUS approaches which were used to characterize biological tissues. While the main focus of the present work was on the characterization of cortical bone, other tissues like kidney and lung mimicking phantoms were evaluated as well.

In chapter 2, the diffusivity of ultrasound waves in heterogeneous structures was studied. We conducted FDTD simulations on cortical bone structures and found a negative correlation between D and micro-structural parameters including Ct.Po., Ct.Po.Dm. and Ct.Po.Dn.. We found that Ct.Po.Dm. had a power law relation with D and at higher pore diameters, the diffusion constant did not change significantly. The in-vivo experiments on the distal tibiae of 49 patients supported this finding. The mentioned experimental study is still ongoing, and we hope to find associations between parameters such as D, entropy, attenuation, backscatter coefficient and low impact fractures in cortical bone in the future. D was also used to evaluate CKD in cats based on the changes in the contrast enhanced vasculature of the kidney. Using this parameter we found a significant difference ($p<0.01$) between healthy and diseased cases.

In chapter 5, D was measured for contrast enhanced vasculature phantoms at the fundamental frequency and at the fifth harmonic frequency using a dual frequency transducer. Obtaining the backscattered signals at higher harmonics resulted in suppression of the response from the tissue (in this case the gelatin phantom) and getting the information exclusively from the contrast enhanced vessels. The information from the vasculature can be especially beneficial in assessment of angiogenesis. We successfully characterized vessels with respect to the vessel spacing using the single frequency approach. However, further improvement in the design of the transducer is vital to successfully implement the dual frequency approach.

In chapter 3, attenuation coefficient and its scattering and absorption coefficients were studied in cortical bone structures using FDTD simulations. The simulations not only allowed us to have control over the micro-structure, but also made it possible to obtain the attenuation exclusively due to scattering in non-absorbing structures and separate the scattering and absorption contributions. The results indicated that increase in either pore diameter or density in low/intermediate scattering regimes was associated with increase in attenuation coefficient as a result of increase in scattering. In higher scattering regimes, increase in either pore size or pore density resulted in an increase in attenuation as a result of increase in the apparent absorption coefficient which indicated that the wave had travelled longer paths in the absorbing bone matrix. A spectroscopy analysis, confirmed these findings and indicated that in higher scattering regimes ($k\phi > 0.8$) the apparent absorption coefficient followed a nonlinear trend with respect to $k\phi$ as a result of multiple scattering.

In chapter 4 we investigated the effect of change in the micro-structure of heterogeneous media on backscatter statistics using Shannon entropy. PDMS phantoms with different concentrations of BaTiO3 scatterers were evaluated. Increase in scatterer VF resulted

in an increase in entropy. In a FDTD study on cortical bone structures, a positive correlation between entropy and micro-structural parameters Ct.Po., Ct.Po.Dm. and Ct.Po.Dn. was observed. To model edema in lungs, we used porous phantoms with different air VFs since edema is associated with increased levels of fluid in lungs. Increase in air VF resulted in an increase in entropy, suggesting that it could be potentially used for quantitative assessment of edematous lungs.

REFERENCES

1. Bartl, R. & Frisch, B. Biology of Bone. in *Osteoporosis* 7–28 (Springer Berlin Heidelberg, 2009). doi:10.1007/978-3-540-79527-8_2

2. Karsenty, G. & Olson, E. N. Bone and Muscle Endocrine Functions: Unexpected Paradigms of Inter-organ Communication. *Cell* **164**, 1248–1256 (2016).

3. Langdahl, B., Ferrari, S. & Dempster, D. W. Bone modeling and remodeling: potential as therapeutic targets for the treatment of osteoporosis. *Therapeutic Advances in Musculoskeletal Disease* **8**, 225–235 (2016).

4. Akkus, O. Bone Morphology and Organization. *Basic Appl. Bone Biol.* 3–25 (2014). doi:10.1016/B978-0-12-416015-6.00001-0

5. Weinstein, S. L. & Buckwalter, J. A. *Turek's orthopaedics : principles and their application*. (Lippincott Williams & Wilkins, 2005).

6. Buckwalter, J. A., Glimcher, M. J., Cooper, R. R. & Recker, R. Bone biology. I: Structure, blood supply, cells, matrix, and mineralization. *Instr. Course Lect.* **45**, 371–86 (1996).

7. Bell, K. L. *et al.* A novel mechanism for induction of increased cortical porosity in cases of intracapsular hip fracture. *Bone* **27**, 297–304 (2000).

8. Buckwalter, J. A. & Cooper, R. R. Bone structure and function. *Instr. Course Lect.* **36**, 27–48 (1987).

9. Kelly, P. J. Anatomy, physiology, and pathology of the blood supply of bones. *J. Bone*

Joint Surg. Am. **50**, 766–83 (1968).

10. Brickley, M. & Ives, R. *The bioarchaeology of metabolic bone disease.* (Academic Press, 2008).

11. Mcnamara, L. M., Van Der Linden, J. C., Weinans, H. & Prendergast, P. J. Stress-concentrating effect of resorption lacunae in trabecular bone $. *J. Biomech.* **39**, 734–741 (2006).

12. Perez-Viloria, M., Villa-Camacho, J. C., Vaziri, A. & Nazarian, A. Biomechanics and Mechanobiology of Trabecular Bone: A Review. (2015). doi:10.1115/1.4029176

13. Fritsch, A. & Hellmich, C. 'Universal' microstructural patterns in cortical and trabecular, extracellular and extravascular bone materials: Micromechanics-based prediction of anisotropic elasticity. *J. Theor. Biol.* **244**, 597–620 (2007).

14. Pietschmann, P. *Principles of osteoimmunology : molecular mechanisms and clinical applications*. (Springer-Verlag/Wien, 2012).

15. Howard, G. A. & Schiller, P. C. Biology of Bone. (2016). doi:10.1007/978-3-319-25976-5_1

16. Wilhelm, M. *et al.* Effect of resistance exercises on function in older adults with osteoporosis or osteopenia: A systematic review. *Physiotherapy Canada* **64**, 386–394 (2012).

17. Osteoporosis: Diagnosis, Prevention, Therapy - Reiner Bartl, Bertha Frisch - Google Books. Available at: https://books.google.com/books?hl=en&lr=&id=DQiX-GJlZUsC&oi=fnd&pg=PA1&dq=biology+of+bone+bartl&ots=gHyp09_x-

p&sig=4tdtUhYjJTL6aLD6sJqIPT7IRJo#v=onepage&q=biology of bone bartl&f=false. (Accessed: 2nd January 2019)

18. Avioli., edited by L. V. *The Osteoporotic syndrome : detection, prevention, and treatment*. (San Diego, Calif. : Academic, c2000., 2000).

19. Tenenhouse, A. *et al.* Estimation of the prevalence of low bone density in Canadian women and men using a population-specific DXA reference standard: the Canadian Multicentre Osteoporosis Study (CaMos). *Osteoporos. Int.* **11**, 897–904 (2000).

20. Riggs, B. L. *et al.* Changes in bone mineral density of the proximal femur and spine with aging. Differences between the postmenopausal and senile osteoporosis syndromes. *J. Clin. Invest.* **70**, 716–23 (1982).

21. Melton, L. J., Crowson, C. S. & O'Fallon, W. M. Fracture incidence in Olmsted County, Minnesota: comparison of urban with rural rates and changes in urban rates over time. *Osteoporos. Int.* **9**, 29–37 (1999).

22. Cummings, S. R. & Melton, L. J. Osteoporosis I: Epidemiology and outcomes of osteoporotic fractures. *Lancet* **359**, 1761–1767 (2002).

23. Melton, L. J. Adverse Outcomes of Osteoporotic Fractures in the General Population. *J. Bone Miner. Res.* **18**, 1139–1141 (2003).

24. Magaziner, J. *et al.* Recovery from hip fracture in eight areas of function. *J. Gerontol. A. Biol. Sci. Med. Sci.* **55**, M498-507 (2000).

25. Khan, A. A. *et al.* Management of osteoporosis in men: an update and case example. *CMAJ* **176**, 345–8 (2007).

26. Papaioannou, A. *et al.* Diagnosis and management of vertebral fractures in elderly adults. *Am. J. Med.* **113**, 220–8 (2002).

27. Barrett, J. A., Baron, J. A., Karagas, M. R. & Beach, M. L. Fracture risk in the U.S. Medicare population. *J. Clin. Epidemiol.* **52**, 243–9 (1999).

28. Campbell, A. J. *et al.* Circumstances and consequences of falls experienced by a community population 70 years and over during a prospective study. *Age Ageing* **19**, 136–41 (1990).

29. Mimouni, F. B. & Littner, Y. Bone mass evaluation in children - comparison between methods. *Pediatr. Endocrinol. Rev.* **1**, 320–30 (2004).

30. Gilsanz, V. Bone density in children: a review of the available techniques and indications. *Eur. J. Radiol.* **26**, 177–82 (1998).

31. Burr, D. B. & Allen, M. R. (Professor of anatomy and cell biology). *Basic and applied bone biology*.

32. Larose, E. Mesoscopics of ultrasound and seismic waves: application to passive imaging. (2006).

33. Wear, K. A. Anisotropy of ultrasonic backscatter and attenuation from human calcaneus: Implications for relative roles of absorption and scattering in determining attenuation. *Cit. J. Acoust. Soc. Am.* **107**, 3474 (2000).

34. Wear, K. A. The effects of frequency-dependent attenuation and dispersion on sound speed measurements: applications in human trabecular bone. *IEEE Trans. Ultrason. Ferroelectr. Freq. Control* **47**, 265–273 (2000).

35. Wear, K. A. Ultrasonic scattering from cancellous bone: A review. *IEEE Trans. Ultrason. Ferroelectr. Freq. Control* **55**, 1432–1441 (2008).

36. Tabor, E., Pluskiewicz, W. & Tabor, K. Clinical Conformity Between Heel Ultrasound and Densitometry in Postmenopausal Women: A Systematic Review. *J. Ultrasound Med.* **37**, 363–369 (2018).

37. Langton, C. M., Palmer, S. B. & Porter, R. W. The Measurement of Broadband Ultrasonic Attenuation in Cancellous Bone. *Eng. Med.* **13**, 89–91 (1984).

38. Culjat, M. O., Goldenberg, D., Tewari, P. & Singh, R. S. A review of tissue substitutes for ultrasound imaging. *Ultrasound Med. Biol.* **36**, 861–873 (2010).

39. Lluveras Núñez, D., Molero-Armenta, M., Izquierdo, M., Hernández, M. & Anaya Velayos, J. Ultrasound Transmission Tomography for Detecting and Measuring Cylindrical Objects Embedded in Concrete. *Sensors* **17**, 1085 (2017).

40. Yu, T. *et al.* Simulations of ultrasonic wave propagation in concrete based on a two-dimensional numerical model validated analytically and experimentally. *Ultrasonics* **92**, 21–34 (2019).

41. Madsen, E. L. *et al.* Oil-in-gelatin dispersions for use as ultrasonically tissue-mimicking materials. *Ultrasound Med. Biol.* **8**, 1150–1159 (1990).

42. Su, Q., Tan, C. & Dong, F. Mechanism modeling for phase fraction measurement with ultrasound attenuation in oil-water two-phase flow. *Meas. Sci. Technol.* **28**, (2017).

43. Wear, K. A., Stuber, A. P. & Reynolds, J. C. Relationships of ultrasonic backscatter with ultrasonic attenuation, sound speed and bone mineral density in human calcaneus.

Ultrasound Med. Biol. **26**, 1311–1316 (2000).

44. Sasso, M., Haïat, G., Yamato, Y., Naili, S. & Matsukawa, M. Frequency Dependence of Ultrasonic Attenuation in Bovine Cortical Bone: An In Vitro Study. *Ultrasound Med. Biol.* **33**, 1933–1942 (2007).

45. Yousefian, O., White, R. D., Karbalaeisadegh, Y., Banks, H. T. & Muller, M. Human and Machine Hearing: Extracting Meaning from Sound The Journal of the. *J. Acoust. Soc. Am.* **144**, 525 (2018).

46. Abendschein, W. & Hyatt, G. W. Ultrasonics and selected physical properties of bone. *Clin. Orthop. Relat. Res.* **69**, 294–301

47. Ashman, R. B., Corin, J. D. & Turner, C. H. Elastic properties of cancellous bone: Measurement by an ultrasonic technique. *J. Biomech.* **20**, 979–986 (1987).

48. Ashman, R. B. & Jae Young Rho. Elastic modulus of trabecular bone material. *J. Biomech.* **21**, 177–181 (1988).

49. Guglielmi, G., Adams, J. & Link, T. M. Quantitative ultrasound in the assessment of skeletal status. *Eur. Radiol.* **19**, 1837–1848 (2009).

50. Njeh, C. F., Boivin, C. M. & Langton, C. M. The role of ultrasound in the assessment of osteoporosis: A review. *Osteoporos. Int.* **7**, 7–22 (1997).

51. Foldes, A. J., Rimon, A., Keinan, D. D. & Popovtzer, M. M. Quantitative ultrasound of the tibia: a novel approach for assessment of bone status. *Bone* **17**, 363–7 (1995).

52. Kang, C. & Speller, R. Comparison of ultrasound and dual energy X-ray absorptiometry measurements in the calcaneus. *Br. J. Radiol.* **71**, 861–867 (1998).

53. Prins, S. H., Jørgensen, H. L., Jørgensen, L. V & Hassager, C. The role of quantitative ultrasound in the assessment of bone: a review. *Clin. Physiol.* **18**, 3–17 (1998).

54. Lee, S. C., Coan, B. S. & Bouxsein, M. L. Tibial ultrasound velocity measured in situ predicts the material properties of tibial cortical bone. *Bone* **21**, 119–125 (1997).

55. Talmant, M. *et al.* In vivo Performance Evaluation of Bi-Directional Ultrasonic Axial Transmission for Cortical Bone Assessment. *Ultrasound Med. Biol.* **35**, 912–919 (2009).

56. Wear, K. A. Measurements of phase velocity and group velocity in human calcaneus. *Ultrasound Med. Biol.* **26**, 641–6 (2000).

57. Nebot, E. *et al.* Paget's Disease of Long Bones: Microstructural Analyses of Historical Bone Samples. *Calcif. Tissue Int.* **105**, 15–25 (2019).

58. Pande, K. ., Bernard, J., McCloskey, E. ., de Takats, D. & Kanis, J. . Ultrasound velocity and dual-energy X-ray absorptiometry in normal and pagetic bone. *Bone* **26**, 525–528 (2000).

59. Planès, T. & Larose, E. A review of ultrasonic Coda Wave Interferometry in concrete. *Cem. Concr. Res.* **53**, 248–255 (2013).

60. Aki, K. & Wu, R.-S. *Scattering and attenuations of seismic waves*. (Springer Basel AG, 1988).

61. Sato, H. & Fehler, M. C. *Seismic wave propagation and scattering in the heterogeneous earth*. (Springer-Verlag, 2009).

62. Xu, R. X. *et al.* Localization and Functional Parameter Reconstruction of Suspicious

Breast Lesions by Near Infrared/Ultrasound Dual Modal Imaging. in *2005 IEEE Engineering in Medicine and Biology 27th Annual Conference* 4473–4476 (IEEE, 2005). doi:10.1109/IEMBS.2005.1615460

63. Gubernatis, J. E., Domany, E., Krumhansl, J. A. & Huberman, M. The Born approximation in the theory of the scattering of elastic waves by flaws. *J. Appl. Phys.* **48**, 2812–2819 (1977).

64. Chew, W. C. & Wang, Y. M. Reconstruction of two-dimensional permittivity distribution using the distorted Born iterative method. *IEEE Trans. Med. Imaging* **9**, 218–225 (1990).

65. Poupinet, G., Ellsworth, W. L. & Frechet, J. Monitoring velocity variations in the crust using earthquake doublets: An application to the Calaveras Fault, California. *J. Geophys. Res. Solid Earth* **89**, 5719–5731 (1984).

66. Pine, D. J., Weitz, D. A., Chaikin, P. M. & Herbolzheimer ', E. *PHYSICAL REVIEW LETTERS Diffusing-Wave Spectroscopy*. **60**, (1988).

67. Cowan, M. L., Jones, I. P., Page, J. H. & Weitz, D. A. Diffusing acoustic wave spectroscopy. doi:10.1103/PhysRevE.65.066605

68. Leroy, V. & Derode, A. Temperature-dependent diffusing acoustic wave spectroscopy with resonant scatterers. doi:10.1103/PhysRevE.77.036602

69. Grêt, A., Snieder, R., Aster, R. C. & Kyle, P. R. Monitoring rapid temporal change in a volcano with coda wave interferometry. *Geophys. Res. Lett.* **32**, L06304 (2005).

70. Brenguier, F. *et al.* Towards forecasting volcanic eruptions using seismic noise. *Nat.*

Geosci. **1**, 126–130 (2008).

71. Brenguier, F. *et al.* Postseismic relaxation along the San Andreas fault at Parkfield from continuous seismological observations. *Science* **321**, 1478–81 (2008).

72. Ham, S., Song, H., Oelze, M. L. & Popovics, J. S. A contactless ultrasonic surface wave approach to characterize distributed cracking damage in concrete. *Ultrasonics* **75**, 46–57 (2017).

73. Ramamoorthy, S. K., Kane, Y., Turner, J. A. & Turner, J. A. Ultrasound diffusion for crack depth determination in concrete. (2004). doi:10.1121/1.1642625

74. Anugonda, P., Wiehn, J. S. & Turner, J. A. Diffusion of ultrasound in concrete. *Ultrasonics* **39**, 429–435 (2001).

75. Larose, E. *et al.* Observation of multiple scattering of kHz vibrations in a concrete structure and application to monitoring weak changes. *Phys. Rev. E* **73**, 016609 (2006).

76. Schurr, D. P., Kim, J.-Y., Sabra, K. G. & Jacobs, L. J. Damage detection in concrete using coda wave interferometry. *NDT E Int.* **44**, 728–735 (2011).

77. Karaiskos, G., Deraemaeker, A., Aggelis, D. G. & Hemelrijck, D. Van. Monitoring of concrete structures using the ultrasonic pulse velocity method. *Smart Mater. Struct.* **24**, 113001 (2015).

78. Xue, Q., Larose, E. & Moreau, L. Locating structural changes in a multiple scattering domain with an irregular shape. *J. Acoust. Soc. Am.* **146**, 595–602 (2019).

79. Ishimaru, A. *Wave propagation and scattering in random media*. (IEEE Press, 1997).

80. Barabanenkov, Y. N. Multiple scattering of waves by ensembles of particles and the theory of radiation transpor. *Sov. Phys. - Uspekhi* **18**, 673–689 (1975).

81. Rozenberg, G. V. PHYSICAL BASIS OF THE SPECTROSCOPY OF LIGHT-SCATTERING SUBSTANCES. *Sov. Phys. Uspekhi* **10**, 188–213 (1967).

82. Peierls, R. E. *Quantum Theory of Solids*. (Clarendon Press, Oxford, 1955).

83. Davison, B. *Neutron Transport Theory*. (Clarendon Press, Oxford, 1958).

84. American Institute of Physics., D. Y. & Sharvin, Y. V. *JETP letters. JETP Letters, Volume 34, Issue 5, September 5, 1981, pp.272-275* **34**, (American Institute of Physics, 1981).

85. Umbach, C. P., Van Haesendonck, C., Laibowitz, R. B., Washburn, S. & Webb, R. A. Direct observation of ensemble averaging of the Aharonov-Bohm effect in normal-metal loops. *Phys. Rev. Lett.* **56**, 386–389 (1986).

86. Albada, M. P. Van & Lagendijk, A. Observation of Weak Localization of Light in a Random Medium. *Phys. Rev. Lett.* **55**, 2692–2695 (1985).

87. Wolf, P. E. & Maret, G. Weak localization and coherent backscattering of photons in disordered media. *Phys. Rev. Lett.* **55**, 2696–2699 (1985).

88. Tourin, A., Derode, A., Roux, P., van Tiggelen, B. A. & Fink, M. Time-Dependent Coherent Backscattering of Acoustic Waves. *Phys. Rev. Lett.* **79**, 3637–3639 (1997).

89. Tourin, A., Derode, A., Peyre, A. & Fink, M. Transport parameters for an ultrasonic pulsed wave propagating in a multiple scattering medium. *J. Acoust. Soc. Am.* **108**, 503–512 (2000).

90. Page, J. . *et al.* Diffusive transport of acoustic waves in strongly scattering media. *Phys. B Condens. Matter* **263**–**264**, 37–39 (1999).

91. Aubry, A. & Derode, A. Ultrasonic imaging of highly scattering media from local measurements of the diffusion constant: Separation of coherent and incoherent intensities. *Phys. Rev. E - Stat. Nonlinear, Soft Matter Phys.* **75**, 1–9 (2007).

92. Aubry, A., Derode, A. & Padilla, F. Local measurements of the diffusion constant in multiple scattering media: Application to human trabecular bone imaging. *Appl. Phys. Lett.* **92**, 124101 (2008).

93. Radiative transfer. By S. Chandrasekhar. London (Oxford University Press) 1950. 8vo. Pp. 393, 35 figures. 35s. *Q. J. R. Meteorol. Soc.* **76**, 498–498 (1950).

94. Rytov, S. M., Kravtsov, Y. A. & Tatarskii, V. I. *Principles of Statistical Radiophysics 1*. (Springer-Verlag, 1987).

95. Paasschens, J. C. J. Solution of the time-dependent Boltzmann equation. *Phys. Rev. E - Stat. Physics, Plasmas, Fluids, Relat. Interdiscip. Top.* **56**, 1135–1141 (1997).

96. Mamou, V. Caractérisation ultrasonore d'échantillons hétérogènes multiplement diffuseurs. (Paris Diderot University, 2005).

97. Eneh, C. T. M., Afara, I. O., Malo, M. K. H., Jurvelin, J. S. & Töyräs, J. Porosity predicted from ultrasound backscatter using multivariate analysis can improve accuracy of cortical bone thickness assessment. *J. Acoust. Soc. Am.* **141**, 575 (2017).

98. Bousson, V. *et al.* Distribution of intracortical porosity in human midfemoral cortex by age and gender. *J. Bone Miner. Res.* **16**, 1308–1317 (2001).

99. Cooper, D. M. L., Kawalilak, C. E., Harrison, K., Johnston, B. D. & Johnston, J. D. Cortical Bone Porosity: What Is It, Why Is It Important, and How Can We Detect It? *Curr. Osteoporos. Rep.* **14**, 187–198 (2016).

100. Zebaze, R. M. *et al.* Intracortical remodelling and porosity in the distal radius and post-mortem femurs of women: a cross-sectional study. *Lancet* **375**, 1729–1736 (2010).

101. Schneider, P. *et al.* Ultrastructural properties in cortical bone vary greatly in two inbred strains of mice as assessed by synchrotron light based micro- and nano-CT. *J. Bone Miner. Res.* **22**, 1557–1570 (2007).

102. Mgeough, A. & Barker, B. Age-Related. **75**, (1993).

103. Palacio-Mancheno, P. E., Larriera, A. I., Doty, S. B., Cardoso, L. & Fritton, S. P. 3D assessment of cortical bone porosity and tissue mineral density using high-resolution μcT: Effects of resolution and threshold method. *J. Bone Miner. Res.* **29**, 142–150 (2014).

104. Rajapakse, C. S. *et al.* Volumetric Cortical Bone Porosity Assessment with MR Imaging: Validation and Clinical Feasibility. *Radiology* **276**, 526–35 (2015).

105. Spadaro, J. A. *et al.* Cortical and trabecular bone contribute strength to the osteopenic distal radius. *J. Orthop. Res.* **12**, 211–218 (1994).

106. Augat, P., Reeb, H. & Claes, L. E. Prediction of fracture load at different skeletal sites by geometric properties of the cortical shell. *J. Bone Miner. Res.* **11**, 1356–1363 (2009).

107. Burghardt, A. J., Kazakia, G. J., Ramachandran, S., Link, T. M. & Majumdar, S. Age- and gender-related differences in the geometric properties and biomechanical significance of intracortical porosity in the distal radius and tibia. *J. Bone Miner. Res.* **25**, 983–993 (2010).

108. David Rockoef, S., Sweet, E. & Bletjstein, J. The Relative Contribution of Trabecular and Cortical Bone to the Strength of Human Lumbar Vertebrae*. *Calc. Tiss. Res* **3**, 163–175 (1969).

109. Holzer, G., Von Skrbensky, G., Holzer, L. A. & Pichl, W. Hip fractures and the contribution of cortical versus trabecular bone to femoral neck strength. *J. Bone Miner. Res.* **24**, 468–474 (2009).

110. Ross, P. D., Davis, J. W., Vogel, J. M. & Wasnich, R. D. A critical review of bone mass and the risk of fractures in osteoporosis. *Calcif. Tissue Int.* **46**, 149–161 (1990).

111. Marshall, D., Johnell, O. & Wedel, H. Meta-analysis of how well measures of bone mineral density predict occurrence of osteoporotic fractures. *Bmj* **312**, 1254–1259 (1996).

112. Van Der Mark, M. B., Van Albada, M. P. & Lagendijk, A. Light scattering in strongly scattering media: Multiple scattering and weak localization. *Phys. Rev. B* **37**, 3575–3592 (1988).

113. Tourin, A., Derode, A., Peyre, A. & Fink, M. in a Multiple Scattering Medium. **108**, 503–512 (2000).

114. Sato, H. & Fehler, M. C. *Seismic Wave Propagation and Scattering in the*

Heterogeneous Earth. (2012). doi:10.1007/978-3-642-23029-5

115. Tourin, A., Derode, A., Roux, P., van Tiggelen, B. A. & Fink, M. Time-Dependent Coherent Backscattering of Acoustic Waves. *Phys. Rev. Lett.* **79**, 3637–3639 (1997).

116. Wiersma, D. S., Bartolini, P., Lagendijk, A. & Righini, R. Localizationof light ina disorderedmedium. *Nature* **390**, 671–673 (1997).

117. Derode, A., Mamou, V., Padilla, F., Jenson, F. & Laugier, P. Dynamic coherent backscattering in a heterogeneous absorbing medium: Application to human trabecular bone characterization. *Appl. Phys. Lett.* **87**, 1–3 (2005).

118. Iori, G. *et al.* BMD-based assessment of local porosity in human femoral cortical bone. *Bone* **114**, 50–61 (2018).

119. Malo, M. K. H. *et al.* Longitudinal elastic properties and porosity of cortical bone tissue vary with age in human proximal femur. *Bone* **53**, 451–458 (2013).

120. Raum, K. Microelastic imaging of bone. *IEEE Trans. Ultrason. Ferroelectr. Freq. Control* **55**, 1417–1431 (2008).

121. Lakshmanan, S., Bodi, A. & Raum, K. Assessment of anisotropic tissue elasticity of cortical bone from high-resolution, angular acoustic measurements. *IEEE Trans. Ultrason. Ferroelectr. Freq. Control* **54**, 1560–1570 (2007).

122. Hube, R., Mayr, H., Hein, W. & Raum, K. • Original Contribution PREDICTION OF BIOMECHANICAL STABILITY AFTER CALLUS DISTRACTION BY HIGH RESOLUTION SCANNING ACOUSTIC MICROSCOPY. (2006). doi:10.1016/j.ultrasmedbio.2006.06.010

123. Raum, K. *et al.* Site-matched assessment of structural and tissue properties of cortical bone using scanning acoustic microscopy and synchrotron radiation μcT. *Phys. Med. Biol.* **51**, 733–746 (2006).

124. Bakalova, L. P. *et al.* Intracortical Bone Mechanics Are Related to Pore Morphology and Remodeling in Human Bone. *J. Bone Miner. Res.* **33**, 2177–2185 (2018).

125. Bousson, V. *et al.* Distribution of intracortical porosity in human midfemoral cortex by age and gender. *J. Bone Miner. Res.* **16**, 1308–1317 (2001).

126. Cowin, S. & Telega, J. Bone Mechanics Handbook, 2nd Edition. -. *Appl. Mech. Rev.* **56**, B61 (2003).

127. Thomas, C. D. L., Feik, S. A. & Clement, J. G. Increase in pore area, and not pore density, is the main determinant in the development of porosity in human cortical bone. *J. Anat.* **209**, 219–230 (2006).

128. Evans, F. & Bang, S. Differences and relationships between the physical properties and the microscopic structure of human femoral, tibial and fibular cortical bone. *Am. J. Anat.* **120**, 79–88 (1967).

129. Boutroy, S., Bouxsein, M. L., Munoz, F. & Delmas, P. D. In Vivo Assessment of Trabecular Bone Microarchitecture by High-Resolution Peripheral Quantitative Computed Tomography. (2005). doi:10.1210/jc.2005-1258

130. Burghardt, A. J., Buie, H. R., Laib, A., Majumdar, S. & Boyd, S. K. Reproducibility of direct quantitative measures of cortical bone microarchitecture of the distal radius and tibia by HR-pQCT. *Bone* **47**, 519–528 (2010).

131. Bossy, E., Talmant, M. & Laugier, P. Three-dimensional simulations of ultrasonic axial transmission velocity measurement on cortical bone models. *J. Acoust. Soc. Am.* **115**, 2314–2324 (2004).

132. Wang, Z. & Norman, T. L. Microdamage of human cortical bone: Incidence and morphology in long bones. *Bone* **20**, 375–379 (1997).

133. Tatarinov, a. & Sarvazyan, a. Topography of acoustical properties of long bones: from biomechanical studies to bone health assessment. *IEEE Trans. Ultrason. Ferroelectr. Freq. Control* **55**, 1287–1297 (2008).

134. Bossy, E. *SimSonic Suite User's guide for SimSonic2D*. (2012).

135. Bell, K. L. *et al.* A novel mechanism for induction of increased cortical porosity in cases of intracapsular hip fracture. *Bone* **27**, 297–304 (2000).

136. Nalla, R. K. *et al.* Role of microstructure in the aging-related deterioration of the toughness of human cortical bone. (2005). doi:10.1016/j.msec.2005.08.021

137. Treece, G. M., Gee, A. H., Mayhew, P. M. & Poole, K. E. S. High resolution cortical bone thickness measurement from clinical CT data. *Med. Image Anal.* **14**, 276–90 (2010).

138. Cooper, D. M. L., Thomas, C. D. L., Clement, J. G. & Hallgrímsson, B. Three-dimensional microcomputed tomography imaging of basic multicellular unit-related resorption spaces in human cortical bone. *Anat. Rec. - Part A Discov. Mol. Cell. Evol. Biol.* **288**, 806–816 (2006).

139. Thomas, C. D. L., Feik, S. A. & Clement, J. G. Increase in pore area, and not pore

density, is the main determinant in the development of porosity in human cortical bone. *J. Anat.* **209**, 219–230 (2006).

140. Chakrabarti, S., Syme, H. M. & Elliott, J. Clinicopathological Variables Predicting Progression of Azotemia in Cats with Chronic Kidney Disease. *J. Vet. Intern. Med.* **26**, 275–281 (2012).

141. Chen, H., Zhou, X., Fujita, H., Onozuka, M. & Kubo, K.-Y. Age-Related Changes in Trabecular and Cortical Bone Microstructure. *Int. J. Endocrinol.* **2013**, (2013).

142. Yerramshetty, J. & Akkus, O. Changes in Cortical Bone Mineral and Microstructure with Aging and Osteoporosis. in *Stud Mechanobiol Tissue Eng Biomater* 105–131 (Springer, Berlin, Heidelberg, 2012). doi:10.1007/8415_2012_114

143. Burghardt, A. J., Kazakia, G. J., Ramachandran, S., Link, T. M. & Majumdar, S. Age- and gender-related differences in the geometric properties and biomechanical significance of intracortical porosity in the distal radius and tibia. *J. Bone Miner. Res.* **25**, 983–993 (2010).

144. Cooper, D. M. L., Kawalilak, C. E., Harrison, K., Johnston, B. D. & Johnston, J. D. Cortical Bone Porosity: What Is It, Why Is It Important, and How Can We Detect It? *Curr. Osteoporos. Rep.* **14**, 187–198 (2016).

145. Zebaze, R. M. D. *et al.* Intracortical remodelling and porosity in the distal radius and post-mortem femurs of women: a cross-sectional study. *Lancet* **375**, 1729–1736 (2010).

146. Iori, G. *et al.* Large cortical bone pores in the tibia are associated with proximal femur

strength. *PLoS One* **14**, e0215405 (2019).

147. Andreasen, C. M. *et al.* Understanding Age-Induced Cortical Porosity in Women: The Accumulation and Coalescence of Eroded Cavities Upon Existing Intracortical Canals Is the Main Contributor. *J. Bone Miner. Res.* **33**, 606–620 (2018).

148. Laugier, P. Quantitative ultrasound of bone: looking ahead. *Jt. Bone Spine* **73**, 125–128 (2006).

149. Muller, M. *et al.* Comparison of three ultrasonic axial transmission methods for bone assessment. *Ultrasound Med. Biol.* **31**, 633–42 (2005).

150. Seeman, E. & Delmas, P. D. *Mechanisms of Disease Bone Quality-The Material and Structural Basis of Bone Strength and Fragility*. (2006).

151. Bensamoun, S. *et al.* Spatial distribution of acoustic and elastic properties of human femoral cortical bone. *J. Biomech.* **37**, 503–510 (2004).

152. Schneider, J. *et al.* In Vivo Measurements of Cortical Thickness and Porosity at the Proximal Third of the Tibia Using Guided Waves: Comparison with Site-Matched Peripheral Quantitative Computed Tomography and Distal High-Resolution Peripheral Quantitative Computed Tomography. *Ultrasound Med. Biol.* **45**, 1234–1242 (2019).

153. Yousefian, O., White, R. D., Karbalaeisadegh, Y., Banks, H. T. & Muller, M. The effect of pore size and density on ultrasonic attenuation in porous structures with mono-disperse random pore distribution: A two-dimensional in-silico study. *J. Acoust. Soc. Am.* **144**, 709–719 (2018).

154. Punurai, W. Cement-based Materials' Characterization using Ultrasonic Attenuation.

PhD Thesis (2006).

155. Mézière, F., Muller, M., Bossy, E. & Derode, A. Measurements of ultrasound velocity and attenuation in numerical anisotropic porous media compared to Biot's and multiple scattering models. *Ultrasonics* **54**, 1146–1154 (2014).

156. Pinton, G. *et al.* Attenuation, scattering, and absorption of ultrasound in the skull bone. *Med. Phys.* **39**, 299–307 (2011).

157. Yousefian, O., Karbalaeisadegh, Y. & Muller, M. Modeling ultrasound attenuation in porous structures with mono-disperse random pore distributions using the independent scattering approximation: a 2D simulation study. *Phys. Med. Biol.* **64**, 155013 (2019).

158. Mohanty, K. *et al.* Artificial neural network to estimate micro-architectural properties of cortical bone using ultrasonic attenuation: A 2-D numerical study. *Comput. Biol. Med.* **114**, 103457 (2019).

159. Cai, X. *et al.* Quantification of stiffness measurement errors in resonant ultrasound spectroscopy of human cortical bone. *J. Acoust. Soc. Am.* **142**, 2755–2765 (2017).

160. Laugier, P. & Haïat, G. Introduction to the Physics of Ultrasound. in *Bone Quantitative Ultrasound* 29–45 (Springer Netherlands, 2011). doi:10.1007/978-94-007-0017-8_2

161. Papadakis, E. P. Ultrasonic Attenuation Caused by Scattering in Polycrystalline Metals. *J. Acoust. Soc. Am.* **37**, 711–717 (1965).

162. Granke, M. *et al.* Change in porosity is the major determinant of the variation of cortical bone elasticity at the millimeter scale in aged women. *Bone* **49**, 1020–1026

(2011).

163. Brunet, T. *et al.* Soft 3D acoustic metamaterial with negative index. *Nat. Mater.* **14**, 384–388 (2015).

164. Karbalaeisadegh, Y., Yousefian, O. & Muller, M. Influence of Micro-Structural Parameters on Apparent Absorption Coefficient in Porous Structures Mimicking Cortical Bone. in *2018 IEEE International Ultrasonics Symposium (IUS)* 1–4 (IEEE, 2018). doi:10.1109/ULTSYM.2018.8579610

165. Lees, S. & Klopholz, D. Z. Sonic velocity and attenuation in wet compact cow femur for the frequency range 5 to 100 MHz. *Ultrasound Med. Biol.* **18**, 303–8 (1992).

166. Karbalaeisadegh, Y., Yousefian, O., Iori, G., Raum, K. & Muller, M. Acoustic diffusion constant of cortical bone: Numerical simulation study of the effect of pore size and pore density on multiple scattering. *J. Acoust. Soc. Am.* **146**, 1015–1023 (2019).

167. NAKAGAMI, M. The m-Distribution—A General Formula of Intensity Distribution of Rapid Fading. *Stat. Methods Radio Wave Propag.* 3–36 (1960). doi:10.1016/B978-0-08-009306-2.50005-4

168. Mohana Shankar, P. A general statistical model for ultrasonic backscattering from tissues. *IEEE Trans. Ultrason. Ferroelectr. Freq. Control* **47**, 727–736 (2000).

169. Tsui, P.-H. *et al.* Use of Nakagami Statistics and Empirical Mode Decomposition for Ultrasound Tissue Characterization by a Nonfocused Transducer. *Ultrasound Med. Biol.* **35**, 2055–2068 (2009).

170. Ma, H.-Y. *et al.* Ultrasound window-modulated compounding Nakagami imaging: Resolution improvement and computational acceleration for liver characterization. *Ultrasonics* **70**, 18–28 (2016).

171. Tsui, P.-H. & Wan, Y.-L. Application of Ultrasound Nakagami Imaging for the Diagnosis of Fatty Liver. *J. Med. Ultrasound* **24**, 47–49 (2016).

172. Shankar, P. M. *et al.* Classification of ultrasonic B-mode images of breast masses using Nakagami distribution. *IEEE Trans. Ultrason. Ferroelectr. Freq. Control* **48**, 569–580 (2001).

173. Klimonda, Z., Karwat, P., Dobruch-Sobczak, K., Piotrzkowska-Wróblewska, H. & Litniewski, J. Breast-lesions characterization using Quantitative Ultrasound features of peritumoral tissue. *Sci. Rep.* **9**, 7963 (2019).

174. Shannon, C. E. *A Mathematical Theory of Communication*. *The Bell System Technical Journal* **27**,

175. Machta, J. Entropy, information, and computation. *Am. J. Phys.* **67**, 1074–1077 (1999).

176. Tsui, P.-H. Ultrasound Detection of Scatterer Concentration by Weighted Entropy. *Entropy* **17**, 6598–6616 (2015).

177. Tsui, P. H. *et al.* Small-window parametric imaging based on information entropy for ultrasound tissue characterization. *Sci. Rep.* **7**, 1–17 (2017).

178. Zhou, Z. *et al.* Hepatic Steatosis Assessment with Ultrasound Small-Window Entropy Imaging. *Ultrasound Med. Biol.* **44**, 1327–1340 (2018).

179. Lin, Y.-H., Liao, Y.-Y., Yeh, C.-K., Yang, K.-C. & Tsui, P.-H. Ultrasound Entropy Imaging of Nonalcoholic Fatty Liver Disease: Association with Metabolic Syndrome. *Entropy* **20**, 893 (2018).

180. Tsui, P.-H. & Wan, Y.-L. Effects of Fatty Infiltration of the Liver on the Shannon Entropy of Ultrasound Backscattered Signals. *Entropy* **18**, 341 (2016).

181. Zhou, Z. *et al.* Entropic imaging of cataract lens: an in vitro study. *PLoS One* **9**, e96195 (2014).

182. Hans, D. *et al.* Assessment of the 10-Year Probability of Osteoporotic Hip Fracture Combining Clinical Risk Factors and Heel Bone Ultrasound: The EPISEM Prospective Cohort of 12,958 Elderly Women. *J. Bone Miner. Res.* **23**, 1045–1051 (2008).

183. Rho, J.-Y., Kuhn-Spearing, L. & Zioupos, P. Mechanical properties and the hierarchical structure of bone. *Med. Eng. Phys.* **20**, 92–102 (1998).

184. Yost, C. S., Matthay, M. A. & Gropper, M. A. Etiology of acute pulmonary edema during liver transplantation: A series of cases with analysis of the edema fluid. *Chest* **119**, 219–223 (2001).

185. Cottrell, T. S. *et al.* Electron microscopic alterations at the alveolar level in pulmonary edema. *Circ. Res.* **21**, 783–797 (1967).

186. Desai, S. R. *et al.* Acute respiratory distress syndrome caused by pulmonary and extrapulmonary injury: A comparative CT study. *Radiology* **218**, 689–693 (2001).

187. Gattinoni, L., Caironi, P., Pelosi, P. & Goodman, L. R. What has computed

tomography taught us about the acute respiratory distress syndrome? *American Journal of Respiratory and Critical Care Medicine* **164**, 1701–1711 (2001).

188. Demi, L., Egan, T. & Muller, M. Lung Ultrasound Imaging, a Technical Review. *Appl. Sci.* **10**, 462 (2020).

189. Kotok, D. *et al.* The evolution of radiographic edema in ARDS and its association with clinical outcomes: A prospective cohort study in adult patients. *J. Crit. Care* **56**, 222–228 (2020).

190. Soldati, G., Smargiassi, A., Demi, L. & Inchingolo, R. Artifactual Lung Ultrasonography: It Is a Matter of Traps, Order, and Disorder. *Appl. Sci.* **10**, 1570 (2020).

191. Soldati, G. *et al.* Is There a Role for Lung Ultrasound During the COVID-19 Pandemic? *J. Ultrasound Med.* (2020). doi:10.1002/jum.15284

192. Demi, L., Demi, M., Prediletto, R. & Soldati, G. Real-time multi-frequency ultrasound imaging for quantitative lung ultrasound – first clinical results. *J. Acoust. Soc. Am.* **148**, 998–1006 (2020).

193. Lichtenstein, D. & Mezière, G. A lung ultrasound sign allowing bedside distinction between pulmonary edema and COPD: the comet-tail artifact. *Intensive Care Med.* **24**, 1331–1334 (1998).

194. Mohanty, K., Blackwell, J., Egan, T. & Muller, M. Characterization of the Lung Parenchyma Using Ultrasound Multiple Scattering. *Ultrasound Med. Biol.* **43**, 993–1003 (2017).

195. Daane, L. & Greenstein, M. A demountable interconnect system for a 50/spl times/50 ultrasonic imaging transducer array. *IEEE Trans. Ultrason. Ferroelectr. Freq. Control* **44**, 978–982 (1997).

196. Shankar, P. M. Statistics of Boundaries in Ultrasonic B-Scan Images. *Ultrasound Med. Biol.* **41**, 268–280 (2015).

197. Carmeliet, P. & Jain, R. K. Angiogenesis in cancer and other diseases. *Nature* **407**, 249–257 (2000).

198. Deshpande, N., Needles, A. & Willmann, J. K. Molecular ultrasound imaging: current status and future directions. *Clin. Radiol.* **65**, 567–581 (2010).

199. Ferrara, K., Pollard, R. & Borden, M. Ultrasound Microbubble Contrast Agents: Fundamentals and Application to Gene and Drug Delivery. *Annu. Rev. Biomed. Eng.* **9**, 415–447 (2007).

200. Kruse, D. E. & Ferrara, K. W. A new imaging strategy using wideband transient response of ultrasound contrast agents. *IEEE Trans. Ultrason. Ferroelectr. Freq. Control* **52**, 1320–9 (2005).

201. Gessner, R. C., Aylward, S. R. & Dayton, P. A. Mapping Microvasculature with Acoustic Angiography Yields Quantifiable Differences between Healthy and Tumor-bearing Tissue Volumes in a Rodent Model. *Radiology* **264**, 733–740 (2012).

202. Gessner, R. C., Frederick, C. B., Foster, F. S. & Dayton, P. A. Acoustic Angiography: A New Imaging Modality for Assessing Microvasculature Architecture. *Int. J. Biomed. Imaging* **2013**, 1–9 (2013).

203. Lindsey, B., Rojas, J., Martin, K., Shelton, S. & Dayton, P. Acoustic characterization of contrast-to-tissue ratio and axial resolution for dual-frequency contrast-specific acoustic angiography imaging. *IEEE Trans. Ultrason. Ferroelectr. Freq. Control* **61**, 1668–1687 (2014).

204. Shelton, S. E., Lindsey, B. D., Tsuruta, J. K., Foster, F. S. & Dayton, P. A. Molecular Acoustic Angiography: A New Technique for High-resolution Superharmonic Ultrasound Molecular Imaging. *Ultrasound Med. Biol.* **42**, 769–781 (2016).

205. Marsh, J. N. *et al.* Frequency and concentration dependence of the backscatter coefficient of the ultrasound contrast agent Albunex®. *J. Acoust. Soc. Am.* **104**, 1654–1666 (1998).

206. Sboros, V. *et al.* The dependence of ultrasound contrast agents backscatter on acoustic pressure: theory versus experiment. *Ultrasonics* **40**, 579–83 (2002).

207. Tang, M.-X. & Eckersley, R. J. Frequency and pressure dependent attenuation and scattering by microbubbles. *Ultrasound Med. Biol.* **33**, 164–168 (2007).

208. Du, H., Mohanty, K. & Muller, M. Microstructural characterization of trabecular bone using ultrasonic backscattering and diffusion parameters. *J. Acoust. Soc. Am.* **141**, EL445--EL451 (2017).

209. Mohanty, K. *et al.* Ultrasound multiple scattering with microbubbles can differentiate between tumor and healthy tissue *in vivo*. *Phys. Med. Biol.* **64**, 115022 (2019).

210. Sibo Li *et al.* A dual-frequency co-linear array for prostate acoustic angiography. in *2016 IEEE International Ultrasonics Symposium (IUS)* 1–4 (IEEE, 2016).

doi:10.1109/ULTSYM.2016.7728718

211. Zhao, S., Kruse, D. E., Ferrara, K. W. & Dayton, P. A. Acoustic response from adherent targeted contrast agents. *J. Acoust. Soc. Am.* **120**, EL63–EL69 (2006).